ULTRASONIC ASSISTED REFLOW SOLDERING OF LEAD FREE SOLDER JOINT

TAN AI TING

FACULTY OF ENGINEERING
UNIVERSITY OF MALAYA
KUALA LUMPUR

2017

ULTRASONIC ASSISTED REFLOW SOLDERING OF LEAD FREE SOLDER JOINT

TAN AI TING

THESIS SUBMITTED IN FULFILMENT OF THE REQUIREMENTS FOR THE DEGREE OF DOCTOR OF PHILOSOPHY

FACULTY OF ENGINEERING
UNIVERSITY OF MALAYA
KUALA LUMPUR

2017

UNIVERSITY OF MALAYA
ORIGINAL LITERARY WORK DECLARATION

Name of Candidate: TAN AI TING

Matric No: KHA 120157

Name of Degree: DOCTOR OF PHILOSOPHY

Title of Project Paper/Research Report/Dissertation/Thesis ("this Work"):

ULTRASONIC ASSISTED REFLOW SOLDERING OF LEAD FREE SOLDER JOINT

Field of Study: MANUFACTURING PROCESSES

I do solemnly and sincerely declare that:

(1) I am the sole author/writer of this Work;
(2) This Work is original;
(3) Any use of any work in which copyright exists was done by way of fair dealing and for permitted purposes and any excerpt or extract from, or reference to or reproduction of any copyright work has been disclosed expressly and sufficiently and the title of the Work and its authorship have been acknowledged in this Work;
(4) I do not have any actual knowledge nor do I ought reasonably to know that the making of this work constitutes an infringement of any copyright work;
(5) I hereby assign all and every rights in the copyright to this Work to the University of Malaya ("UM"), who henceforth shall be owner of the copyright in this Work and that any reproduction or use in any form or by any means whatsoever is prohibited without the written consent of UM having been first had and obtained;
(6) I am fully aware that if in the course of making this Work I have infringed any copyright whether intentionally or otherwise, I may be subject to legal action or any other action as may be determined by UM.

Candidate's Signature Date:

Subscribed and solemnly declared before,

Witness's Signature Date:

Name:

Designation:

ABSTRACT

The present thesis focused on the development of ultrasonic assisted reflow soldering technique to improve the reliability of lead free solder joint in the electronic packaging application by integrating ultrasonic vibration (USV) into the reflow stage of a reflow soldering process. In the preliminary phase, Cu/Sn-Ag-Cu/Cu lead free solder joints were successfully fabricated by using 20 kHz USV with 169 W (high-power-low-frequency USV) and 55 kHz USV with 10 W (low-power-high-frequency USV). The material characterization tests revealed that the solder matrix microstructure was refined and the formation of interfacial intermetallic compound (IMC) was reduced after treated with both types of USV. This is attributed to the USV induced nucleation of β-Sn and eutectic phases as well as the homogeneity effect on the mass and heat transfer in the fully liquefied SAC solder. Additionally, USV induced degassing mechanism has taken effect on the size reduction of macrovoids in the solder joint which enhanced the shear strength of the ultrasonic-treated solder joints in return. The study also expressed the variation of USV time and its influence on the microstructural and mechanical properties of the solder joints. Coarsening of solder matrix was observed at prolonged USV time when using low-power-high-frequency USV. This may be associated with the prolonged of acoustic streaming induced by USV in the molten SAC, which allowed the nucleated β-Sn, Cu_6Sn_5 and Ag_3Sn crystals to grow larger with time. However, the solder joints with coarsened solder matrix microstructure exhibited higher shear strength compared to those with refined microstructure. Therefore, in the subsequent study, the effect of ultrasonic power on the solder joint properties was investigated by using low-power-high-frequency USV. The results revealed that higher ultrasonic power would induce greater superheating effect and promoted the formation of eutectic phase in the solder joints. Furthermore, the shear stress-strain curve acknowledged that the strength enhancement on the solder joint with

coarsened solder matrix microstructure was contributed by the strain hardening mechanism of the coarser β-Sn phase. Overall, the present studies progressively presented the caliber of the proposed ultrasonic assisted reflow soldering technique in producing reliable lead free solder joint with homogeneous solder matrix microstructure, thinner IMC and improved shear strength. These evidences demonstrate the potential use of ultrasonic assisted reflow soldering as a beneficial approach for the fabrication of lead free solder joints.

ABSTRAK

Tesis ini memberi tumpuan kepada pembangunan ultrasonik terbantu reflow pematerian teknik untuk meningkatkan keandalan sendi pateri bebas plumbum dalam aplikasi pembungkusan elektronik dengan mengintegrasikan getaran ultrasonik (USV) ke dalam tahap reflow proses reflow pematerian. Pada fasa permulaan, sendi pateri Cu/Sn-Ag-Cu/Cu telah berjaya difabrikasi dengan menggunakan 20 kHz USV yang berkuasa 169 W (kuasa-tinggi-frekuensi-rendah USV) dan 55 kHz USV yang berkuasa 10 W (kuasa rendah-frekuensi tinggi USV). Ujian pencirian material menunjukkan bahawa mikrostruktur pateri matrik telah diperhalusi dan pembentukan sebatian intermetik interfacial (IMC) dikurangkan selepas dirawat dengan kedua-dua jenis USV tersebut. Ini adalah disebabkan oleh nukleasi teraruh β-Sn dan fasa eutektik serta kesan homogeniti terhadap pemindahan jisim dan haba dalam pateri SAC lebur. Selain itu, mekanisme degassing yang diinduksikan oleh USV telah mengurangkan saiz macrovoids dalam sendi pateri dan juga meningkatkan kekuatan ricih sendi pateri terawat ultrasonik. Kajian ini juga menyatakan variasi masa USV dan pengaruhnya terhadap sifat mikrostruktur dan mekanik sendi pateri. Pengasaran pateri matrik diperhatikan pada masa USV yang berpanjangan apabila menggunakan kuasa rendah-frekuensi tinggi USV. Ini mungkin berkaitan dengan aliran akustik berpanjangan yang diinduksikan oleh USV dalam pateri SAC lebur, yang membolehkan kristal β-Sn, Cu6Sn5 dan Ag3Sn nukleus berkembang dengan lebih besar dengan masa. Walau bagaimanapun, sendi pateri dengan mikrostruktur pateri matrik yang mengasarkan menunjukkan kekuatan ricih yang lebih tinggi berbanding dengan mikrostruktur yang halus. Oleh itu, dalam kajian seterusnya, kesan kuasa ultrasonik pada sifat-sifat pateri sendi telah disiasat dengan menggunakan kuasa rendah-frekuensi tinggi USV. Keputusan yang diperolehi menunjukkan bahawa kuasa ultrasonik yang lebih tinggi akan mendorong kesan pemanasan yang lebih besar

dan mempromosikan pembentukan fasa eutektik dalam sendi pateri. Selain itu, lengkungan tegasan tegangan ricih mengesahkan bahawa peningkatan kekuatan sendi pateri yang mempunyai mikrostruktur pateri matrik yang mengasarkan adalah disumbangkan oleh mekanisme pengerasan terikan fasa β-Sn kasar. Secara keseluruhannya, kajian-kajian ini membentangkan secara progresif tentang kaliber ultrasonik terbantu reflow pematerian teknik yang dicadangkan dalam menghasilkan sendi pateri bebas plumbum yang mempungai mikrostructur pateri matrik yang homogen, IMC yang lebih nipis dan kekuatan ricih yang lebih baik. Bukti-bukti ini memperlihatkan potensi penggunaan ultrasonik terbantu reflow pematerian teknik sebagai kaedah yang bermanfaat untuk pembuatan sendi pateri bebas plumbum.

.

ACKNOWLEDGEMENTS

This thesis owes its existence to the help, support and inspiration of several people. First and foremost, I would like to express my heartfelt gratitude to my supervisor, Dr. Farazila binti Yusof for her unfailing support, invaluable guidance, inspirational encouragement and scientific freedom of thought throughout these past four years of my PhD life. Her tremendous academic support on my research and overall intellectual development of me as a PhD student have been invaluable.

I am also deeply indebted to Dr. Tan Ai Wen for her insightful comments and encouragement, but also for the hard question which incented me to widen my research from various perspectives.

I am also grateful to Prof. Dr. Ahmed Aly Diaa Mohammed Sarhan for allowing me to use his facilities whenever I needed for my experimental work.

I would also like to thank all my group mates, Nashrah Hani Jamadon, Maisarah Lufti, Shamini Janasekaran and Nur Ayuni Jamal for their friendship and warm-hearted help throughout my graduate study. It was a wonderful experience to work with them.

Last but not the least, my deepest gratitude goes to my family where the most basic source of my life energy resides. Their unflagging love and unconditional support throughout my life and in all my pursuits have made me who I am now.

TABLE OF CONTENTS

LIST OF FIGURES

LIST OF TABLES

LIST OF SYMBOLS AND ABBREVIATIONS

USV	Ultrasonic vibration
IMC	Intermetallic compound
Sn-Pb	Tin-lead
SAC	Sn-Ag-Cu
PCB	Printed circuit board
t	Aging time
x_0	IMC thickness of the as-soldered joint
x_t	IMC thickness at aging time, t
D_{eff}	Effective diffusion coefficient of IMC during thermal aging
$t^{1/2}$	Square root of aging time
D_0	Temperature-independent diffusion coefficient
Q	Activation energy
R	Universal gas constant
T	Absolute temperature in Kelvin
CTE	Coefficient of thermal expansion
t_{eff}	Total accumulated dwell duration
x	Total thickness of Cu_6Sn_5 and Cu_3Sn IMC layers at time t_{eff}
A	Growth constant
n	Time exponent

CHAPTER 1: INTRODUCTION

1.1 Background of study

The increasing global demand for portable electronic devices with advanced features and functionality has driven the use of surface-mount devices that are produced by reflow soldering process. The process involves melting of tin-based solder to permanently attach the surface-mount electrical components to their contact pads on a printed circuit board (PCB).

In the past, tin-lead (Sn-Pb) solders are practically the main conventional solders used for the interconnection in the electronic assemblies, typically package-to-board assemblies, due to their availability, low cost, low melting temperature, excellent wettability on most of the substrate materials, and capability to prevent transformation of β-Sn to α-Sn at temperature below 13°C (Abtew & Selvaduray, 2000). However, the use of these Sn-Pb solders has been restricted by several legislations due to the inherent toxicity of lead. Furthermore, the continued trend of miniaturization and occurrence of α-particle-induced soft errors challenged the reliability of Sn-Pb solder joints, leading to the substitution of lead free solders for Sn-Pb solders (Tu & Zeng, 2001).

Among the proposed lead free solders, Sn-Ag-Cu (SAC) solders have the highest degree of acceptance in the electronics industry, mainly because of their comparable or even superior mechanical properties than that of the Sn-Pb solders. However, owing to their inherent high melting temperature (217-220°C) and Sn content, higher thermal stress and thicker interfacial IMCs could be induced in the SAC solder joints (Abtew & Selvaduray, 2000; Frear, 2006; Marques, Johnston, & Grant, 2014). Additionally, the SAC solder joints are most likely exposed to high operating temperature and current stress, caused by the increasing power density in the portable electronic devices. This promotes the degradation of SAC solder joints through thermal aging and electromigration (Gain,

Zhang, & Chan, 2015; Laurila et al., 2012; Moore & Shi, 2014). The situation is exacerbated by the formation of voids caused by the evaporation of soldering flux in the solder joints, which reduces the heat dissipation efficiency during the operation and subsequently deteriorates the reliability of SAC solder joints as well as the performance of the devices (Bušek et al., 2016).

1.2 Problem statement

To address the above reliability concerns, new and ever-improving lead free solders and soldering processes are seen as the key solutions. Most of the recent research is focused on the development of composite lead free solders to substitute the conventional lead free solders, for example, SAC solders. The composite lead free solders are prepared by adding foreign nano-sized reinforcement, such as metallic (A. T. Tan, Tan, & Yusof, 2015; Yakymovych, Mudry, Shtablavyi, & Ipser, 2016), ceramic (Chellvarajoo & Abdullah, 2016; Wen et al., 2017; Zhao, Wen, Li, Liu, & Wang, 2016) and carbon-based material (Jing et al., 2017; Y. Ma, Li, Zhou, Yang, & Wu, 2017) into the lead free solders. The aforementioned studies indicate that the addition of nano-sized reinforcement refines the solder matrix microstructure and reduces the interfacial IMCs through the particle adsorption mechanism. The composite lead free solder joints are also reported to possess better mechanical properties due to the particle dispersion strengthening mechanism. Although satisfactory performance has been obtained in many studies, numerous studies have shown that the performance of a composite lead free solder highly depends on the interaction between the added reinforcement with both the lead free solder and the substrate (Chen, Wu, Liu, Silberschmidt, & Chan, 2016; Z. L. Ma, Belyakov, & Gourlay, 2016; Mohd Salleh, McDonald, Gourlay, Yasuda, & Nogita, 2016). It can be affected by the type (Laurila, Vuorinen, & Paulasto-Kröckel, 2010), size (Zhao et al., 2016), and amount (Chellvarajoo & Abdullah, 2016; A. T. Tan et al., 2015) of the added

reinforcement, as well as the preparation method of the composite solder (Fathian, Maleki, & Niroumand, 2017; Jing et al., 2017). Since the reliability of each potential composite lead free solder is not fully assessed to date, the search for the most promising replacement for conventional lead free solders is still in progress.

As for the soldering process, several new soldering techniques that utilize different heat transfer mechanism are developed to minimize the thermal stress introduced by the use of SAC solders (related to its high melting temperature) and the non-homogeneous heat distribution caused by the soldering of components with different thermal mass on a printed circuit board (PCB). Among the available techniques, infrared and convection reflow, vapor phase reflow and laser reflow soldering produce the most satisfying results for the electronics packaging industry. These methods offer several distinct advantages but also limitations. Infrared and convection reflow soldering utilizes infrared heaters and heated air convection to transfer heat to the soldering assembly. This process offers high throughput, versatile temperature profiling and processing parameters, and easier zone separation. However, the uniformity of temperature across the entire board is mostly concerned since each component on the board has its own thermal capacity and overheating is highly possible (Schussler, Kozic, & Franke, 2009). Therefore, research on developing simulation models or tools that can predict the thermal distribution and monitor the transient behavior of the solder reflows during the process is gaining its popularity (S.-S. Deng, Hwang, & Lee, 2016; Srivalli, Abdullah, & Khor, 2015; Xu, Hook, & Mayer, 2017). On the other hand, vapor phase reflow soldering has been introduced as it offers uniform heating through vapor condensation mechanism. Nevertheless, due to the excellent heat transfer coefficient of the vapor medium, the soldering assembly may not be adequately preheated, resulting in the solder joint with excessive voiding or paste sputtering (Illés & Géczy, 2016). Furthermore, the condensate layer thickness was found to have an effect on the heat distribution of the soldering

assembly (Illés, Géczy, Skwarek, & Busek, 2016). Uneven condensate layer thickness across the assembly will result in spatial heat transfer difference that leads to uneven solder joint quality and soldering failures. On the contrary, laser reflow soldering utilizes a focused laser beam to provide localized heating on each soldering area. The formation of solder joint is very rapid due to the rapid heating and cooling mechanism (Ogochukwu, 2013; Reinl, 2013). Thereby, the soldering assembly is subjected to lower thermal stress and the solder joint has a finer microstructure and thinner interfacial IMCs (B. Liu, Tian, Liu, Wu, & Wang, 2016; Nishikawa & Iwata, 2015). The major limitation on the application of this technique lies within the individual thermal capacity, light reflectivity and light adsorption coefficient of each component in the soldering assembly. This makes the selection of laser condition for the whole assembly to be very difficult (Imai, Kibushi, Hatakeyama, Nakagawa, & Ishizuka, 2014; Jung et al., 2016). The capability of this technique to solder large area is rather limited and the equipment capital for this process is very costly, as it requires laser source, accurate and precise positioning and alignment systems, as well as safety equipment (Jung et al., 2016; Ogochukwu, 2013). Additionally, in the study of Nishikawa and Iwata (2015), large amounts of Kirkendall voids were found in the thermally aged laser-soldered joints that contained extremely fine interfacial IMC grains under as-soldered condition. The authors attributed this to the faster diffusion of Cu atoms from the substrate into the interface through the excessive grain boundaries contributed by the extremely fine IMC grains. To homogenize the heat distribution and produce the lead free solder joint with lesser voids and thinner interfacial IMCs in a more cost effective manner, ultrasonic assisted reflow soldering with the application of USV during the solidification stage of reflow soldering has been proposed by several researchers (Chinnam, Fauteux, Neuenschwander, & Janczak-Rusch, 2011; Ji, Wang, & Li, 2016; Kago et al., 2004). Solder joint improvement in terms of hardness and shear strength was reported in these studies ascribed to the refinement of solder matrix

microstructure and thinner interfacial IMCs formation under the influence of USV, where USV induced nucleation and temperature homogeneity in the solidifying molten solder. However, these studies do not report any effect related to the well-known degassing mechanism induced by USV in a liquid medium, which the viscosity of the solidifying molten solder may be the underlying reason.

1.3 Objectives and scope of research

Therefore, the key scope of the present study is to explore the possibility of applying USV during the reflow stage of reflow soldering process, where the molten SAC solder has a complete fluidity. A thorough evaluation of the effect of USV parameters on the microstructural and mechanical properties of the SAC lead free solder joint is systematically investigated. Overall, the studies presented new insight in the application of ultrasonic in the reflow soldering process that enhances the microstructure and mechanical properties of the solder joints and lead to an improvement on the solder joint reliability. The objectives of the work are as follows:

1) To develop a new ultrasonic assisted reflow soldering technique by applying USV on the soldering assembly during the reflow stage.
2) To produce SAC lead free solder joints with enhanced properties by using the proposed reflow soldering technique.
3) To identify the suitable type of USV to be used for the soldering application.
4) To determine the effect of USV time and power on the microstructure and mechanical properties of the SAC lead free solder joints.

1.3 Dissertation overview

This dissertation is written in the format of published papers. The organization of the dissertation is structured as follows:

Chapter 1 gives an overview of the research background concerning of ultrasonic assisted reflow soldering, and the aim and objectives of the research.

Chapter 2 is meant to serve as the literature review of this research. A brief introduction on reflow soldering is given, and the microstructural evolution and interfacial reaction in a lead free solder joint, typically SAC/Cu solder joint, during reflow soldering are reviewed in detail. The reliability issues of lead free solder joint are discussed, and the current state of soldering techniques to improve the solder joint reliability is reviewed. This chapter identifies the areas of interest and the uncertainties that are then studied in Chapter 4 to 6.

Chapter 3 presents the general methodology for all the experiments for achieving the adopted objectives. The chapter also includes the safety aspect to conduct the experiments.

In **Chapter 4**, an ultrasonic assisted reflow soldering system is established and the generated USV is of low-frequency (20 kHz) but high-power (169 W). The effect of USV time on the microstructure and mechanical properties of SAC/Cu solder joints is investigated. The research in this chapter has been published in *Journal of Materials Processing Technology, Volume 238, 2016, Pages 8-14*, written by Ai Ting Tan, Ai Wen Tan and Farazila Yusof. The dissertation author is the first author of the publication.

Chapter 5 modifies the established ultrasonic assisted reflow soldering system to generate low-power-high-frequency USV (55 kHz, 10 W) and the influence of USV time on the properties of SAC/Cu solder joints is evaluated. The research in this chapter has been published in *Ultrasonics Sonochemistry, Volume 34, 2017, Pages 616-625*, written

by Ai Ting Tan, Ai Wen Tan and Farazila Yusof. The dissertation author is the first author of the publication.

Chapter 6 explores the evolution of microstructure and mechanical properties of SAC/Cu solder joints under the influence of ultrasonic power. The type of USV and the USV time used in the study are selected based on the results obtained from Chapter 4 and 5. The research in this chapter has been published in *Journal of Alloys and Compounds, Volume 705, 2017, Pages 188-197*, written by Ai Ting Tan, Ai Wen Tan and Farazila Yusof. The dissertation author is the first author of the publication.

Chapter 7 summarizes the entire significant outcome of the thesis and its novelty and contribution in the soldering industry. The chapter also substantially provides the recommendation for the continuation of the current studies.

CHAPTER 2: LITERATURE REVIEW

2.1 Introduction of reflow soldering

The global trend of miniaturization and the demand for electronic devices with advanced features and functionality have driven the use of surface mounted components in the electronic packaging industry. The soldering of these surface mounted components on a PCB, commonly called reflow soldering, is accomplished by the application of solder (usually in the form of solder paste or solder ball) on one of the mating surfaces. The assembly is then heated to melt the solder and the joint is formed upon solidification (Abtew & Selvaduray, 2000).

2.2 Types of solder for reflow soldering

2.2.1 Tin-lead (Sn-Pb) solder

Before the interference of global legislation, Sn-Pb solder with eutectic composition of 63Sn-37Pb or near eutectic composition of 60Sn-40Pb is commercially used in the package-to-board assemblies. As an alloying element, Pb provides many technical advantages to the Sn-Pb solder as follows (Abtew & Selvaduray, 2000; Y. Zhang, 2010):

1) Sn-Pb solder has a low melting temperature of 183°C, allowing the soldering conditions that are compatible with most of the substrate materials.
2) The cost of Sn-Pb solder is lower than most of the Sn-based solders since Pb is a low cost metal and readily available.
3) Pb improves the wettability of Sn-Pb solder by reducing the surface tension of pure tin.
4) Pb inhibits the transformation of ductile beta tin (β-Sn) to brittle alpha tin (α-Sn) at temperature below 13°C, which the volume can be increased by 26%.

However, due to inherent toxicity of Pb, the use of Pb in most electrical and electronic components has been banned or restricted by global legislations such as Waste Electrical and Electronic Equipment (WEEE) and Restriction of Hazardous Substances (RoHS) directives. Additionally, Sn-Pb solder might cause "soft error" failure in the integrated circuits at wafer level packages. Pb-containing solder may contain a small amount of radioactive ^{210}Pb isotopes that will decay to non-radioactive ^{206}Pb and emit α-particles. When these particles pass through a silicon (Si) device, they move around and produce charge along their path, leaving a trail of electrons and holes. When sufficient amounts of electrons were knocked out from the integrated circuit and accumulated in the capacitor (memory unit), the capacitor will be switched from 0 to 1 or from 1 to 0 (this is known as "soft error") (N. C. Lee, 2000; Tu & Zeng, 2001). Therefore, the transition to lead free solders is of paramount importance in the worldwide electronic industry.

2.2.2 Lead free solder

To serve as an alternative for Sn-Pb solder, the properties of the lead free solder must be comparable to or superior than the Sn-Pb solder in terms of manufacturability, reliability and environmental suitability. In overall, the lead free solder is expected to have the following criteria (Abtew & Selvaduray, 2000; Handwerker, Kattner, & Moon, 2007):

1) The physical properties (such as melting temperature, wettability, reworkability, cost, etc) should be as close to Sn-Pb solder as possible.
2) Binary or ternary composition is preferred and should be eutectic or close to eutectic.
3) The reliability and performance in terms of thermal expansion coefficient, mechanical strength, fatigue and creep behavior are equivalent to or better than Sn-Pb solder.
4) Avoid using patented solder due to the consideration of cost and availability.

Based on the works of N. C. Lee (2000), Puttlitz and Stalter (2004), and Handwerker et al. (2007), a worldwide consensus has developed that the Sn-Ag-Cu (SAC)

ternary solder is the most promising alternative for Sn-Pb solder in general purpose use. The recommended compositional range for SAC solder is 3 – 4 wt% Ag, 0.5 – 0.9 wt% Cu, with the remaining balance of Sn. It possesses the melting temperature of 217 - 220°C, which is relatively lower than the majority of the other lead free solders. It is reported that the SAC solder has good wettability, creep and thermal fatigue characteristics, and able to form reliable solder joint with comparable or even superior quality to Sn-Pb solder joint.

2.3 Reflow soldering profile

During the reflow soldering process, a soldering assembly is heated according to a temperature profile, which is known as reflow soldering profile. This profile enables the solder to react with the substrate material in a proper manner during soldering and forms a strong metallurgical bonding upon solidification.

A reflow soldering profile can be generally divided into preheat, reflow and cooling stages, as shown in Figure 2.1. Based on the reflow profile recommended by IPC/JEDEC joint industry standard (J-STD-020D-01A), the lead free soldering assembly is first preheated to a temperature within the range of 150 – 200°C and maintained at this range for 60 – 120 s. Next, the soldering temperature is ramped up to the peak temperature in the range of 245 – 260°C, with ramp-up rate of 3°C/s or below. The assembly is then soaked at this temperature for approximately 30 s to reduce the temperature difference between the substrates and solder. Lastly, it is cooled down to room temperature at a rate of 6°C/s or below and formed a solder joint upon solidification. The time maintained above the liquidus temperature of the solder is approximately 60 – 150 s. The time to heat the assembly from room temperature to peak temperature is not more than 8 min.

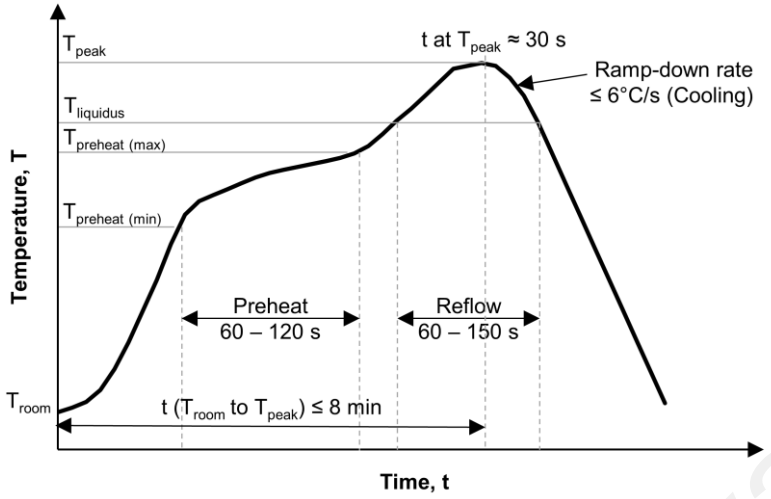

Figure 2.1: Reflow soldering profile recommended by IPC/JEDEC joint industry standard (J-STD-020D-01A)

2.4 Microstructural evolution and interfacial interactions in lead free solder joint during reflow soldering

The reliability of a solder joint is affected greatly by the microstructure of the solder joint (including the solder matrix microstructure and microstructure at the substrate/solder interface) as it determines the mechanical properties of the solder joint. Therefore, it is crucial to understand the microstructural evolution and the reaction between the solder and the substrate at the interface during reflow soldering process, as it determines the initial microstructure of the solder joint. Since the current electronic packaging industry is demanded for lead free soldering, the material combination of copper (Cu) substrate and SAC solder is selected as the focus of this study due to its conventional value in the electronic packaging industry. The fundamental studies on the reaction between these materials during reflow soldering process are reviewed in details in the following section.

2.4.1 Preheat

The application of flux on the PCB or using solder paste that contains flux is a common practice to prevent the soldering materials from oxidation and facilitate the wetting of

molten solder on the substrate during soldering. Therefore, it is necessary to preheat the soldering assembly in order to allow the flux to evaporate in a proper manner and reduce the temperature shock in the assembly. Preheating with an appropriate ramp rate and time is demanded as well or else it could lead to soldering failures, such as bridging, spattering, tombstoning, skewing, wicking, opening, component cracking, voiding, and poor wetting (N. C. Lee, 1999; Srivalli et al., 2015).

As mentioned earlier, the assembly is heated to a temperature below the solder liquidus temperature during the preheating stage. Both the SAC solder and the Cu substrate are in solid state and thus, there is no obvious interfacial reaction between them. However, a trace amount of Sn atoms from the solder and Cu atoms from the substrate may diffuse into the flux, according to the Gong, Liu, Conway, and Silberschmidt (2009).

2.4.2 Reflow

As the soldering assembly is continually heated to the solder liquidus temperature, the solder is fully molten and spread on the Cu substrate. Initially, the Cu atoms from the substrate will dissolve rapidly and thus, a very high concentration of Cu can be realized locally in the vicinity of Cu/molten SAC interface (Laurila, Vuorinen, & Kivilahti, 2005). Based on the concept of local nominal composition introduced by Rönkä, van Loo, and Kivilahti (1997), solid IMC starts to form when the composition of Cu and Sn at the Cu/molten SAC interface reaches the local (metastable) equilibrium. As can be seen from the binary Cu-Sn phase diagram (Figure 2.2), ε-Cu_3Sn (orthorhombic) and η-Cu_6Sn_5 (hexagonal) are the two IMCs that can be formed at the interface. However, Cu_6Sn_5 IMC is considered to be the first phase to form at the Cu/molten SAC interface as a result of heterogeneous nucleation (Laurila et al., 2010). The findings in the review of Ai Ting Tan, Tan, and Yusof (2016) has further supported that Cu_6Sn_5 IMC is more favorable as its formation requires lower activation energy, compared to the formation of Cu_3Sn IMC.

The formation of interfacial Cu_6Sn_5 IMC reduces the composition of Cu in the molten SAC region adjacent to the substrate, leading to further dissolution of Cu from the substrate.

In the study of Gong, Liu, Conway, and Silberschmidt (2008), the initial interfacial Cu_6Sn_5 IMC formed was in a layer consisted of single hemispherical grain (also known as scallop morphology). However, the morphology of Cu_6Sn_5 IMC grains is depending on the solder composition. The grain is hemispherical or scallop-shaped when a near eutectic or eutectic solder is used. In contrary, the grain is faceted when the solder composition is far away from the eutectic composition (Suh, Tu, Lutsenko, & Gusak, 2008; Tu, 2007). Moreover, the morphology of the Cu_6Sn_5 IMC grains might not be uniform due to the possible uneven distribution of Cu atoms along the SAC/Cu joint interface. The IMC layer had an elongated scallop shape in some studies owing to the excessive Cu atoms at certain region in the joint (Laurila et al., 2010; Tsao, Wu, Cheng, Fan, & Chen, 2013).

When the soldering assembly is further heated to the peak soldering temperature, it is held at this temperature for approximately 30 s in order to obtain a uniform temperature distribution throughout the assembly and allow the molten solder to spread or wet on the substrate more thoroughly. The Cu_3Sn (formed at the Cu/Cu_6Sn_5 interface) and Cu_6Sn_5 IMC continue to grow during this period of time (Gong et al., 2008; Y. Tang, Li, & Pan, 2013). Several IMC growth mechanisms at this stage have been reported and they will be discussed in the next section.

Excessively high peak temperature is avoided as it could lead to soldering defects, such as delamination, charring, cold joints, excessive IMC formation, leaching, brittle solder joint and possibly dewetting due to oxidation (N. C. Lee, 1999; Srivalli et al., 2015).

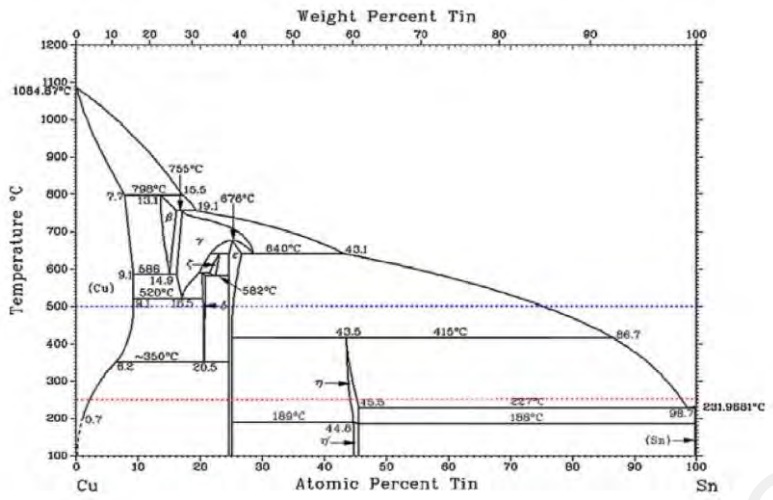

Figure 2.2: Binary Cu–Sn phase diagram (adapted from Laurila et al. (2010) with permission)

2.4.3 Cooling

When the soldering assembly is subjected to subsequent cooling, the solubility of Cu and Sn atoms decreases as the temperature decreases. As the temperature drops below the solder liquidus temperature, the diffused Cu atoms near the Cu_6Sn_5/SAC interface precipitate locally and nucleate heterogeneously on top of the existing interfacial Cu_6Sn_5 IMC (due to lower energy state requirement). The diffused Cu atoms, however, might not be evenly distributed across the interface, thus there are areas where not all the Cu atoms are precipitated on the existing interfacial Cu_6Sn_5 IMC. Instead, these surplus of Cu atoms could form Cu_6Sn_5 IMC whisker (as shown in Figure 2.3) that grows into the solder matrix of the solder joint (Laurila et al., 2005). On the other hand, the Cu_3Sn IMC layer remains as a very thin and planar layer, and sometimes, could not be observed by scanning electron microscopy due to low soldering temperature or short soldering time (Kotadia, Mokhtari, Clode, Green, & Mannan, 2012; Li, Agyakwa, & Johnson, 2012).

Apart from the Cu/SAC interface, the molten SAC solder undergoes undercooling upon its solidification. The first solid phase that formed in the molten SAC solder is either Ag_3Sn or β-Sn, depends on the content of Ag and the cooling rate. The undercooling for

Ag_3Sn nucleation (7.2°C) is much smaller than the undercooling for β-Sn nucleation (29°C) (Mei, 2005). Therefore, if the Ag content is near the eutectic composition and the cooling rate is slow, solid Ag_3Sn phase nucleates first and may grow into large plate-like structure. Otherwise, solid β-Sn phase nucleates homogenously when large undercooling is reached and morphs into a dendritic structure. When the temperature drops to the solder solidus temperature, ternary eutectic reactions take place in the remaining unreacted molten solder at the interdendritic region and form eutectic phase that consists of fine dispersion of Ag_3Sn and Cu_6Sn_5 phases in β-Sn matrix, as illustrated in Fig. 2.4 (Liang, Dariavach, & Shangguan, 2007; Mei, 2005).

The cooling rate of reflow soldering process has a significant influence on the initial microstructure of solder joint. Slow cooling rate might cause thick IMC growth, weak fatigue resistance and solder detachment. Whereas, fast cooling rate could refine the microstructure but at the same time, induce high thermal stress in the solder joint and resulting in internal cracking of solder joint and delamination of the PCB (N. C. Lee, 1999; Srivalli et al., 2015).

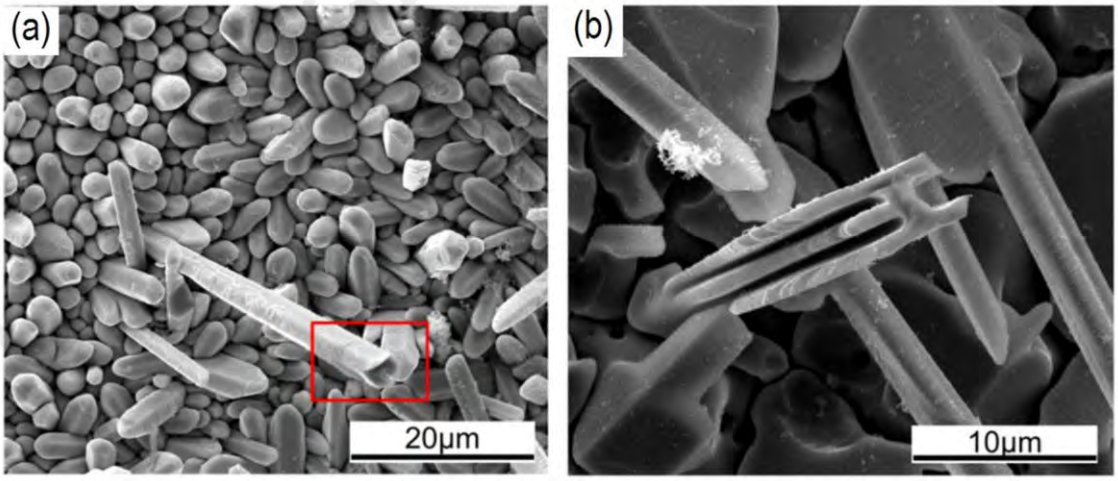

Figure 2.3: Morphology of Cu_6Sn_5 whiskers; (a) hexagonal and (b) acicular (adapted from Tian, Zhang, Hang, Niu, and Wang (2014) with permission)

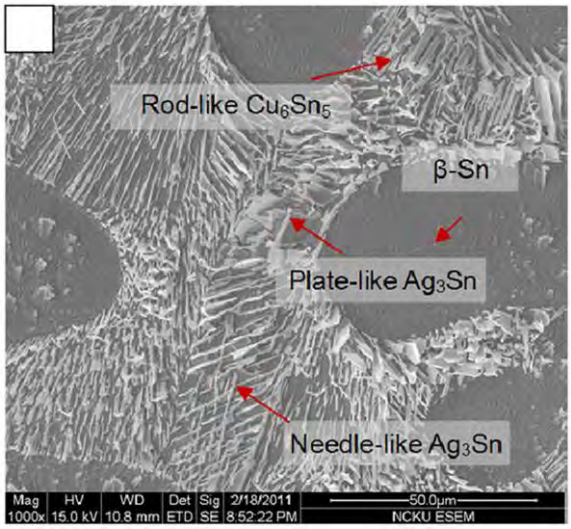

Figure 2.4: Microstructure of air-cooled Sn-3.0Ag-0.5Cu solder (adapted from H.-T. Lee and Huang (2016) with permission)

2.4.4 Growth mechanism of interfacial IMCs during liquid-solid state diffusion

During reflow stage, the Cu_3Sn and Cu_6Sn_5 IMC layers will continue to grow and their growth mechanisms were reported to be different with the reflow time. For the growth of Cu_3Sn IMC, most of the works indicated that this IMC layer grew slightly with increasing reflow time, which formed a thin and planar morphology underneath the Cu_6Sn_5 IMC grains (Gagliano & Fine, 2001; Park & Arróyave, 2012; Y. Tang et al., 2013). This is because the formation of Cu_3Sn IMC requires higher activation energy compared to Cu_6Sn_5 IMC (Ai Ting Tan et al., 2016).

For the growth mechanism of Cu_6Sn_5 IMC layer, it was reported that its mechanism varied with the reflow time (Gagliano & Fine, 2001; Gong et al., 2008; Y. Tang et al., 2013; Z. Zhang, Li, & Wang, 2013). Based on the work of Y. Tang et al. (2013), Gagliano and Fine (2001), Qu, Zhao, Zhao, Huang, and Ma (2014), and Z. Zhang et al. (2013), the Cu_6Sn_5 IMC growth during short reflow time (less than 1000s) was dominated by grain thickening and coarsening. The newly formed Cu_6Sn_5 IMC grains had a scallop shape and were separated from each other. The Cu atoms from the substrate diffused through the channels in between the separated grains and formed Cu_6Sn_5 IMC

particles in the solder matrix. These particles tend to deposit on the larger Cu_6Sn_5 IMC grains according to the Gibbs-Thomson effect, which states that the solubility of a particle is higher when the particle size or curvature is smaller (Ely, Edwin García, & Thommes, 2014; Perez, 2005). Therefore, the grains grew upward or thicken, as depicted in Figure 2.5(a). Meanwhile, the grains grew larger (grain coarsening) due to the Ostwald ripening effect, which describes the dissolution of smaller adjacent IMC grains into molten solder and then redepositing on the larger adjacent grains (Baldan, 2002). The mechanism is illustrated in Figure 2.5(b). The IMC grains continued to thicken and coarsen with reflow time, and eventually closed off the channels in between the grains.

The channels in between the IMC grains were completely pinched off when the reflow time exceeded 1000 s. The diffusion rate of Cu atoms reduced as they were forced to diffuse through the thick IMC layers. Hence, the Cu_6Sn_5 IMC grains are more likely to be coarsen rather than thicken. However, the coarsening rate of Cu_6Sn_5 grains was found to be reduced as well due to the formation of Cu_6Sn_5 whiskers on top of the existing scallop grains. This is associated with the excessive Cu atoms, which are supposedly present in the molten solder between the scallops, have been flowed into the region beyond the grains by convection during reflow stage. They reacted with Sn atoms and grew on the tops of the scallops to form cusps instead of larger grains. As the reflow time increased, grain coarsening was further hindered by the elongation of these cusps into hexagonal shaped whiskers which are hollow, with flat ends, and sometimes in acicular shape (refer to Figure 2.3)(W. Liu, Tian, Wang, Wang, & Liu, 2012; Tian et al., 2014).

When the reflow time prolonged further, the growth of Cu_6Sn_5 IMC was mainly dominated by grain coarsening, according to Gagliano and Fine (2001). The diffusion of Cu atoms was hindered by the growth of Cu_3Sn IMC and Cu_6Sn_5 IMC layers. The source for grain coarsening mainly originated from the broken whiskers which were caused by

the turbulence within the molten solder. The morphological change of both Cu_6Sn_5 and Cu_3Sn IMCs at different reflow time has been summarized in Table 2.1.

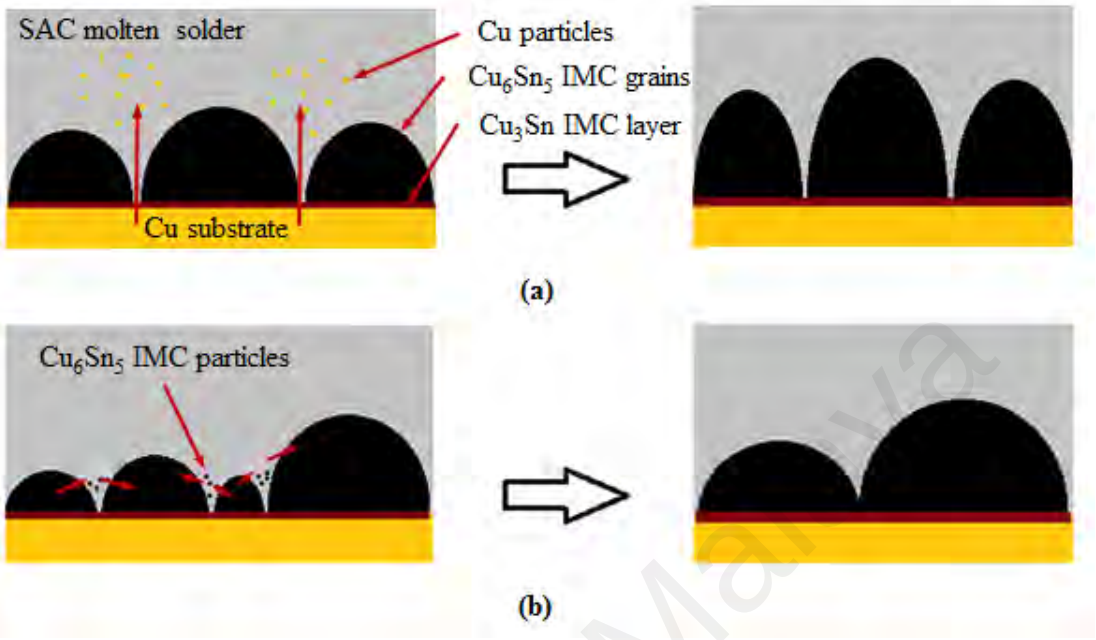

Figure 2.5: Schematics of (a) grain thickening and (b) grain coarsening

Table 2.1: IMC morphological change during reflow stage

Type of IMC	Morphology of IMC at different reflow time		
	Short (<1000 s)	**Long (>1000 s)**	**Prolonged**
Cu_6Sn_5	Continuous scalloped (due to grain thickening and coarsening mechanism)	Scalloped grains coarsen (dominant) and thicken, formation of Cu_6Sn_5 whiskers (either hollow hexagonal or acicular shape) on top of scalloped grains	Scalloped grains continue to coarsen, long Cu_6Sn_5 whiskers may break and flow into solder matrix
Cu_3Sn	Planar, very thin layer	Planar, thin layer	Planar, thin layer

2.5 Reliability of lead free solder joint

Solder joint reliability is defined as the probability that the solder joint can perform its intended function under specified operating conditions for a specified time interval. With the global trend towards miniaturization and multi-functionalization of electronic devices, the reliability of lead free solder joints in these devices is mainly degraded by creep,

thermal fatigue and electromigration phenomenon. These devices are continuously exposed to temperature fluctuations during service condition due to the heat dissipation of the internal electronic components and the temperature change in the service environment. The temperature fluctuations induce thermomechanical strains in the lead free solder joints due to the thermal expansion mismatch between the soldering assemblies (known as creep phenomena). Besides, depending on the application, some of the electronic devices are constantly exposed to high service temperature or kept inactive in such condition for long times between service cycles (known as thermal fatigue phenomena). Furthermore, the increasing current density on the solder joint (due to miniaturization) has promoted the material degradation through mass transport of atoms in the solder joint (known as electromigration phenomena) (Laurila et al., 2012). Therefore, reliability tests such as thermal aging, thermal cycling and electromigration tests are commonly used in research to simulate the alteration of joint microstructure and properties under different service conditions. To provide a fundamental background, the evolution of microstructure and mechanical properties of Cu/SAC solder joint under different reliability test conditions will be reviewed in the following section.

2.5.1 Thermal aging

Thermal aging test (also known as isothermal aging) is used to observe the degradation of joint properties when the solder joint is subjected to a constant temperature for over a long period of time. Based on the literatures, the as-soldered joint is usually aged up to 2000 h, under the aging temperature range of 100-170°C (Haseeb & Leng, 2011; Hodúlová, Palcut, Lechovič, Šimeková, & Ulrich, 2011; Tay, Haseeb, Johan, Munroe, & Quadir, 2013; Y. W. Wang, Lin, Tu, & Kao, 2009).

Laurila et al. (2012) reported that the thermal aged Cu/SAC solder joint had similar solder matrix microstructure with the as-soldered joint, in which both contained

β-Sn dendrites and a large volume fraction of eutectic phase at the interdendritic region. The main difference was that the solder matrix microstructure coarsened after thermal aging. The β-Sn dendrites evolved to a more globular-like structure and a large amount of coarse Cu_6Sn_5 and Ag_3Sn bulk IMCs precipitated in the solder matrix. Accordingly, the volume fraction of finely dispersed eutectic phase decreased after thermal aging. The coarsening phenomena is caused by the tendency of the soldering system to minimize its surface energy by coalescence of small IMC particles into large IMC precipitate to reduce the boundary area.

Microstructural change was also observed at the interfacial IMC layers of the Cu/SAC solder joint. As mentioned earlier, the scallop-shaped Cu_6Sn_5 and the thin and planar Cu_3Sn are the two main IMC layers that would present in the as-soldered Cu/SAC joint. The thickness of both IMC layers increased after thermal aging due to the solid-state diffusion between Cu and Sn atoms. The channels between the Cu_6Sn_5 scallops served as the convenient path for the diffusion of Cu atoms, resulted in rapid IMC growth at the channels rather than on the top surface of the scallops during initial aging stage (Jun Shen, Zhao, He, & Pu, 2013; L. Zhang, Xue, Zeng, Gao, & Ye, 2012). Hence, the Cu_6Sn_5 IMC layer changed from scallop to planar morphology. On the contrary, the Cu_3Sn IMC layer remained planar but thicken significantly with aging temperature and time (Peng, Monlevade, & Marques, 2007; Jun Shen, Zhao, et al., 2013). However, there might be a change in the lattice structure of Cu_3Sn, according to Mookam and Kanlayasiri (2012), who observed the presence of Cu_3Sn in both orthorhombic and hexagonal lattice structures in the joint interface after aging for 1000 h at 100°C. The alteration of lattice structure might affect the slip mechanism of the solder joint when being subjected to mechanical forces.

Kirkendall voids were found at the Cu/Cu_3Sn interface and within the Cu_3Sn IMC layer in the thermally aged Cu/SAC solder joint. The formation of Kirkendall voids is

attributed to the faster diffusion of Cu atoms than Sn atoms during thermal aging condition, in which the atomic level vacancies left by the migrating Cu atoms on the substrate are not filled by Sn atoms. These vacancies coalesce into voids at the interface region, which are named as Kirkendall voids (Peng et al., 2007; Tz-Cheng, Kejun, Stierman, Edwards, & Ano, 2004). The density of the voided area would increase with aging time and temperature, leading to brittle fracture at the joint interface (P. Liu, Yao, & Liu, 2009; W.-m. Tang, He, Liu, & Ivey, 2010; Tz-Cheng et al., 2004; Y. W. Wang et al., 2009).

The growth of Cu_3Sn IMC layer during thermal aging is mainly governed by the inter-diffusion between the Sn atoms diffused through Cu_6Sn_5 IMC layer and the Cu atoms from metal substrate at the Cu/Cu_3Sn interface (C.-Y. Liu, Lai, Wang, & Hon, 2006; Mookam & Kanlayasiri, 2012; Peng et al., 2007). The interfacial reaction can be expressed by Equation 1 (Mookam & Kanlayasiri, 2012). The growth of Cu_3Sn IMC layer could also be contributed by Cu atoms diffused through Cu_3Sn to Cu_3Sn/Cu_6Sn_5 interface (P. Liu et al., 2009; Mookam & Kanlayasiri, 2012; Peng et al., 2007; L. Zhang et al., 2012). The reaction is described in the Equation 2.

As for Cu_6Sn_5 IMC, its growth is governed by the reaction (as stated in Equation 3) between Cu and Sn atoms available in the Cu_6Sn_5/solder interface. Due to the reaction in Equation 2, the amount of Cu atoms diffused from metal substrate to Cu_6Sn_5/solder interface is greatly reduced as the Cu_3Sn layer thicken with aging time. Meanwhile, the Cu supply from the solder is limited as most of the Cu atoms have been used to form Cu_6Sn_5 IMC precipitates in the solder matrix (L. Zhang et al., 2012). Therefore, the growth of Cu_3Sn IMC is more significant as compared to the Cu_6Sn_5 IMC during thermal aging.

$$3Cu + Sn \rightarrow Cu_3Sn \quad \text{(Equation 1)}$$

$$Cu_6Sn_5 + 9Cu \rightarrow 5Cu_3Sn \quad \text{(Equation 2)}$$

$6Cu + 5Sn \rightarrow Cu_6Sn_5$ (Equation 3)

However, in the case where the supply of both Cu and Sn atoms is very sufficient, the growth of IMCs in the solder joint is determined by the required activation energy to form that particular IMC. Therefore, several approaches have been taken to calculate the activation energy of Cu_6Sn_5 and Cu_3Sn IMC formation and one of the famous approaches is to derive the activation energy from the data acquired through thermal aging test (Kim, Roh, Kim, & Kim, 2010; Mookam & Kanlayasiri, 2012; Yoon, Noh, Kim, Shur, & Jung, 2009; L. Zhang et al., 2012). The details of the derivation are presented in the following section.

2.5.1.1 Calculation of IMCs' activation energy

Activation energy of a reaction is the minimal energy required for the reaction to occur. The lower the activation energy, the higher the thermodynamic stability of the reaction. In other words, the growth of IMC is faster when the required activation energy is lower, but with the condition of sufficient supply of reactants. Over the years, studies have been conducted to determine the activation energy for the formation of Cu_6Sn_5 and Cu_3Sn IMC and the following is the summary of the calculation method.

As the growth of IMCs during thermal aging is governed by solid-state diffusion mechanism or more precisely lattice diffusion dominated diffusion mechanism (Jun Shen, Zhao, et al., 2013), the relationship between IMC layer thickness and aging time can be expressed by the following equation (Rizvi, Chan, Bailey, Lu, & Islam, 2006; L. Zhang et al., 2012):

$$x_t - x_0 = (D_{eff}t)^{1/2} \quad \text{(Equation 4)}$$

where t is the aging time, x_0 is the IMC thickness of the as-soldered joint, x_t is the IMC thickness at aging time, t and D_{eff} is the effective diffusion coefficient of IMC during thermal aging. By plotting the graph of IMC thickness, x_t against square root of aging

time, $t^{1/2}$, the D_{eff} of both IMCs can be determined from the slope of the linear curve. The activation energy for each IMC can be determined by the Arrhenius equation as expressed in the equation:

$$D_{eff} = D_0 e^{-Q/RT} \quad \text{(Equation 5)}$$

where D_0 is the temperature-independent diffusion coefficient, Q is the activation energy, R is the universal gas constant and T is the absolute temperature in Kelvin. By taking logarithm of Equation 5, the equation can be expressed as follows.

$$\ln D_{eff} = \ln D_0 - \frac{Q}{R}\left(\frac{1}{T}\right) \quad \text{(Equation 6)}$$

The activation energy of the IMC can be obtained by calculating the slope of the plot of efficient diffusion coefficient ($\ln D_{eff}$) against inverse aging temperature (1/T). The activation energy of Cu_6Sn_5, Cu_3Sn and (Cu_6Sn_5 + Cu_3Sn) IMCs obtained from several studies are listed in Table 2.2. From the table, the activation energy is the lowest for Cu_6Sn_5 IMC but the highest for Cu_3Sn IMC, regardless of the solder composition. This indicates that the formation of Cu_6Sn_5 IMC is more thermodynamically stable than the Cu_3Sn IMC. These data are consistent with the observation in which the Cu_6Sn_5 IMC layer is usually thicker than the Cu_3Sn IMC layer. The variation in between the reported activation energy might be attributed to the Cu substrate used in each study. The grain size, energy state, and purity of the Cu substrate could affect the diffusivity of Cu atoms (N. Huang, Hu, & Li, 2013; Peng et al., 2007).

Table 2.2: Activation energies obtained from literature studies

Solder	Aging temperature, °C	Aging time, h	Activation energy, kJ/mol			Ref.
			Cu_6Sn_5	Cu_3Sn	(Cu_6Sn_5 + Cu_3Sn)	
SAC 037	100-170	0-1000	51.59	119.04	80.65	(Mookam & Kanlayasiri, 2012)
SAC 305	100-170	0-672	58.3	114.7	75.1	(Yoon et al., 2009)
SAC 355	120-180	0-2000	69.42	91.88	79.79	(Kim et al., 2010)
SAC 387	100-140	0-720	61.4	105.8	73.5	(L. Zhang et al., 2012)
SAC 387	100-150	0-1000	-	119.8	-	(Peng et al., 2007)
SAC 387	75-175	0-1008	52.27	80.69	77.7	(Tay et al., 2013)

2.5.2 Thermal cycling

When the electronic devices are continuously exposed to temperature fluctuations during service condition, the coefficient of thermal expansion (CTE) mismatch between the electronic components and the PCB generates cyclic thermal stresses and strains in the solder joints and leading to thermal fatigue failures (Jun Shen, Zhao, et al., 2013; L. Zhang et al., 2012).

Thermal cycling test (also called as thermo-mechanical fatigue test) is used to determine the joint ability to resist extremely high and low temperature, as well as to withstand cyclical exposures to these temperature extremes. It is used to accelerate the occurring of joint fatigue failures under cyclic stress and strain (Teo & Sun, 2008; L. Zhang et al., 2012). During thermal cycling test, the as-soldered joint is heated in a furnace with the temperature ranging from -40 to +150 °C for 0 to 2000 cycles in general. The ramp rate is approximately 10 °C/min and the dwell time at each extreme temperature

is about 10 min. The joint is then air cooled to room temperature after reaching the desired thermal cycles (Han et al., 2012b).

Coarsening of solder matrix microstructure after thermal cycling, accompanied by gradual rotation of small volumes in the stress concentration regions were observed in the work of Hokka, Mattila, Xu, and Paulasto-Kröckel (2013) and Laurila et al. (2012). The β-Sn dendrites coalesced into large structure and the Cu_6Sn_5 and Ag_3Sn IMC precipitates coarsened at the expense of the eutectic phase, resulted in the gradually disappearance of eutectic phase in between the large β-Sn phases. When the stress level was sufficiently high (depending on the thermal cycling test condition), the solder matrix in the stress concentration region underwent recrystallization and formed new grains to release the stress. The solder matrix transformed into equiaxed grain structure, with a network of high-angle grain boundaries surrounding the recrystallized grains. These high-angle grain boundaries favored the intergranular crack propagation between the recrystallized grains in the solder joint, as reported by Hokka et al. (2013). In other words, the solder joint, which has undergone severe recrystallization, is lower in strength because the intergranular crack propagation requires less energy consumption as compared to the transgranular crack propagation.

At the Cu/SAC interface, the thickness of both Cu_6Sn_5 and Cu_3Sn IMC layers increased with the number of thermal cycles and the morphology of Cu_6Sn_5 IMC changed from scallop-like to planar (Lihua et al., 2009; L. Zhang et al., 2012). Shen et al. (Jun Shen, Zhao, et al., 2013) reported that the growth of both IMCs during thermal cycling was faster than during thermal aging. Moreover, the Cu_6Sn_5 IMC grown faster than Cu_3Sn IMC during thermal cycling, which is the total opposite to those during thermal aging. The authors compared the growth behavior during thermal aging and thermal cycling by using equivalent aging duration parameter, in which t_{eff} is defined as total accumulated

dwell duration. The growth of total IMC layers under both thermal conditions can be explained by the following equation:

$$x - x_0 = At_{eff}^n \quad \text{(Equation 7)}$$

where x is the total thickness of both IMC layers at time t_{eff}, x_0 is the as-soldered total thickness of IMC layer, A is the growth constant and n is the time exponent. The n value obtained for thermal aging and thermal cycling tests was 0.51 and 0.6, respectively, indicating that the IMC growth is faster during thermal cycling. The increase in IMC growth rate is contributed by (1) lattice diffusion and grain boundary diffusion paths for Sn atoms due to the recrystallization occurred during thermal cycling, and (2) faster diffusion of Cu atoms due to higher thermal mechanical stress.

Cu/SAC interface is usually the stress concentration region under service condition and thus, recrystallization is usually occurred at the interface. Once the recrystallization is initiated, the recrystallized volume expands gradually from the initial recrystallization region towards the other region within the solder joint. As a result, the Sn atoms in the solder could diffuse into the solder/IMC interface by lattice diffusion and grain boundary diffusion during thermal cycling. In comparison to thermal aging (which is dominated by lattice diffusion), there is an additional diffusion path during thermal cycling and the diffusion through grain boundary is claimed to be faster than lattice diffusion (Jun Shen, Zhao, et al., 2013). On the other hand, thermal mechanical stress is generated in the solder joint due to the temperature variation during each thermal cycle. This promotes the diffusivity of Cu atoms from the substrate into the solder joint, leading to the growth of interfacial IMCs during thermal cycling (Jun Shen, Zhao, et al., 2013; Zeng et al., 2010). Since the supply of Cu and Sn atoms is comparatively sufficient during thermal cycling, the Cu_6Sn_5 IMC would grow faster than the Cu_3Sn IMC. This is consistent with the observation of Zhang et al. (L. Zhang et al., 2012) and Han et al. (Han et al., 2012a).

2.5.3 Electromigration

A lead free solder joint can be served as an electrical, mechanical and thermal interconnection in an electronic device. When electric current passes through a solder joint during service condition, it induces the transport of metal atoms in the solder joint along the electron flow direction from cathode to anode terminal. This phenomena is known as electromigration. To date, the increasing current density due to the demands for miniaturization and performance have accelerated the rate of electromigration in lead free solder joints. Furthermore, these solder joints are exposed to greater Joule heating (heat generated by the passage of electric current) as Joule heating is proportional to the square of the current density. In other words, the solder joints are subjected to high local temperature rise, which would further induce atom diffusion in the lattice of solder joints (Chan & Yang, 2010). Therefore, to assess the effect of electromigration in an operating lead free solder joint, the solder joint is usually subjected to current density up to the magnitude of 10^4 A/cm^2 in an isothermal condition ranging from 100 to 150°C for hundreds of hours.

Based on the work of Chan and Yang (2010) and Laurila et al. (2012), coarsening of Cu_6Sn_5 and Ag_3Sn IMC precipitates was observed in the solder matrix of Cu/SAC solder joint. The authors proposed that the phase coarsening was attributed to the diffusion induced by current stressing and the accompanying Joule heating. Furthermore, rotation of β-Sn grains was observed in the work of Wu, Gusak, Tu, and Kao (2005) and Wua and Hsieh (2008). The β-Sn grains reoriented and realigned along the current flow to reduce the resistance under electric current stressing. This may promote the diffusion of Cu atoms, typically along the c-axis of the β-Sn crystal (Bieler et al., 2012).

At the Cu/SAC interface, high current stressing and the accompanying Joule heating promote the interstitial diffusion of Cu atoms from the substrate into the SAC solder at the cathode terminal. As similar to the formation mechanism of Kirkendal voids

during thermal aging, the divergence of atomic flux near the current crowding region causes the accumulation of vacancies, leading to the formation of voids in this region. As the growth of voids would induce redistribution of the current, the voids develop along the Cu/SAC interface and eventually lead to open circuit failure (Chan & Yang, 2010).

Apart from the void formation, rapid interstitial diffusion of Cu atoms into the solder promotes the growth of interfacial IMCs. However, the IMC growth at the cathode is different to those at the anode, due to the polarity effect of electrons flow. Studies have shown that the IMC growth at the cathode was retarded as compared to the IMC growth at the anode (M. L. Huang, Zhao, Zhang, & Zhao, 2015; Laurila et al., 2012; Y.-A. Shen & Chen, 2017). This was attributed to the electromigration of Cu atoms into solder and the dissolution of IMC at the cathode induced by current stressing and Joule heating, according to Chan and Yang (2010). When the solder joint is subjected to prolonged current stressing, the cathode is in tension and the anode is in compression due to the mass transport from cathode to anode by electric current. Sn grains could be extruded out from the free surface at anode, in the form of hillock or whisker, in order to release the compressive stress (Tu, 1994). The growth of Sn whisker is further accelerated by the increase of current density (Lin, Lai, Lin, Tu, & Kao, 2008).

2.6 Proposed solutions to improve reliability of lead free solder joint

Based on the aforementioned studies, it is noticed that the reliability of lead free solder joint is determined by the degree of microstructural evolution during service conditions. In other words, the solder joint reliability can be improved if the microstructural evolution of solder joint is limited or under-controlled. Therefore, the developments of new and ever-improving soldering materials and processes are regarded as the key solutions to achieve this goal. The current state and research progress on these two aspects are presented in the next section.

2.6.1 Development of composite lead free solder

Lead free solders with incorporated reinforcement are known as composite lead free solders. They are termed as nano-composite solders when the reinforcement is on nano-scale. The melting temperature of these nano-composite solders is similar to the SAC solders, thus allowing them to replace the SAC solders in the industry without the need to purchase any new equipment or change the process parameters. The purpose of adding reinforcement into lead free solders is to strengthen the solders by particles dispersion, which can improve the solder deformation resistance by impeding the movement of dislocation and pinning the grain boundaries in the solder matrix (J.-S. Lee et al., 2008; Mohankumar & Tay, 2004). Besides, the nano-reinforcement could restrict the diffusion activity of the relevant elements in the solder joint through particle adsorption mechanism. This could prevent the excessive growth of IMCs and reduce the degree of solder matrix coarsening during service conditions (Laurila et al., 2010; Tay et al., 2013; Tsao, Huang, Chung, & Chen, 2012; Tsao et al., 2013).

A number of nano-reinforcements have been investigated, including metallic, ceramics and carbon-related nano-particles. There are several preparation methods for nano-composite solders and there are some conditions to be obeyed for each preparation method (J. Shen & Chan, 2009). It was reported that the added nanoparticles were not completely incorporated into the SAC solder after soldering (Tay et al., 2013; Wilde & Perepezko, 2000). The particles could be rejected, engulfed or entrapped in the molten solder, depending on the interaction mechanisms between the particles and the solder. The particles could also be dispersed into the solder flux rather than into the solder matrix.

Based on the review of Laurila et al. (2010) and Ai Ting, Ai Wen, and Farazila (2015), the nano-reinforcements can be categorized the into three general groups: (1) element that dissolves in Cu-Sn IMC, (2) element that does not dissolve in Cu-Sn IMC and (3) element that reacts with Cu to form new IMC. For example, Ni, Co and Ni-coated-

carbon nanotube are considered as group (1) elements as they dissolved into Cu_6Sn_5 IMC and formed $(Cu,Ni)_6Sn_5$ and $(Cu,Co)_6Sn_5$, respectively. These new IMCs are more thermodynamically stable than Cu_6Sn_5 IMC and would not easily decompose to Cu_3Sn, especially during thermal aging and thermal cycling. However, they have the tendency to promote Cu_6Sn_5 IMC growth and suppress the formation of Cu_3Sn IMC at the same time. This implies that a better control of the process parameters is required while using these elements as their suppressing effect might be very dependent on the parameters, such as temperature and time. Al, Mo, Al_2O_3, TiO_2, ZrO_2 and carbon nanotube are considered as group (2) elements. This group of elements could reduce the growth of Cu-Sn IMCs in a solder joint by adsorption effect. They are also considered as non-reacting elements since they have a stable suppression effect on Cu-Sn IMCs, regardless of temperature and time. As for group (3) elements, a typical example of this is Zn, as it could react with Cu directly to form Cu_5Zn_8 IMC layer on top of the Cu_6Sn_5 IMC when the Zn content is above 1.0 wt%.

The literatures above also reported that the amount of addition is very crucial in regulating the growth of Cu-Sn IMCs. When an excessive amount of nanoparticles is added into the joint, the wettability of molten solder on the substrate would be reduced due to higher viscosity. It could promote the formation of IMC at the same time, especially when using group (3) elements. Furthermore, excessive nanoparticles would agglomerate and result in the formation of microvoids at the joint interface.

Although satisfactory performance has been obtained in many studies using different types of proposed composite lead free solder, the question of the optimum type of composite solder with reliable overall performance has not been addressed to date and is still in progress. There has been some recent development on the fabrication of new composite solders by adding new ceramic, carbon-related and polymeric nanoparticles such as ZnO (Fawzy et al., 2014), Y_2O_3 (Yang & Zhang, 2013a), SiC (El-Daly, Fawzy,

Mansour, & Younis, 2013a, 2013b), Si_3N_4 (M.A.A et al., 2011), graphene nanosheet (Y. L. Huang, Xiu, Wu, Tian, & He, 2016) and polyhedral oligomeric silsesquioxanes (POSS) (Jun Shen, Tang, et al., 2013). It is reported that these new composite solders showing promising enhancement on the solder and solder joint properties. Therefore, it is foreseen that non-reacting and non-metallic nanoparticles would continue to attract interest as the potential candidate for the fabrication of nanocomposite lead free solder.

2.6.2 Development of reflow soldering process

With the integration of more functions into smaller electronic packages, the intensive heat density generated by the functioning components in the miniature electronic devices has driven the necessity for thermal management on the PCB. The most common solution to cool the components is to increase the thermal conductivity or heat dissipation efficiency between the components and the board. This can be realized by using electronic packages with built-in thermal enhancement feature, such as large area bottom metal or heat sink, to provide a direct thermal path out from the components. The bottom heat sink is directly mounted to the thermal land on the PCB with solder (due to its good thermal and mechanical performance as well as low cost) (Chung et al., 2012; Samanta, 2016). The second approach is to use thermal via that acts as thermal connection between the component soldered on the top side of the PCB to the thermally conductive plane that locates within the board or even the heat sink that attached at the bottom of the board (Schussler et al., 2009).

The use of thermal management features has, however, drawn away the energy from the solder during reflow soldering due to the large thermal mass of the thermal management materials. The non-homogeneous heat distribution would lead to either insufficient reflow of the solder or overheating the part of the soldering assembly with no thermal management feature or smaller component size (Schussler et al., 2009). Therefore,

reflow soldering techniques that utilize different heat transfer mechanism have been developed over the years. Among the available techniques, infrared and convection reflow, vapor phase reflow and laser reflow are the most satisfying techniques for the electronics packaging industry. These techniques offer several distinct advantages but with limitations.

2.6.2.1 Infrared and convection reflow

Infrared and convection reflow soldering is performed in a multiple-zoned oven that contains preheat, reflow and cooling zones. The temperature of each zone can be controlled individually and the soldering assembly is reflowed by passing through the oven on a conveyor belt. Infrared heaters are used to heat the soldering assembly and the surrounding air in the oven. The heated air is forced to flow towards the assembly by fans in the oven. Heat transfer by conduction takes place as well within the soldering assembly Thereby, the heat transfer during infrared and convection reflow soldering results from the combination of radiation, convection and conduction (Lau & Abdullah, 2013). The soldering assembly is sometimes reflowed in an oxygen-free atmosphere to prevent oxidation and improve the wetting of lead free solder. Nitrogen gas is commonly used for this purpose and it was reported that the use of nitrogen gas reduced the peak soldering temperature due to its better heat transmission than the oxygen gas (Schüßler, Kozic, & Franke, 2009).

The main advantages of infrared and convection reflow soldering are its long application history and cost effectiveness for mass production. However, the temperature uniformity across the soldering assembly is still a persisting problem when using this soldering technique. This is attributed to the increasing complexity of the soldering assembly and the variation of component mass within the assembly. Furthermore, shadowing effect (also known as the impedance of heating due to the blocking of heating

medium flow by nearby components) was reported in the study of Dušek and Váňa (2011). Therefore, the recent research of this technique is focused on the development of simulation models or tools to optimize the reflow soldering profile by predicting the thermal distribution of the soldering assembly and monitoring the transient behavior of the solder reflows during the soldering process (S.-S. Deng et al., 2016; Srivalli et al., 2015; Xu et al., 2017).

2.6.2.2 Vapor phase reflow

Vapor phase reflow soldering is also known as condensation soldering as it uses vapor to transfer heat via condensation onto the soldering assembly. The soldering process is carried out in a container or tank and the bottom of the tank is filled with heat transfer liquid, as shown in Figure 2.6. During the soldering process, the heat transfer liquid is heated up to its boiling temperature by heating elements to generate vapor blanket above the liquid surface. The soldering assembly is then immersed into the vapor and a condensate layer (an inert and continuous fluid layer) is formed on the colder surface of the soldering assembly. The chemically inert fluid layer provides an inert atmosphere to the soldering assembly during soldering. The condensation of vapor continues until the assembly reaches the boiling temperature of the heat transfer liquid. The latent heat of condensing mass is transferred to the assembly and the solder "reflows" when the assembly reaches the boiling temperature. The assembly is lifted out of the heating zone at last to allow the molten solder to solidify and allow the condensate layer to evaporate from the assembly (Attila Géczy, Kvanduk, Illes, & Harsányi, 2016; Illés & Géczy, 2016; Synkiewicz, Skwarek, & Witek, 2015).

The most widely used heat transfer fluid up to date is Galden, a liquid medium that contains ether chains closed with carbon-fluorine bonds (Perfluoropolyether, PFPE). The Galden liquid offers a wide range of boiling temperature from 150 to 265°C, based

on the configuration of the ether chain. The Galden liquid is chemically and thermally resistant, non-toxicity and possesses excellent heat transfer coefficient and electric insulation properties, no flash or fire point and low viscosity (Illés et al., 2016; Leicht & Thumm, 2008).

The main advantage of vapor phase reflow over the infrared and convection reflow is the prevention of overheating since the soldering temperature is regulated by the boiling temperature of the heat transfer fluid (Illés et al., 2016). The occurrence of shadowing effect is also possibly avoided when reflowing the soldering assembly with varying component mass distribution (Illés & Géczy, 2016; N.-C. Lee, 2001; Schüßler et al., 2009).

However, the heat transfer during vapor phase reflow is more intense than during infrared and convection reflow, which may cause soldering failures such as voiding, paste sputtering and tombstoning. This is attributed to the excellent heat transfer coefficient of Galden vapor, which is 2-3 times higher than the gas medium used in the infrared and convection reflow (Illés & Géczy, 2016). Therefore, heat transfer by level adjustment method (also known as soft vapor phase) is introduced to achieve a non-linear reflow profile with proper preheating (A. Géczy, Szőke, Illyefalvi-Vitéz, Ruszinkó, & Bunea, 2011; Leicht & Thumm, 2008; Livovsky, Pietrikova, & Durisin, 2008). Apart from the intensive heat transfer issue, Illés and Géczy (2012) and Illés et al. (2016) reported that the condensate layer thickness had considerable effects on the heat transferred to the soldering assembly. The condensate layer thickness that formed on the colder surface of the assembly might be not uniform due to the variation of component mass. This resulted in spatial heat transfer difference which could lead to uneven joint quality and aforementioned soldering failures. Therefore, the authors proposed to incline the soldering assembly during vapor phase reflow to improve the uniformity of the condensate layer thickness. Illés and Géczy (2016) observed that the optimal condensate

layer thickness was achieved by inclination ranging from 1° to 10°. Inclination below 1° was found to cause a greater temperature difference between the opposite edges of the soldering assembly, whereas the inclination above 10° was not recommended by the authors due to the possibility of component displacement on the assembly during soldering.

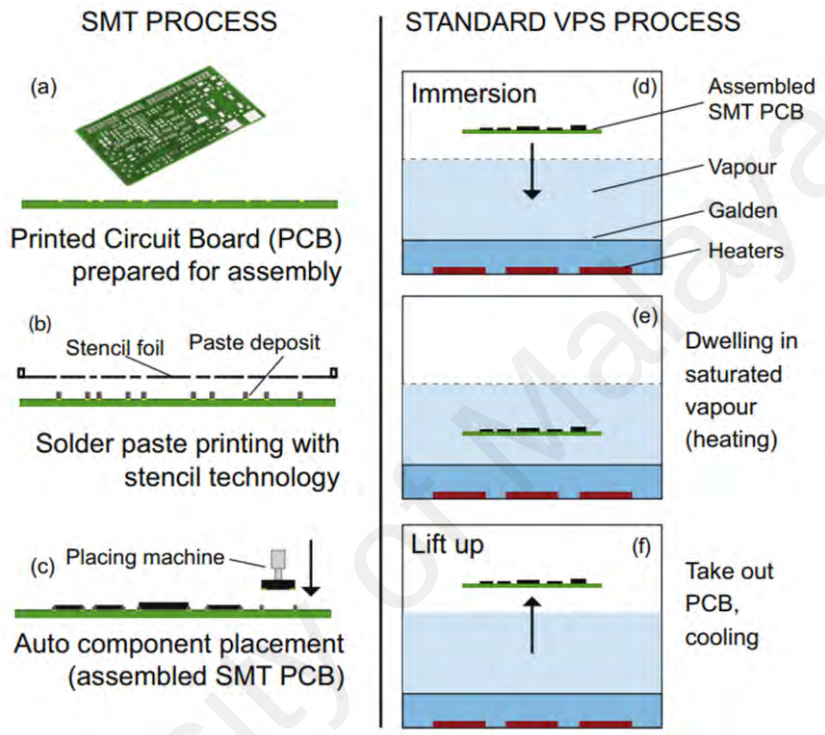

Figure 2.6: Surface mount technology (SMT) and vapor phase soldering (VPS) processes (adapted from with Illés and Géczy (2016) permission)

2.6.2.3 Laser reflow

Laser reflow soldering has become one of the most favored soldering technique in microelectronics industry as it can be adapted to the soldering of temperature-sensitive assembly or assembly with complex and fine-pitch geometry. This process utilizes focused laser beam (generated from a laser source) to transfer energy by radiation to the soldering area and melts the solder with the adsorbed energy. The heating process is contactless and localized and the formation of joint is very rapid due to the rapid heating and cooling mechanism (Ogochukwu, 2013; Reinl, 2013). Thereby, the soldering

assembly is subjected to lower thermal stress and the solder joint has a finer microstructure and thinner IMC layer (Nishikawa & Iwata, 2015).

Despite of its high efficiency and performance, the use of laser reflow soldering in the industry is rather limited. First of all, each solder joint in the soldering assembly has its own thermal mass and reflectivity. As the laser heat input has to be precisely defined for each joint, this makes the selection of laser condition for the entire assembly to be very difficult (Imai et al., 2014). Secondly, the capability of this technique to solder large area is rather limited and the equipment capital for this process is very costly, as it requires laser source, accurate and precise positioning and alignment systems, as well as safety equipment (Jung et al., 2016; Ogochukwu, 2013). Additionally, in the study of Nishikawa and Iwata (2015), a large amount of Kirkendall voids was found in the thermally aged laser-soldered joints that contained extremely fine interfacial IMC grains under as-soldered condition. The authors attributed this to the faster diffusion of Cu atoms from the substrate into the interface through the excessive grain boundaries contributed by the extremely fine IMC grains.

2.6.2.4 Ultrasonic assisted reflow

Over the past decade, several researchers have proposed a new reflow soldering technique by integrating USV (with frequency range of 20-60 kHz) into ordinary reflow soldering process (Chinnam et al., 2011; Hongjun Ji, Qiang Wang, Mingyu Li, & Chunqing Wang, 2014; Ji et al., 2016; Kago et al., 2004). This technique is known as ultrasonic assisted reflow soldering, in which the USV is applied on the soldering assembly during the cooling stage of a reflow soldering process.

Kago et al. (2004) first reported that the Cu/Sn-Bi solder joints obtained better peel strength, refined solder matrix microstructure and thinner interfacial IMC layer after treated with several seconds of 58 kHz USV during the cooling stage in a hot-air reflow

soldering process. In the work of Chinnam et al. (2011), Cu/Sn-4.0Ag-0.5Cu/Cu solder joints with refined solder matrix microstructure, thinner interfacial IMC layer and improved hardness were obtained when treated with 240 seconds of 40 kHz USV within 40 W of ultrasonic power in an ultrasonic assisted oven reflow soldering. Hongjun Ji et al. (2014) and Ji et al. (2016) further examined the effect of ultrasonic power (up to 267 W) on the Cu/Sn-3.0Ag-0.5Cu/Cu solder joint properties by applying 28 kHz USV in a hot-plate reflow soldering. Their studies showed that the ultrasonic-treated solder joints have better shear strength even though the solder matrix microstructure was coarser when treated with USV of 200 W and above.

The reported enhancement on the solder joint properties is contributed by the refinement of solder matrix microstructure and thinner interfacial IMCs formation under the influence of USV, where USV induced nucleation and temperature homogeneity in the solidifying molten solder explains the reported microstructural change. Despite all of the promising results reported, the research on ultrasonic assisted reflow soldering is still in its infancy as only very limited works can be found in the literatures, and hence more extensive studies would be valuable. Moreover, these studies do not report any effect related to the well-known degassing mechanism induced by USV in a liquid medium, which the viscosity of the solidifying molten solder may be the underlying reason.

2.7 Summary

From the literature survey, it is evident that both the development of composite lead free solder and the modification techniques on the reflow soldering process could be used to produce lead free solder joints with enhanced reliability. However, it is relatively simple to generate similar promising results through the modification on the reflow soldering process. Amongst the modification techniques, ultrasonic assisted reflow soldering shows greater potential to produce void-free and reliable lead free solder joints in a cost-effective

manner. Although some works have been carried out in this field, several insights are yet to be explored to fill the gaps of previous research. This includes applying the USV on the soldering assembly before the molten solder enters the cooling stage, where the molten solder is in fully liquefied form. Investigation on the effect of USV parameters such as frequency, power and time should be carried out as well in order to provide in-depth understanding on the ultrasonic application in the soldering industry.

CHAPTER 3: METHODOLOGY

3.1 Ultrasonic assisted reflow soldering system

Figure 3.1 illustrates the general overview on the developed ultrasonic assisted reflow soldering system to be used in the following experimental studies. The whole system is consisted of ultrasonic unit (ultrasonic generator, transducer and horn), reflow soldering unit (programmable hotplate) and position control unit (programmable position controller and fixture).

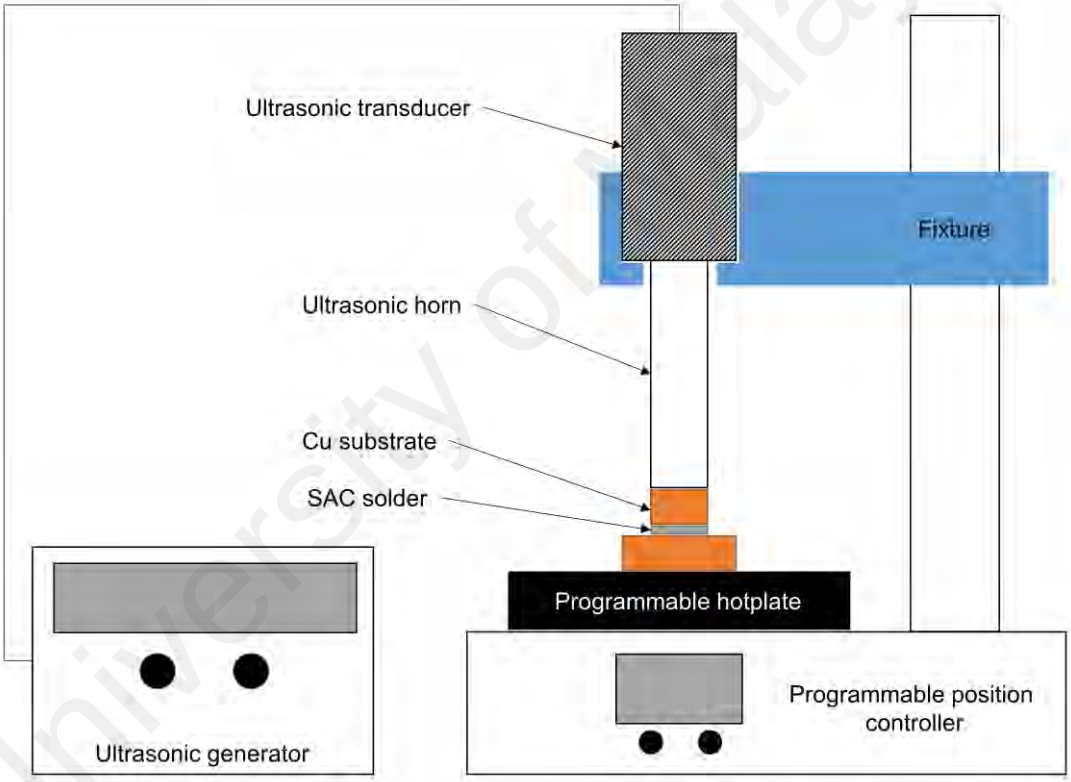

Figure 3.1: Schematic diagram of ultrasonic assisted reflow soldering system

3.2 Experimental research design

The experimental research design of this dissertation is depicted in Figure 3.2.

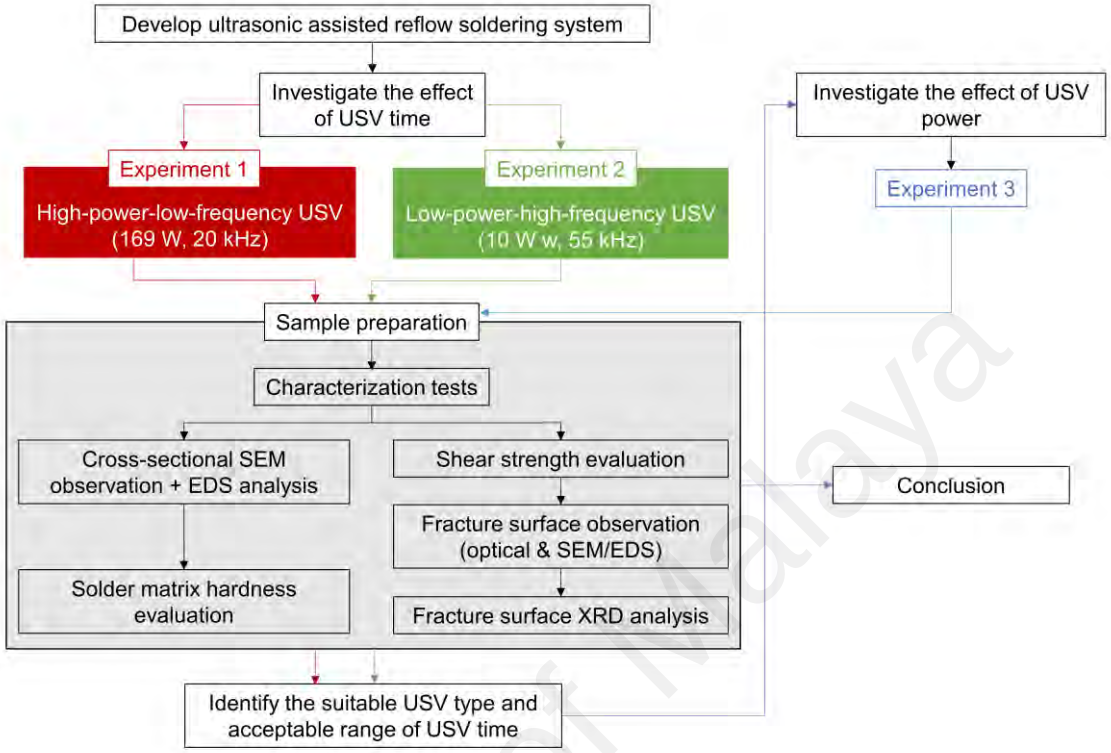

Figure 3.2: Experimental research design flowchart

3.3 Safety precaution

Before conducting the above mentioned experiments, there are several safety precaution to be taken as follows:

1) Put on an earmuff or a pair of earplugs to protect the eardrums from any ultrasound or noise generated by the 20 kHz and 55 kHz USV.
2) Wear a pair of gloves to prevent any form of electric shock while in contact with the ultrasonic unit, programmable hotplate and programmable position controller.
3) Avoid direct contact at the tip of ultrasonic horn as it may generate intense heat upon contact or may cause electric shock to the contacting person.

CHAPTER 4: EFECT OF USV TIME ON THE LEAD FREE SOLDER JOINTS SOLDERED BY HIGH-POWER-LOW-FREQUENCY ULTRASONIC ASSISTED REFLOW SOLDERING

4.1 Introduction and literature review

The research in this chapter has been published in *Journal of Materials Processing Technology, Volume 238, 2016, Pages 8-14*, written by Ai Ting Tan, Ai Wen Tan and Farazila Yusof. The dissertation author is the first author of the publication.

As reviewed in Chapter 2, ultrasonic assisted reflow soldering technique by applying 20-60 kHz USV on lead free soldering assembly during the cooling stage of a reflow soldering process was developed by Kago et al. (2004), Chinnam et al. (2011), Hongjun Ji et al. (2014) and Ji et al. (2016). The solidifying soldering assembly was exposed to ambient atmosphere in common during the application of USV. However, there is a vast difference between these studies, in terms of USV power and time. It is noticed the optimal results were obtained when using either high-power-low-frequency or low-power-high-frequency USV. For example, Hongjun Ji et al. (2014) reported that the optimal ultrasonic power for 28 kHz USV was 133 W. In the work of Chinnam et al. (2011), 40 kHz USV with optimal ultrasonic power of 23 W produced the most satisfying Cu/SAC solder joints. Furthermore, none of these studies reported the effect of USV time and the USV time used in this studies was either uninformed or rather long (up to 240 s). Based on the study of Nagaoka, Morisada, Fukusumi, and Takemoto (2009), aluminum substrates were ultrasonically soldered by Sn-Zn solder under the solder liquidus temperature. The authors observed that the USV time had significant effect on the tensile strength of the joints and the optimal USV time obtained was 4 s.

Therefore, in this chapter, we have established a modified ultrasonic assisted reflow soldering experimental setup, by integrating an ultrasonic system that generates

high-power-low-frequency USV with a digital ceramic hot-plate that can perform reflow soldering according to the soldering profile recommended by IPC/JEDEC joint industry standard (J-STD-020D-01A). Cu substrate is chosen in this study due to its common application as a metallization element in the electronic packages, whereas Sn-3.0Ag-0.5Cu (SAC305) solder is chosen for its conventional application in the electronic packaging industry. The application of USV on the soldering assembly is executed during the reflow stage of the soldering process, instead of cooling stage. The study in this chapter is focused on the effect of USV time on the microstructural and mechanical properties in terms of the shear strength and hardness of the Cu/SAC305/Cu solder joints.

4.2 Methodology

4.2.1 Sample preparation

Cu plates (99% purity) with the dimension of 20 mm x 20 mm x 3 mm (bottom plate) and 15 mm x 15 mm x 3 mm (top plate) were used as substrates in the experiment. They were first grinded using silicon carbide sandpaper with grit size of 30 μm, 15 μm, 10 μm and 5 μm, followed by polishing using 1 μm diamond suspension and fine polishing using 0.05 μm colloidal silica suspension. Next, they were ultrasonically cleaned with acetone for 6 minutes and dried in hot air. The Sn-3.0Ag-0.5Cu (SAC305) solder paste (LFM-48W TM-HP, ALMIT SRC) was then deposited in between the substrates through a mask having an opening of 10 mm x 10 mm and a thickness of 0.42 mm (equivalent to deposited solder mass of 0.27 g) prior to soldering. The layout of the test sample is illustrated in Figure 4.1(a).

4.2.2 Soldering procedures

An ultrasonic assisted reflow soldering system was assembled with a digital ceramic hot plate (CHP-170DN, AS-ONE) and a customized USV output unit. The USV output unit

consisted of an ultrasonic generator and a transducer with horn. The vertical USV generated at the tip of the horn was 20 kHz in frequency and 169 W in power (equivalent to 30 μm in amplitude). The schematic diagram of the soldering arrangement is shown in Figure 4.1(a). The test sample was heated on the hot plate under ambient atmosphere, following the heating profile as shown in Figure 4.1(b). Ultrasonic horn was loaded on the top Cu plate when the temperature reached 260 ˚C, at a pressure of 125 kPa, and vibrated for 1, 2, 3, 4, and 6 s. The sample was then air-cooled to room temperature. Non-ultrasonic-treated sample was fabricated to serve as control sample.

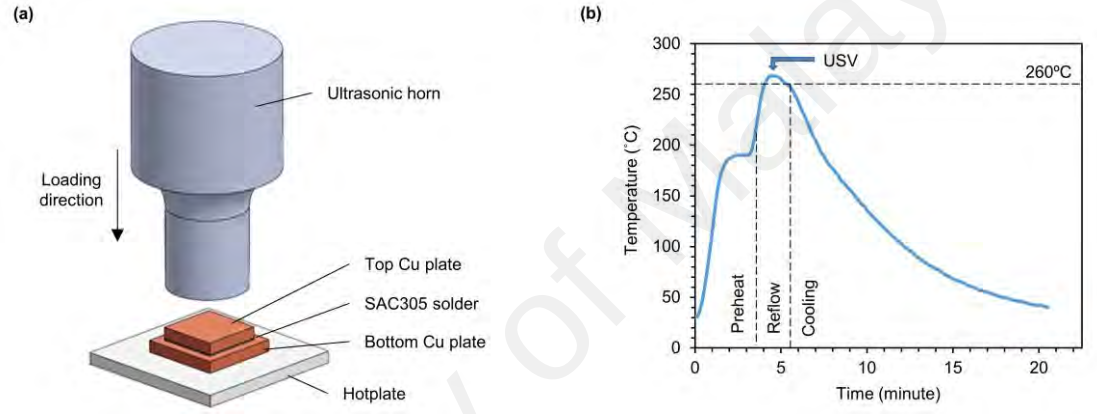

Figure 4.1: (a) Schematic diagram of ultrasonic assisted reflow soldering setup with soldering sample and (b) reflow soldering profile

4.2.3 Cross-sectional observation

The soldered samples were cross-sectioned at the center and then mounted in epoxy. The surface of the cross-sectioned samples was grinded and polished using the same procedures as mentioned in section 3.2.1. All the samples were etched in the solution of 10 vol. % of hydrochloric acid (HCl) + 90 vol. % of methanol (CH_3OH) for 15 s to reveal their microstructure. The microstructure and elemental composition of the samples were characterized by scanning electron microscope (SEM, Phenom ProX) equipped with energy-dispersive x-ray spectroscopy (EDS). The total area of interfacial IMC layer and its length of coverage were measured using an image analysis software (Image J, NIH

software). As illustrated in Figure 4.2, the IMC layer thickness was calculated by dividing the total area of the interfacial IMC layer to its length of coverage, measured from a SEM micrograph (Liashenko, Lay, & Hodaj, 2016). The average IMC layer thickness was obtained from the SEM images taken at ten different spots.

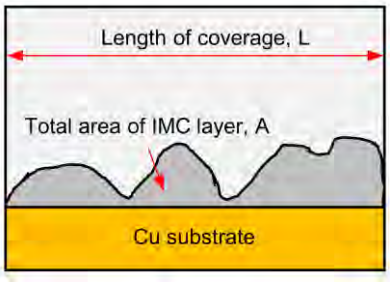

Figure 4.2: Calculation method of interfacial IMC layer thickness

4.2.4 Vickers hardness test

A Vicker microhardness tester (HMV 2T E, SHIMADZU) with pyramidal diamond indenter was used to evaluate the hardness of solder matrix in each sample. Indentation was performed under load control at a peak load of 98.07 mN and held for 10 s at each indent spot. A minimum of 25 indentations were performed randomly on each sample to obtain the average hardness value.

4.2.5 Shear test

Compressive shear test was conducted at room temperature, using a universal testing machine (Instron 3369). The top Cu plate of each sample was clamped to the shear test fixture and the bottom Cu plate was shear punched with a shear strain rate of 1.0 mm/min. The average strength for each parameter was taken from 3 different samples to ensure the validity of data. After shear testing, the failure mode of the samples was investigated in terms of the fractured surface microstructure and elemental compositions using SEM, EDS, and X-ray diffractometer (XRD, PANalytical Empyrean) fitted with CuKα radiation in the 2θ range of 20-80^{o}, respectively.

4.3 Results and discussion

4.3.1 Solder matrix microstructure of Cu/SAC305/Cu joints

Figure 4.3 shows the cross-sectional SEM micrographs of Cu/SAC305/Cu solder joints treated with high-power-low-frequency USV for various time duration. In common, the solder matrix of every sample was constituted by β-Sn and eutectic phases, in which the eutectic phase was present at the boundary region in between the β-Sn phases. In the control sample (Figure 4.3(a)), the β-Sn phase was in a large grain-like structure, while the eutectic phase was in a structure of β-Sn matrix embedded with rod-like or plate-like Ag_3Sn phase and whisker-like Cu_6Sn_5 phase. Refinement on the solder matrix microstructure was observed in every ultrasonic-treated sample. The Ag_3Sn and Cu_6Sn_5 phases embedded in the eutectic phase became particle-like structure after the ultrasonic treatment. The grain-like β-Sn phase was significantly smaller and more uniform in size as compared to the control sample. The size of the grain-like β-Sn phase varied with increasing USV time, but seemingly larger in size after treated with USV for more than 1 s.

The results obtained indicate that microstructural refinement of the Cu/SAC305/Cu solder matrix was achieved after the treatment of high-power-low-frequency USV for as short as 1 s. This may be attributed to the heterogeneous nucleation of solid crystals induced by USV in the molten SAC305 solder during the reflow soldering. The presence of USV in the molten SAC305 solder would induce pressure fluctuation and consequently, generate microbubbles and acoustic streaming in the liquid medium. Formation, growth and collapse of these microbubbles could cause the molten solder to undergo changes from undercooling to superheating frequently, according to T. Leong, Ashokkumar, and Sandra (2011). As reported by H. Ji, Q. Wang, M. Li, and C. Wang (2014) and H.-T. Lee and Huang (2016), rapid undercooling and superheating would promote the nucleation of β-Sn, Ag_3Sn and Cu_6Sn_5 crystals in the molten SAC305

solder. The distribution of these solid crystals in the molten solder could be homogenized by the USV-induced acoustic streaming. Since the USV setup in the this study produces USV with a high amplitude of 30 μm, the USV is more intense and thereby, promoted the intensity of acoustic streaming and the crystallization rate of β-Sn, Ag_3Sn and Cu_6Sn_5 crystals, as mentioned by Luque de Castro and Priego-Capote (2007). A uniform acoustic streaming flow across the solder joint may be achieved as the top Cu substrate was completely in-contact with the ultrasonic horn in our studies. Therefore, the solidified solder joints exhibited a refined solder matrix microstructure, even treated with USV for duration as short as 1 s.

By comparing the solder matrix microstructure of the ultrasonic-treated samples, the effect of USV time on the morphological change of β-Sn phase is more remarkable than those of eutectic phase. As the SAC305 is mainly composed of Sn element, we speculate that the amount of nucleated β-Sn crystals increased more rapidly with USV time, if compared to the Ag_3Sn and Cu_6Sn_5 crystals. With the aid of acoustic streaming, these β-Sn crystals aggregated and formed larger β-Sn phase in the samples treated with longer USV time. Other than the aggregation effect, acoustic streaming can also induce segregation of phases that are present in the molten SAC305 solder. Therefore, the combination of aggregation and segregation effects may attribute to the size variation of β-Sn phase, as observed in the samples treated with 1 to 6 s of USV (as shown in Figure 4.3(b)-(f)).

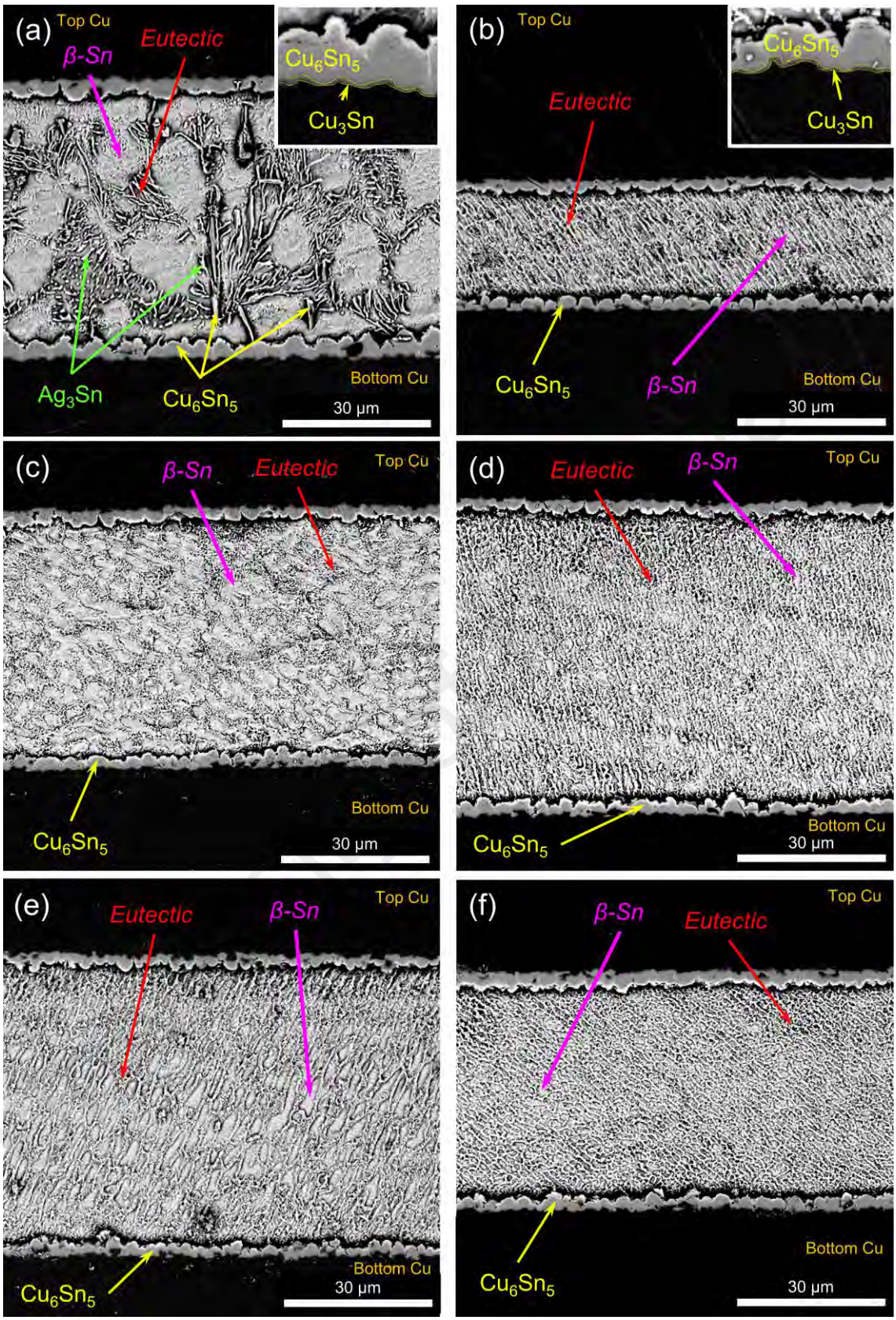

Figure 4.3: Cross-sectional SEM micrograph of Cu/SAC305/Cu solder joint treated with USV time of (a) 0 s, (b) 1 s, (c) 2 s, (d) 3 s, (e) 4 s, and (f) 6 s

4.3.2 Interfacial microstructure at Cu/SAC305/Cu joints

At the Cu/SAC305 interfaces of every sample, formation of Cu_3Sn and Cu_6Sn_5 IMC layers were observed, in which the Cu_6Sn_5 layer was formed adjacent to the solder matrix while the Cu_3Sn layer was formed in between the Cu substrate and the Cu_6Sn_5 layer. As depicted in the insets of Figure 4.3(a) and 4.3(b), the Cu_3Sn layer in every sample was very thin and seemingly planar in shape. Meanwhile, the Cu_6Sn_5 layer consisted of many scallop-shaped Cu_6Sn_5 grains and the size of these Cu_6Sn_5 grains was observed to be larger in the control sample compared to the other counterparts. To further identify the effect of USV time on the interfacial IMC formation quantitatively, the thickness of both interfacial Cu_3Sn and Cu_6Sn_5 layers at the top and bottom Cu/SAC305 interfaces was measured and the results were plotted in Figure 4.4. The interfacial IMC layers of the ultrasonic-treated samples were thinner compared to those of the control sample. When the USV time increased from 1 to 6 s, the IMC layers thickness varied with USV time, but was generally increased after 1 s of USV time. The difference in thickness between the top and bottom interfacial IMC layers was also found to increase with USV time after 1 s.

The general reduction of interfacial IMC layer thickness after the ultrasonic treatment may be contributed by the size reduction of Cu_6Sn_5 grains that formed at the top and bottom Cu/SAC305 interfaces. As reported in the studies of Gong et al. (2008) and Gong et al. (2009), small and separated Cu_6Sn_5 grains started to form at the Cu/SAC305 interfaces once the solder reached its liquidus temperature. The channels between the Cu_6Sn_5 grains served as easy path for the dissolution of Cu atom from the Cu substrates into the molten SAC305 solder. These dissolved Cu atoms accelerated the formation of new interfacial Cu_6Sn_5 grains and the coarsening of existing Cu_6Sn_5 grains before the solder joint solidified completely. With the presence of USV in the molten solder, the growth of the interfacial Cu_6Sn_5 grains was suppressed as the dissolved Cu

atoms were dispersed evenly into the molten solder and nucleated as Cu_6Sn_5 crystals that might contribute to the eutectic phase formation. The existing Sn atoms might nucleate into β-Sn crystals, instead of forming the interfacial Cu_6Sn_5 grains. Therefore, the interfacial Cu_6Sn_5 grains were smaller in size after the ultrasonic treatment. This observation is in good agreement with the morphological change of the interfacial Cu_6Sn_5 layers as observed in Figure 4.3.

The variation of interfacial IMC layers thickness in the samples treated with USV time from 1 to 6 s may be related to the degree of saturation in the molten SAC305 solder before solidification. As the dissolved Cu atoms near the Cu/SAC305 interfaces was transported away by the acoustic streaming, dissolution of Cu atoms from the Cu substrates continued due to the concentration gradient at the interfaces. With the continual occurrence of acoustic cavitation, the amount of nucleated β-Sn, Ag_3Sn and Cu_6Sn_5 crystals increased with USV time. These crystals may aggregate and segregate to form β-Sn, Ag_3Sn and Cu_6Sn_5 solid particles with the aid of acoustic streaming. Therefore, the increased amount of Cu_6Sn_5 solid particles may contribute to the increase of interfacial Cu_6Sn_5 layers thickness in the samples treated with longer USV time. Concurrently, the increasing amount of solid particles formed at increasing USV time may interrupt the flow of acoustic streaming in the molten SAC305 solder. In other words, the homogenization effect diminished with increasing USV time and resulted in greater discrepancy between the top and bottom interfacial Cu_6Sn_5 layer thickness.

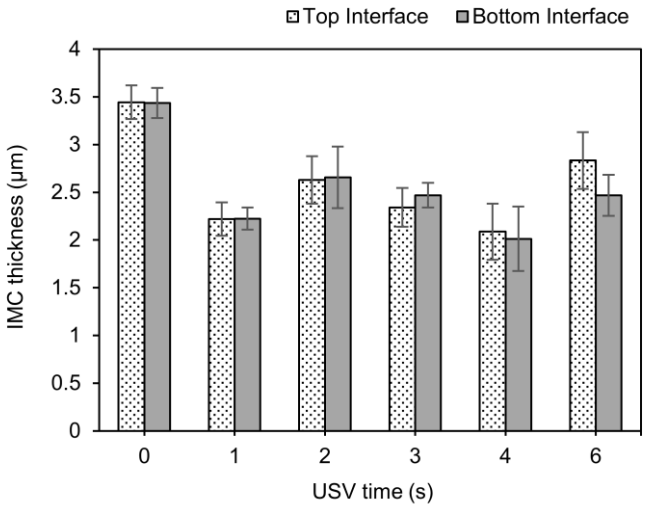

Figure 4.4: Interfacial Cu_6Sn_5 + Cu_3Sn IMC layers thickness with respect to USV time

4.3.3 Hardness of Cu/SAC305/Cu joints

The measured Vickers hardness values at the solder matrix region of every Cu/SAC305/Cu sample are plotted in Figure 4.5. The plot shows a marked increase in the hardness of the ultrasonic-treated samples compared to the control sample. From the ultrasonic-treated samples, the obtained solder matrix hardness varied with time but exhibited an increasing trend with USV time.

The improvement on the solder matrix hardness after the ultrasonic treatment is in accordance with the microstructural refinement on the solder matrix as observed in Figure 4.3. The eutectic phase has direct influence on the solder matrix hardness due to the dispersion or phase-boundary strengthening, according to Mahmudi and Alibabaie (2013) and M. N. Wang, Wang, Feng, and Ke (2012). As the Ag_3Sn and Cu_6Sn_5 phases embedded in the eutectic phase were refined after the ultrasonic treatment, the eutectic phase obtained higher resistance against the indentation force and thereby, hindered the dislocation along the eutectic phase region.

The variation of solder matrix hardness of the ultrasonic-treated samples with time may be associated to the size variation of the β-Sn phase, as observed in Figure 4.3(b)-(f). X. Deng, Chawla, Chawla, and Koopman (2004) reported that the β-Sn phase is the

softest constituent in the SAC305 solder. Therefore, we speculate that the larger β-Sn phase as observed from the ultrasonic-treated samples at 2 s (Figure 4.3(c)) and 4 s (Figure 4.3(e)) is accounted for lower solder matrix hardness as shown in Figure 4.5.

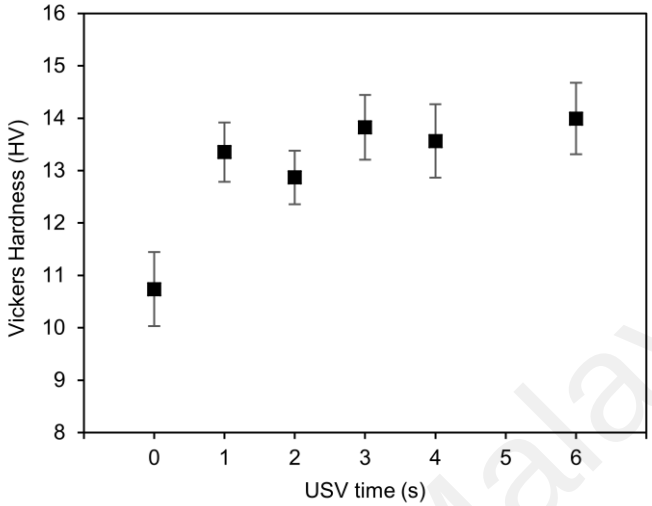

Figure 4.5: Vickers hardness of the Cu/SAC305/Cu solder matrix with respect to USV time

4.3.4 Mechanical strength and fracture behavior of Cu/SAC305/Cu joints

Figure 4.6 shows the yield and shear strength of the Cu/SAC305/Cu samples treated at varied USV time. Significant enhancement on the yield and shear strength of the solder joints was observed after the ultrasonic treatment. However, the shear strength of the ultrasonic-treated samples varied insignificantly with USV time, but the yield strength decreased gradually with increasing USV time.

To further confirm the influence of USV time on the mechanical strength of the Cu/SAC305/Cu solder joints, the fractured surface at the top Cu substrate after shear testing was observed under SEM and the composition of the fractured surface was identified by XRD. As seen in Figure 4.7(a)-(c) and 4.7(g)-(i), macrovoids were found in every sample but the size of macrovoids was apparently smaller after the ultrasonic treatment. Furthermore, all the samples behaved in a ductile manner under shear stress as

parabolic dimples were found on the topography of the fractured surfaces, as shown in Figure 4.7(d)-(f) and 4.7(j)-(l). Greater number of dimples were observed in the samples treated with USV time of 1 to 4 s. The topography of the dimples surface in the sample treated with 6 s of USV time was seemingly the roughest among all the samples.

Figure 4.8 shows the XRD pattern of the fractured surface at the top Cu substrate of every sample. As compared to the control sample, higher intensity of β-Sn (peaks located at 2θ angles of 32°, 62.5° and 79.5°), Cu (peaks at 50.4° and 74.1°), Ag_3Sn (peaks at 37.6° and 39.6°) and Cu_6Sn_5 (peaks at 43.3° and 74.6°) phases were found in the ultrasonic-treated samples. However, the intensity of these phases does not vary significantly with increasing USV time.

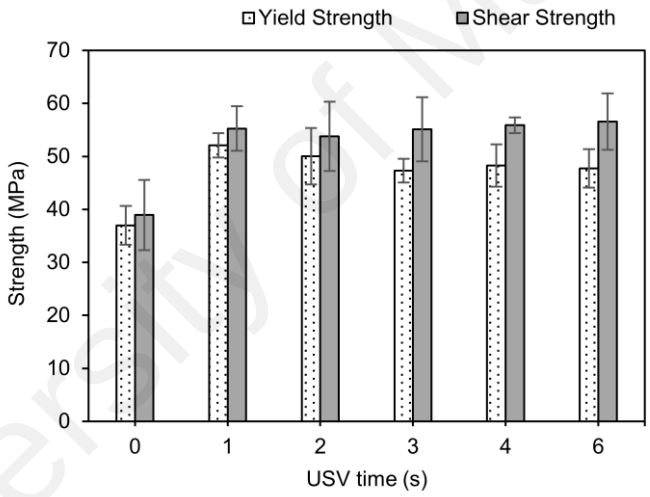

Figure 4.6: Shear strength of the Cu/SAC305/Cu solder joints with respect to USV time

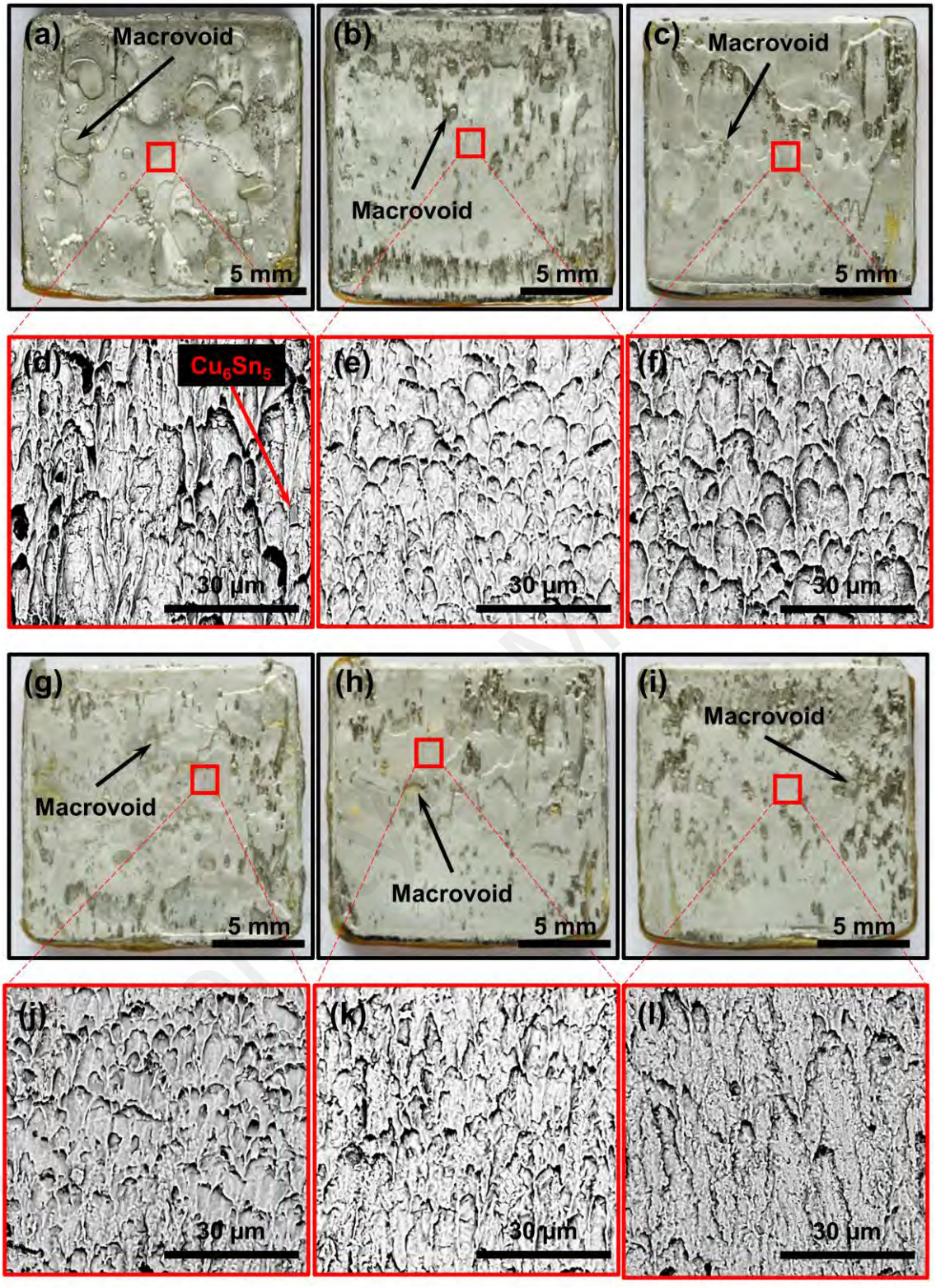

Figure 4.7: Shear fracture surface microstructure of the Cu/SAC305/Cu solder joint treated with USV time of (a, d) 0 s, (b, e) 1 s, (c, f) 2 s, (g, j) 3 s, (h, k) 4 s, and (i, l) 6 s

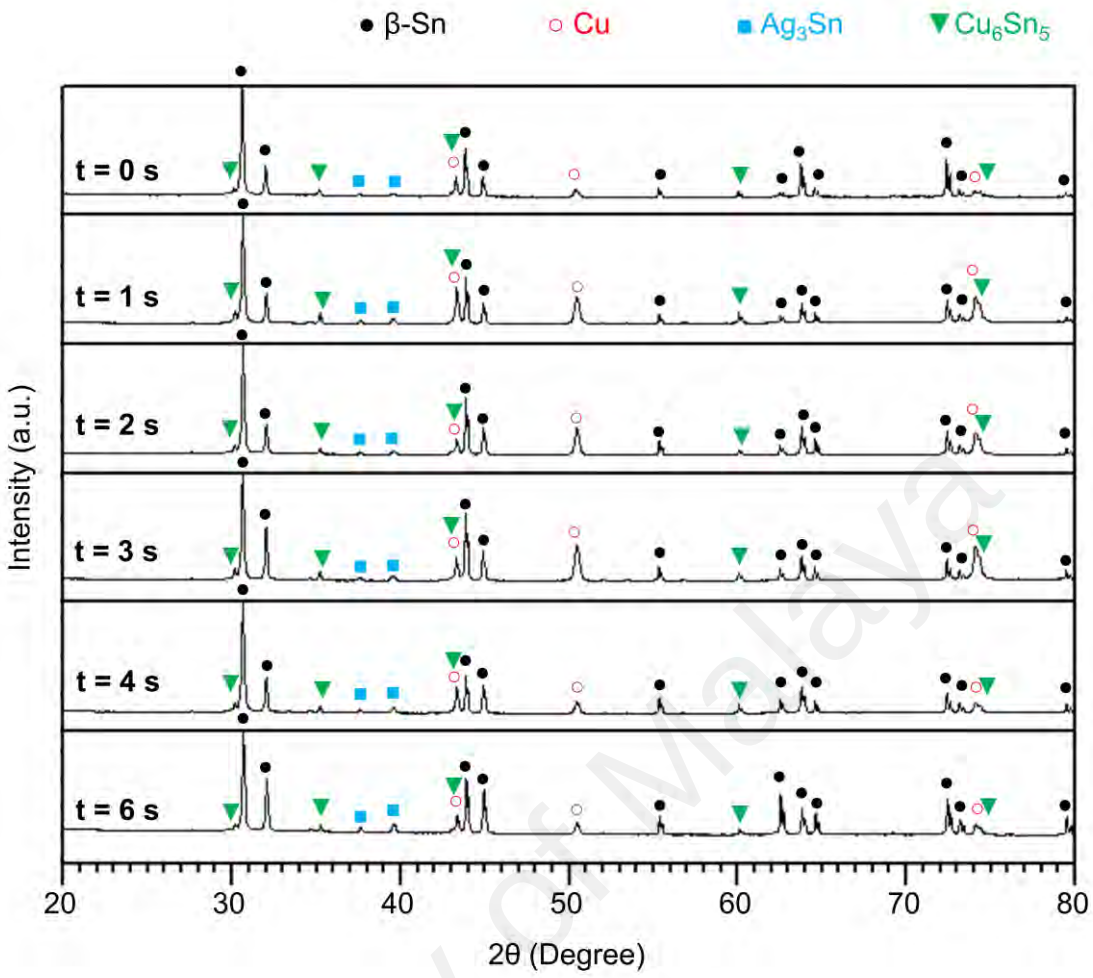

Figure 4.8: XRD analysis from the fractured surface of Cu/SAC305/Cu solder joint treated with various USV time

4.4 Conclusion

Ultrasonic assisted reflow soldering of Cu/SAC305/Cu samples was conducted by applying high-power-low-frequency USV on the sample during the reflow stage for 1 to 6 s. The influence of USV time on the microstructure and shear strength of the solder joints can be summarized as follows:

a) All the ultrasonic-treated Cu/SAC305/Cu samples exhibited finer solder matrix microstructure, thinner interfacial Cu_6Sn_5 IMC layer, improved solder matrix hardness and better mechanical strength as compared to the control sample.

b) By comparing the morphology of the phases present in the solder matrix, the effect of USV time from 1 to 6 s was more significant on the β-Sn phase than the eutectic phase.

c) The interfacial Cu_6Sn_5 IMC layer at the top and bottom Cu/SAC305 interfaces was generally thicker at longer USV time. The difference of IMC thickness between these two interfaces was found to increase with USV time.

d) The obtained solder matrix hardness exhibited an increasing trend with USV time, indicating that the Cu/SAC305/Cu sample is less ductile when treated with USV for longer duration.

e) The shear strength of the ultrasonic-treated samples was not affected by the USV time. However, the yield strength of these samples exhibited a decreasing trend with increasing USV time from 1 to 6 s.

CHAPTER 5: EFECT OF USV TIME ON THE LEAD FREE SOLDER JOINTS SOLDERED BY LOW-POWER-HIGH-FREQUENCY ULTRASONIC ASSISTED REFLOW SOLDERING

5.1 Introduction

The research in this chapter has been published in *Ultrasonics Sonochemistry, Volume 34, 2017, Pages 616-625*, written by Ai Ting Tan, Ai Wen Tan and Farazila Yusof. The dissertation author is the first author of the publication.

The results presented in the previous chapter suggest that the proposed ultrasonic assisted reflow soldering technique is a viable approach to improve the Cu/SAC305/Cu solder joint in terms of microstructure and mechanical properties. To realize the full potential of this technique, the established ultrasonic assisted reflow soldering experimental setup has been modified in the present study, by using an ultrasonic system that generates low-power-high-frequency USV. The effect of USV time on the properties of Cu/SAC305/Cu solder joints is investigated in this chapter.

5.2 Methodology

5.2.1 Sample preparation

Cu plates (99% purity) with the dimension of 15 mm x 15 mm x 3 mm (bottom plate) and 2 mm x 8 mm in diameter (top plate) were used as the substrates in this study. Prior to soldering, the faying surface of the substrate was ground, polished and cleaned using standard metallographic techniques. SAC305 solder paste (ALMIT SRC, LFM-series) was placed in between the substrates through a mask with an opening diameter of 6 mm and a thickness of 0.4 mm (equivalent to 0.1 g of solder paste).

5.2.2 Soldering system

An ultrasonic assisted reflow soldering system was assembled with an USV output unit (HC-DLT-5580, Hangzhou Create Ultrasonic Technology Co., Ltd, Hangzhou, China) and a digital ceramic hotplate (CHP-170DN, AS-ONE, Japan). The USV output unit consisted of an ultrasonic generator and a transducer with horn. The vertical USV generated at the tip of the horn has a frequency of 55 ± 1 kHz and a power of 10 W (equivalent to 2 μm in amplitude). The ceramic hotplate was equipped with a temperature control system (PID control by Type-K thermocouple) to measure the actual temperature throughout the soldering process. All the instruments were exposed to the ambient atmosphere.

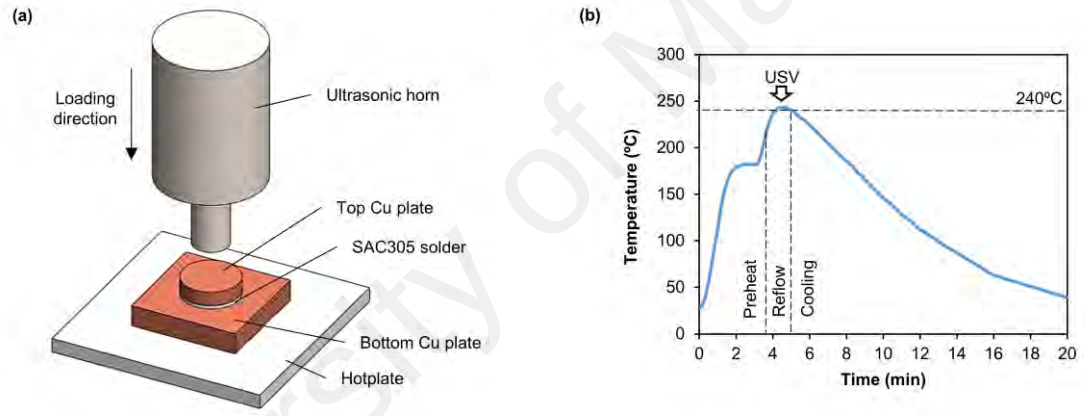

Figure 5.1: (a) Schematic diagram of the soldering sample and ultrasonic assisted soldering system and (b) reflow soldering profile

5.2.3 Soldering procedure

The ultrasonic assisted reflow soldering system is schematically illustrated in Figure 5.1(a). The sample was placed on the hotplate and heated under ambient atmosphere, following the reflow soldering profile as shown in Figure 5.1(b). When the temperature reached above 240 ˚C (during reflow stage), the ultrasonic horn was loaded on the top Cu plate to apply vertical 10 W USV with different vibration time of 1.5, 3, 4.5 and 6 s. The hotplate was turned off immediately after the reflow stage as indicated in Figure 5.1(b)

and the sample was then cooled to room temperature at a rate of 0.3 ˚C/s. Non-ultrasonic-treated sample was fabricated to serve as the control sample.

5.2.4 Characterization methods

The soldered samples were cross-sectioned at the center and then ground and polished using the standard metallographic techniques. All the samples were etched in the solution of 10 vol. % of HCl + 90 vol. % of CH_3OH for 15 s to reveal their microstructure. The microstructure and elemental composition of the samples were characterized by a scanning electron microscope (SEM, Phenom ProX, Netherlands) equipped with energy-dispersive x-ray spectroscopy (EDS). An image analysis software (Image J, NIH software) was used to measure the sectional area of the β-Sn phase and the interfacial IMC layer thickness. The average sectional area of the β-Sn phase was taken from at least three different spots in every sample. The interfacial IMC layer thickness was measured by dividing the total area of IMC layer by its total length. The average interfacial IMC layer thickness was taken from at least five SEM images at different spots in every sample.

The hardness of the solder matrix region in each sample was evaluated by a Vicker microhardness tester (HMV 2T E, SHIMADZU) with pyramidal diamond indenter. Indentation was performed under load control at a peak load of 98.07 mN and held for 10 s at each indent spot. A minimum of 20 indentations were performed randomly on each sample to obtain the average hardness value.

Shear tests were conducted using a universal testing machine (Instron 3369) by clamping the bottom Cu plate to the shear test fixture. The top Cu plate was shear punched with a shear strain rate of 0.5 mm/min at room temperature. The average shear strength was taken from three different samples for each joining parameter. After the shear test, the microstructure and elemental composition of the shear fractured surface were

observed by the SEM equipped with EDS and analyzed by X-ray diffractometer (XRD, PANalytical Empyrean, Netherlands) fitted with CuKα radiation in the 2θ range of 20-80˚.

5.3 Results and discussion

5.3.1 Microstructure at the solder matrix of Cu/SAC305/Cu solder joint

Figure 5.2 shows the cross-sectional SEM micrographs of the solder matrix of Cu/SAC305/Cu solder joints treated with 10 W USV at various USV times. Commonly, the solder matrix of every sample is constituted of primary β-Sn phase and eutectic phase where the eutectic phase was present at the boundary region between the primary β-Sn phases. In the control sample (Figure 5.2(a)), the primary β-Sn phase was in a dendritic structure and adhered with nearly circular branches. These β-Sn dendrites were aligned in the oblique direction to the Cu substrates. Viewing under higher magnification, the eutectic phase (Figure 5.2(a)-(i)) was in a structure of β-Sn matrix embedded with particle or rod-like Ag-rich and Cu-rich intermetallic phases, as confirmed by the EDS analysis as shown in Table 4.1.

Microstructural refinement on the solder matrix was observed when the sample was treated with 10 W USV for 1.5 s (Figure 5.2(b)). The primary β-Sn phase changed to small grain-like structure. Meanwhile, the eutectic phase seemed to have a network-like structure. Both the primary β-Sn and eutectic phase were distributed homogeneously within the solder matrix. However, the primary β-Sn phase appeared as coarsened dendrite when the USV time was increased to 3 s (Figure 5.2(c)). The eutectic phase seemed to coarsen as well and Cu_6Sn_5 whisker was found embedded in the eutectic region. The microstructure of the solder matrix treated with 4.5 s of USV (Figure 5.2(d)) was similar to those at 3 s, except for the allignment of primary β-Sn dendrites which was now alligned in the direction of almost perpendicular to the Cu substrates. Particle-like Ag_3Sn,

rod-like Cu_6Sn_5 and Cu_6Sn_5 whisker were found in the eutectic region. When the USV time was prolonged to 6 s (Figure 5.2(e)), the solder joint thickness was remarkably reduced as compared to the other counterparts. The morphology of the eutectic phase has changed into the structure of β-Sn matrix embedded with mostly plate-like Ag_3Sn phase. The Ag_3Sn plates were alligned in the oblique direction or almost parallel to the Cu substrates. Moreover, some of the Ag_3Sn plates were connected to the opposite interfacial IMC layers.

The average sectional area of the primary β-Sn phase in every sample was measured and the results are plotted in Figure 5.3. Based on the figure, the average size of the primary β-Sn phase in the sample treated with 1.5 s of USV decreased by 72.05 % compared to the control sample. However, the average size of the primary β-Sn phase increased drastically in the samples treated from 3 to 6 s. A great variation was observed in every sample, except the sample treated with 1.5 s of USV. This is attributed to the morphological change of the primary β-Sn phase after treating with USV for various time as observed in Figure 5.2.

The results above suggest that the application of 10 W USV during the reflow stage altered the morphology of the solder matrix, from refine to coarsen with increasing USV time from 1.5 to 6 s. This may be attributed to the acoustic streaming and cavitation associated with the propagation of USV in the molten SAC305 solder. Under normal reflow soldering condition (refer to the control sample), the Cu_6Sn_5 phase nucleates first in the solder matrix during the reflow stage due to the high soldering temperature that accelerated the dissolution of Cu atoms from the Cu substrate into the molten SAC305 solder, leading to the formation of interfacial Cu_6Sn_5 layer and eutectic phase in the subsequent cooling stage. When the molten solder undergoes large undercooling, the β-Sn phase nucleates and grows into dendritic form. When the molten solder temperature drops to the eutectic temperature (approximately 217 °C), the remaining molten solder

solidifies and forms the eutectic phase. As observed from Figure 5.2(a), the morphology and distribution of the β-Sn and eutectic phases were less homogeneous in the solder joint formed by normal reflow soldering.

With the application of USV during the reflow stage, pressure fluctuation is generated in the molten solder and induced acoustic streaming that can effectively homogenize the mass and heat transfer within the molten solder. At the same time, acoustic cavitation in the form of tiny bubbles is generated in the molten solder, either from the pre-existing bubbles in the molten solder or formed at the solid/liquid interface (in this case, Cu_6Sn_5/molten solder interface) (H. J. Ji, Q. Wang, M. Y. Li, & C. Q. Wang, 2014). These cavitation bubbles expand in size during the rarefaction phase of the USV wave and compress during the compression phase. The bubble expansion causes the surrounding molten solder to be undercooled while the bubble compression causes the surrounding molten solder to be superheated. Undercooling of the molten solder promotes the nucleation of β-Sn phase, while superheating promotes the nucleation of Ag_3Sn and Cu_6Sn_5 phases. The bubbles oscillation can occur with high frequency and increases the amount of nuclei in the molten solder during the reflow stage. Eventually, the cavitation bubbles grow in size with USV time and may collapse (termed as transient cavitation) when they reach their resonance size or continue to oscillate without collapsing (termed as stable cavitation) (Thomas Leong, Ashokkumar, & Kentish). Transient cavitation would release tremendous amount of heat that further superheat the molten solder and shock waves that facilitate the mass transfer or streaming effect. The oscillation of stable cavitation can contribute to the micro-streaming effect.

Based on the observation in Figure 5.2, it can be deduced that the acoustic streaming and cavitation took place concurrently in the molten solder during the reflow stage. The effects induced by acoustic streaming and cavitation were emphasized with increasing USV time. Increasing USV time increased the cavitation activity and more β-

Sn, Ag_3Sn and Cu_6Sn_5 phases nucleated in the molten solder during the reflow stage. Meanwhile, acoustic streaming lasted for longer duration and led to aggregation and segregation effects, instead of a solely homogenization effect (Luque de Castro & Priego-Capote, 2007). Aggregation caused the nucleated β-Sn, Ag_3Sn and Cu_6Sn_5 phases to coarsen, and morph into the β-Sn dendrites, plate-like Ag_3Sn and Cu_6Sn_5 whiskers whereas segregation caused the eutectic phase to be distinctly separated by the coarsened β-Sn dendrites. Therefore, this may explain the change of solder matrix microstructure in the Cu/SAC305/Cu solder joint from refine to coarsen as observed in our studies.

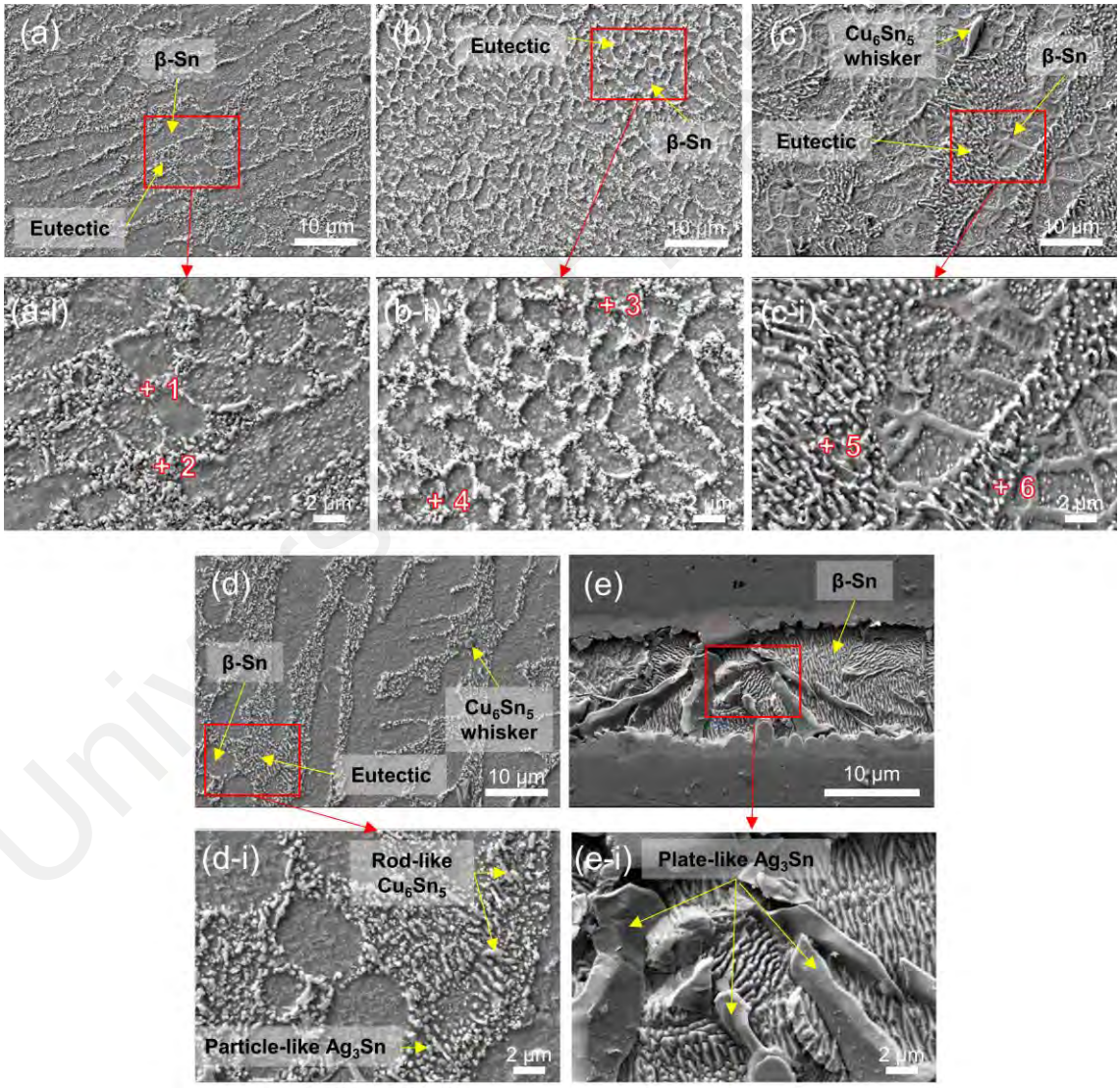

Figure 5.2: SEM cross-sectional images of the solder matrix of Cu/SAC305/Cu solder joints with respect to USV time; (a) Without USV, (b) 1.5 s, (c) 3 s, (d) 4.5 s and (e) 6 s

Table 5.1: EDS results for the analyzed points shown in Figure 5.2

Spot	Element (at%)			Phase
	Sn	Ag	Cu	
1	38.58	25.59	35.83	Eutectic
2	36.86	38.32	24.82	Eutectic
3	47.79	9.2	43.02	Eutectic
4	34.6	46.02	19.38	Eutectic
5	66.41	4.7	28.89	Eutectic
6	52.9	43.68	3.43	Eutectic

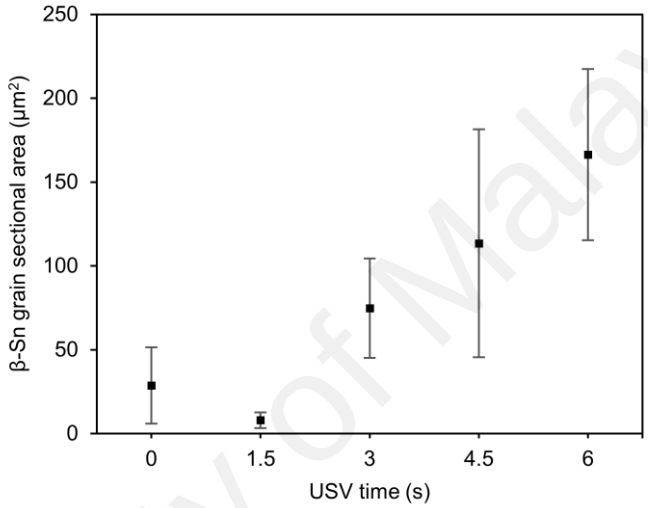

Figure 5.3: Sectional area of the β-Sn phase in the Cu/SAC305/Cu solder joints with respect to USV time

5.3.2 Hardness of the solder matrix of Cu/SAC305/Cu solder joint

Figure 5.4 shows the Vickers hardness of the solder matrix of Cu/SAC305/Cu solder joints treated with 10 W USV at various USV times. The solder matrix hardness increased from 11.465 ± 0.57 HV in the control sample to 12.06 ± 0.66 HV in the sample treated with 1.5 s of USV. However, the solder matrix hardness of the samples treated with 3 s to 6 s was lower than that of the control sample. The sample treated with 6 s of USV was found to have the highest hardness among these samples, which was 11.14 ± 0.52 HV.

The variation of the solder matrix hardness is associated with the evolution of the solder matrix microstructure with USV time. The increase of solder matrix hardness in

the sample treated with 1.5 s of USV is contributed by the homogeneously distributed small grain-like β-Sn phase in the network-like eutectic phase. The decrease of solder matrix hardness in the samples treated with longer USV time is attributed to the coarsening of β-Sn dendrites and the Ag_3Sn and Cu_6Sn_5 phases in the eutectic region. However, the presence of plate-like Ag_3Sn phase in the sample treated with 6 s of USV has slightly improved its solder matrix hardness compared to the samples treated with 3 and 4.5 s of USV time. This is because the plate-like Ag_3Sn phase has higher hardness than the particle-like Ag_3Sn phase in the eutectic region (X. Deng et al., 2004). Similar observation was reported in the work of Lee and Huang (H.-T. Lee & Huang, 2016).

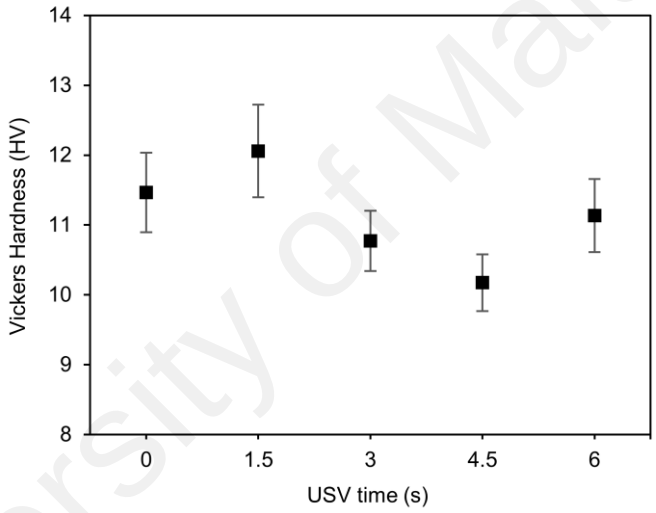

Figure 5.4: Vickers hardness of the Cu/SAC305/Cu solder matrix with respect to USV time

5.3.3 Interfacial microstructure of the Cu/SAC305/Cu solder joint

Cu_6Sn_5 and Cu_3Sn are the two types of IMCs formed at the Cu/SAC305 interface in every sample. As depicted in Figure 5.5(a), the Cu_3Sn IMC layer formed in between the Cu substrates (both the top and bottom) and the Cu_6Sn_5 IMC layer was very thin and planar in shape. On the other hand, the Cu_6Sn_5 IMC layer consisted of many Cu_6Sn_5 grains, which were scallop in shape. In the control sample (Figure 5.5(a)), the top interfacial IMC layers seemed to be discontinuous and had double layers of finer Cu_6Sn_5 scallops in some

regions. In contrast, the bottom interfacial IMC layers were continuous and the Cu_6Sn_5 IMC layer was formed by single layer of Cu_6Sn_5 scallops. Overall, the Cu_6Sn_5 IMC layer on both interfaces was coarse and the size of the interfacial Cu_6Sn_5 scallops was uneven across the layer.

The morphology of both the top and bottom interfacial layers changed notably after treating with 10 W USV. In the sample treated with 1.5 s of USV (Figure 5.5(b)), the top interfacial IMC layers became continuous and the Cu_6Sn_5 scallops formed at this interface were shorter in width but longer in height. Meanwhile, the bottom interfacial IMC layers became discontinuous with double layers of finer Cu_6Sn_5 scallops. The size of the Cu_6Sn_5 scallops was relatively uniform across the layer compared to the control sample. Similar morphology of both the top and bottom interfacial layers was observed in the samples treated with 3 s to 6 s of USV (refer to Figure 5.5(c)-(e)). However, the size of the Cu_6Sn_5 scallops seemed to decrease with increasing USV time. On the other hand, the morphological change of Cu_3Sn IMC layer after the ultrasonic treatment was insignificant as compared to those of Cu_6Sn_5 IMC layer.

The effect of USV time on the interfacial microstructure was further quantified by calculating the total thickness of the interfacial (Cu_6Sn_5 + Cu_3Sn) IMC layers at the top and bottom Cu substrates of each sample, and the results are plotted in Figure 5.6. Both the top and bottom interfacial IMC layer thickness exhibited a decreasing trend with increasing USV time in general, except for the USV time of 1.5 s. The top interfacial IMC layer at this time had comparable thickness with the control sample, but the bottom IMC layer was exceptionally thicker than the other counterparts. By comparing the thickness of the top and bottom interfacial IMC layer, it is noticed that the discrepancy in thickness between these two interfaces reduces only after the samples were treated with 10 W USV for at least 3 s.

Based on the results obtained, it is clear that the refinement on the morphology of interfacial IMC layers (typically the Cu_6Sn_5 layer) in the Cu/SAC305/Cu solder joint can be achieved by the application of 10 W USV during the reflow stage regardless of the USV time. We speculate that acoustic streaming is the main influencing factor on these morphological changes of the interfacial IMC layers. According to the work of Gong et al. (2008), the interfacial Cu_6Sn_5 and Cu_3Sn IMC layers started to form once entering the reflow stage. Without the disturbance of USV, the interfacial Cu_6Sn_5 scallops continued to thicken and coarsen until the solder joint solidified completely (as shown in Figure 5.5(a)). The difference in IMC thickness between the top and bottom interfaces of the control sample and the discontinuous top interfacial IMC layer implied that the temperature distribution and Cu dissolution is not even across the solder joint.

With the application of USV during the reflow stage, the induced acoustic streaming has homogenized the temperature distribution in the molten solder. This is evidenced by the reduction of discrepancy between the top and bottom interfacial IMC layers thickness. Additionally, the dissolved Cu atoms that accumulated near the Cu_6Sn_5/molten solder interface were transported and distributed evenly across the solder joint. This resulted in the formation of thinner interfacial Cu_6Sn_5 IMC layer with uniform scallop morphology, as observed in the ultrasonic-treated samples.

However, in the sample treated with short USV time of 1.5 s during the reflow stage, it is presumed that the hot plate may continue to supply heat from the bottom Cu substrate before entering the subsequent cooling stage. Therefore, the homogenization induced by the USV may have accelerated the dissolution of Cu atoms from the bottom Cu substrate during the post-ultrasonic reflow period, leading to the formation of exceptionally thick bottom interfacial IMC layer with the morphology of double layer of finer Cu_6Sn_5 scallops, as observed in the Figure 5.5(b).

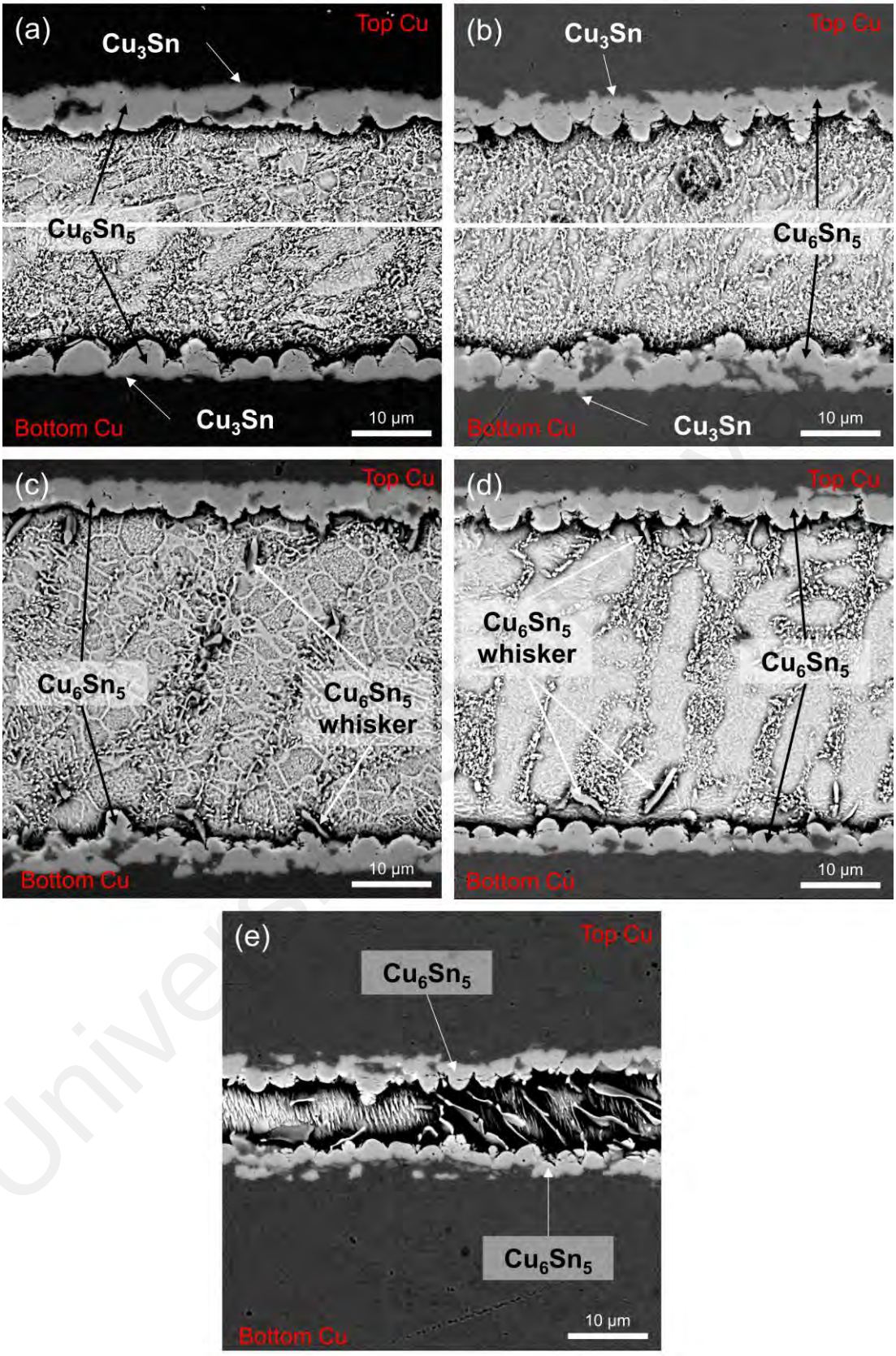

Figure 5.5: SEM cross-sectional images of the interfacial microstructure of Cu/SAC305/Cu solder joints with respect to USV time; (a) Without USV, (b) 1.5 s, (c) 3 s, (d) 4.5 s and (e) 6 s

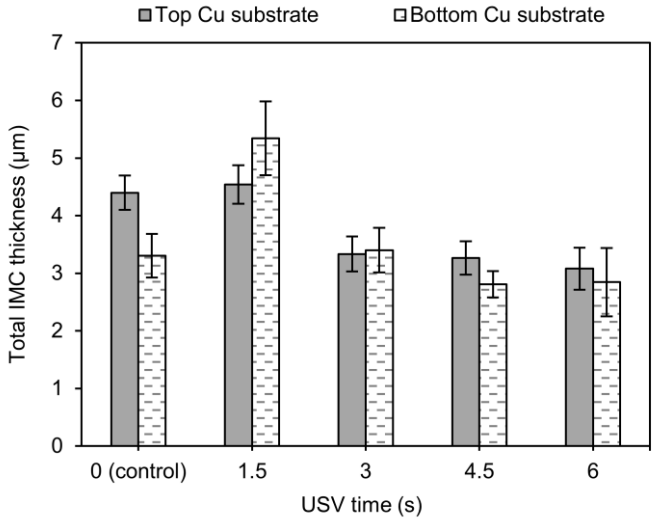

Figure 5.6: Total thickness of interfacial (Cu_6Sn_5 + Cu_3Sn) IMC layers with respect to USV time

5.3.4 Shear strength of Cu/SAC305/Cu solder joint

Figure 5.7 shows the shear strength of the Cu/SAC305/Cu solder joints treated with 10 W USV for different USV times. In general, the ultrasonic-treated samples possessed higher shear strength than the control sample, which had the lowest shear strength of 37.70 ± 3.88 MPa. Among the ultrasonic-treated samples, the samples treated within the range of 1.5 s to 4.5 s of 10 W USV possessed comparable value of shear strength and the highest shear strength of 48.51 ± 4.33 MPa was achieved at 4.5 s. This is equivalent to an increase of 28.67 % of shear strength compared to the control sample. However, the shear strength decreased to 42.88 ± 2.48 MPa after treated with 6 s of USV, which is equivalent to a decrease of 11.61 % of shear strength compared to the USV-treated sample at 4.5 s but an increase of 13.74% compared to the control sample.

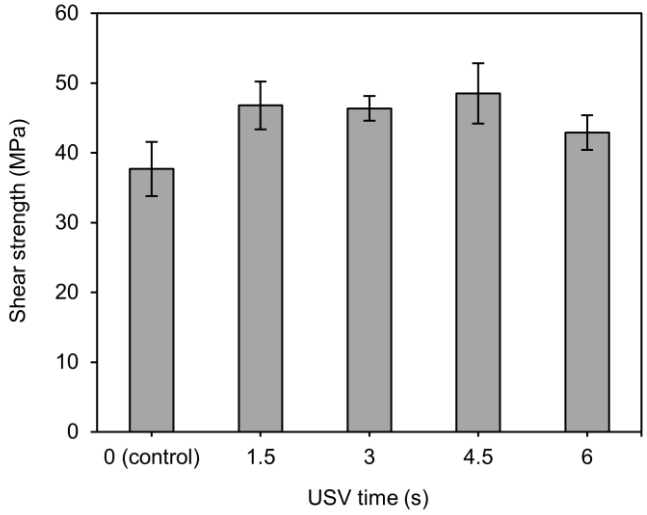

Figure 5.7: Shear strength of Cu/SAC305/Cu solder joints with respect to USV time

5.3.5 Observation of shear-fractured surface

The morphology of the shear-fractured surface on the top Cu substrate was observed by SEM, and the results are presented in Figure 5.8. Macrovoids were found in every sample but the amount and size of the macrovoids were apparently reduced after treated with USV. The macrovoids in the control sample may be formed by the flux vapor since flux was contained in the solder paste and evaporated during the soldering process. The acoustic streaming and cavitation might facilitate the flux vapor to escape from the molten solder and this phenomenon is known as the degassing effect. Another possibility is that this flux vapor might collapse and be fragmented into smaller cavities or bubbles. Therefore, with lesser and smaller macrovoids, the shear strength of the ultrasonic-treated samples was generally higher than the control sample, which is in accordance with our shear strength results obtained above.

As observed in every sample, the shear fracture was initiated at region 1 and propagated to region 2. The fracture of the control sample was mainly ductile failure as only parabolic dimples were observed in both region 1 and 2, as shown in Figure 5.8(a-i) and 5.8(a-ii). Similar ductile failure was also observed in the region 1 of all the ultrasonic-treated samples. However, in the region 2, there is a change from ductile failure to mixed

mode of ductile-brittle failure at the Cu_6Sn_5/solder interface when the USV time increased from 1.5 to 6 s. Parabolic dimples that originated from the tip of Cu_6Sn_5 scallop at the joint interface were observed in the USV-treated samples within 3 s (Figure 5.8(b-ii) and 5.8(c-ii)). Mixed mode of ductile-brittle failure that occurred at the interfacial Cu_6Sn_5 scallops was exhibited in the region 2 of the USV-treated sample with 4.5 s (Figure 5.8(d-ii)), whereas larger area of brittle failure was observed in the region 2 of the sample treated with 6 s of USV (Figure 5.8(e-ii)).

To further identify the influence of USV time on the joint shear strength, the composition of the shear-fractured surface of every sample was identified by XRD and the results are depicted in Figure 5.9. Generally, β-Sn, Cu_6Sn_5, Ag_3Sn and Cu are the four phases that present in every sample. The intensity of β-Sn phase was the highest in every sample, indicating that the shear fracture occurred mainly within the solder matrix. The number of dominant β-Sn peaks was higher in the ultrasonic-treated samples compared to the control sample, showing that USV has promoted the formation of β-Sn phase with different crystallographic orientation in the solder joints. This may reduce the anisotropic behavior of the solder joint and thereby corroborate to the higher shear strength, as observed in the ultrasonic-treated samples (Kariya, Tajima, & Yamada, 2012). High intensity of Cu_6Sn_5 phase was also detected in every sample and its intensity was higher in the ultrasonic-treated samples than the control sample, implying that the failure may occur at the Cu_6Sn_5/solder interfaces or at the eutectic phase region or both.

On the other hand, higher intensity of Cu was observed in the samples treated with 1.5 and 6 s of USV. The increase of Cu content in the former sample may be attributed to the rapid Cu dissolution mechanism as mentioned earlier. Whereas, in the latter sample, the prolonged USV time induced intense superheating in the molten solder and resulted in further dissolution of Cu atoms from the substrate. As for the Ag_3Sn phase, it has the lowest intensity in every sample but its intensity increased slightly with the USV time.

This can be attributed to the coarsening of the eutectic phase after ultrasonic treatment, typically at the USV time of 6 s where plate-like Ag_3Sn phase was formed. The plate-like Ag_3Sn phase is known to have lower dislocation resistant compared to the particle-like Ag_3Sn phase, which has higher resistant by pinning the dislocation at the boundaries of β-Sn phase (Yang & Zhang, 2013b). Therefore, the plate-like Ag_3Sn may act as the crack initiation site upon shear test and deteriorate the shear strength. Furthermore, given the alignment of the plate-like Ag_3Sn as observed in the Figure 5.2(e), it might facilitate the brittle failure along the interfacial Cu_6Sn_5 scallops as shown in Figure 5.8(e-ii).

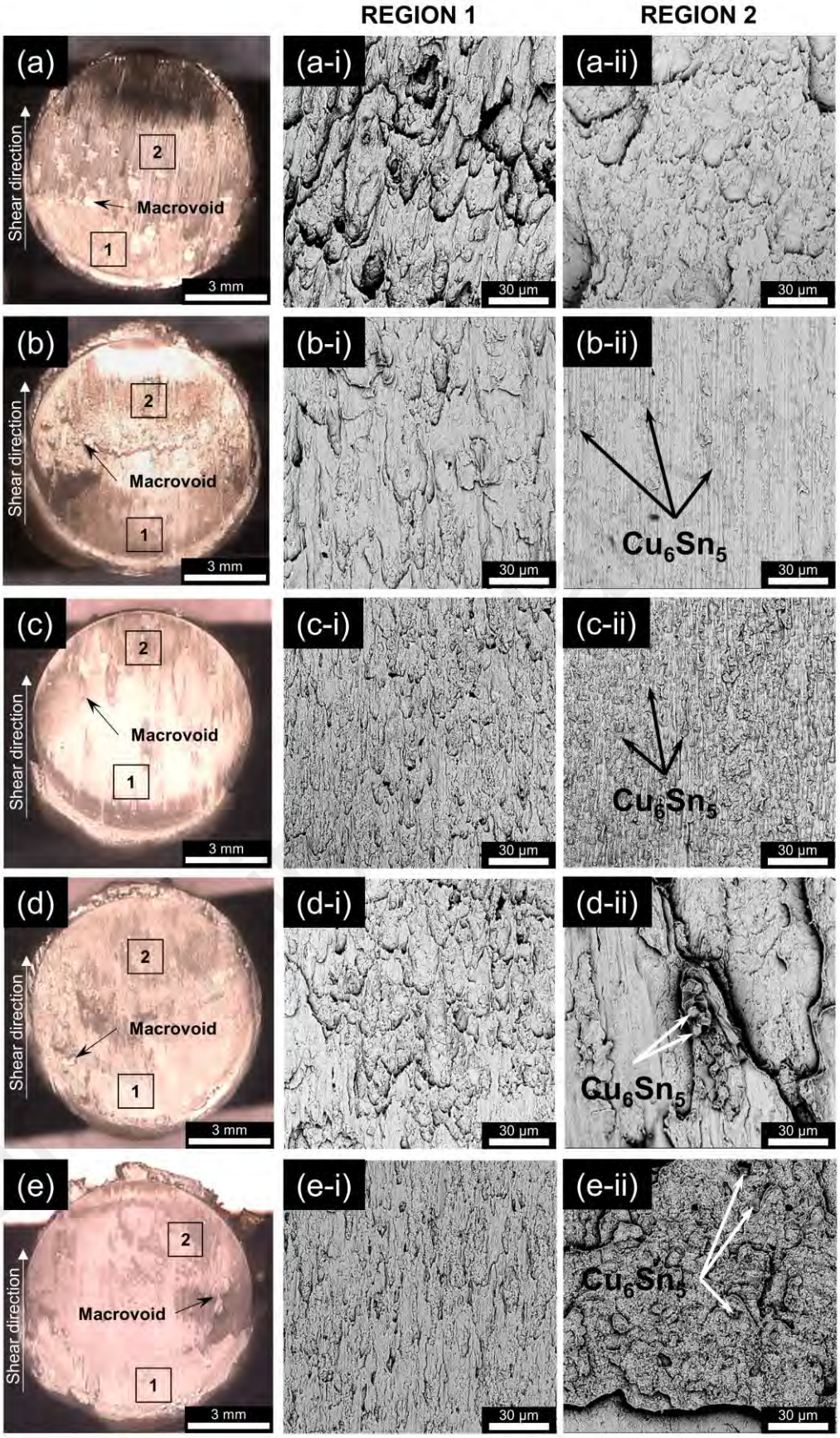

Figure 5.8: Shear-fractured surface of the Cu/SAC305/Cu solder joints soldered (a) without USV and with 10 W USV for USV time of (b) 1.5 s, (c) 3 s, (d) 4.5 s and (e) 6 s

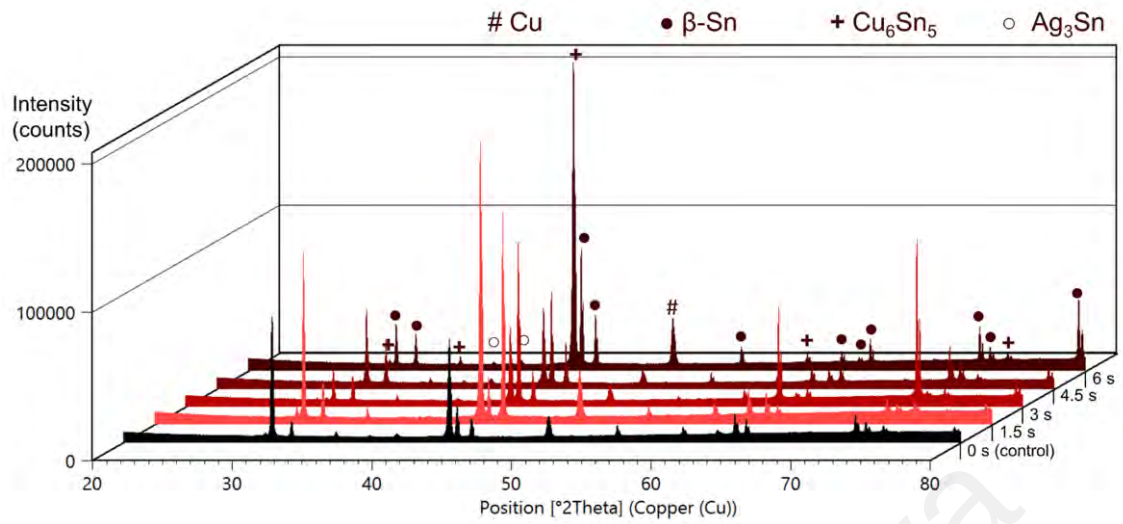

Figure 5.9: XRD analysis of the shear-fractured surface of the solder joints

5.4 Conclusion

Ultrasonic assisted reflow soldering of Cu/SAC305/Cu samples was conducted by applying low-power-high-frequency USV on the sample during the reflow stage for 1.5 to 6 s. The influence of USV time on the microstructure and shear strength of the solder joints can be summarized as follows:

a) The solder matrix microstructure of the Cu/SAC305/Cu joint was refined at 1.5 s of USV time but coarsened after 3 s. The microstructure of the interfacial IMC layers at the top and bottom Cu/SAC305 joint interfaces of all the USV-treated samples was also refined after the ultrasonic treatment. However, the effect of USV time is not significant as all the USV-treated samples showed comparable refinement regardless of the applied USV time.

b) The solder matrix refinement has promoted the solder matrix hardness of the USV-treated sample at 1.5 s, but the coarsening of solder matrix has reduced the solder matrix hardness of the samples treated with 3 s to 6 s of USV.

c) The total thickness of interfacial IMC layers reduced with increasing USV time, except for the USV-treated sample at 1.5 s, where the bottom interfacial IMC layer was exceptionally thicker than the other counterparts. The short USV time may have

allowed the continual and rapid dissolution of Cu from the bottom Cu substrate during the post-ultrasonic reflow period.

d) The ultrasonic-treated samples possessed higher shear strength than the control sample. The samples treated with 6 s of USV possessed the lowest shear strength among the ultrasonic-treated samples.

CHAPTER 6: EFECT OF ULTRASONIC POWER ON THE LEAD FREE SOLDER JOINTS SOLDERED BY LOW-POWER-HIGH-FREQUENCY ULTRASONIC ASSISTED REFLOW SOLDERING

6.1 Introduction and literature review

The research in this chapter has been published in *Journal of Alloys and Compounds, Volume 705, 2017, Pages 188-197*, written by Ai Ting Tan, Ai Wen Tan and Farazila Yusof. The dissertation author is the first author of the publication.

In the last two chapters, we proposed to apply high-power-low-frequency and low-power-high-frequency USV during the reflow stage of reflow soldering for Cu/SAC305/Cu solder joints, where the molten SAC solder has complete fluidity. These studies showed that the ultrasonic-treated solder joints possessed higher shear strength, regardless of which type of USV used. This is contributed by the USV-induced degassing mechanism in the molten solder, which reduced the size of macrovoids that formed in the solder joints. We also observed that the interfacial IMC layers were generally thinner and the morphology of Cu_6Sn_5 IMC was finer after the ultrasonic treatment, mainly due to the acoustic cavitation and acoustic streaming induced by USV.

However, there are distinguished differences in the solder matrix microstructure, solder matrix hardness and shear strength of the solder joint with respect to USV time (within 6 s) when different types of USV were employed. The influence of USV time was less significant at high-power-low-frequency USV. The solder matrix microstructure was refined after the ultrasonic treatment and became small grain-like structure at all tested USV time. The variation of the joint shear strength and the solder matrix hardness with respect to USV time is insignificant as well. On the contrary, at low-power-high-frequency USV, the solder matrix microstructure was refined after treated with shorter USV time (1.5 s) but coarsened after treated with longer USV time (3 to 6 s). The solder

matrix hardness increased when the solder matrix microstructure was refined, but decreased when the microstructure was coarsened. Additionally, the shear strength of the solder joints with coarsened solder matrix microstructure was higher than those with refined microstructure.

According to Luque de Castro and Priego-Capote (Luque de Castro & Priego-Capote, 2007), ultrasonic power of a USV can effectively accelerate the mass transfer and increase the driving force for crystallization in a mixture. In other words, the solder matrix microstructure as observed in Chapter 3 and 4 may also be affected by the ultrasonic power of USV, since the two types of USV used are of different ultrasonic power (169 W and 10 W, respectively). Therefore, based on the consideration of power consumption and process performance, low-power-high-frequency USV is used in the present study and the effect of ultrasonic power on the solder joint properties is investigated in this chapter. We believe that an in-depth understanding on the influence of such parameter is important for the optimization and up-scaling of ultrasonic application in the soldering industry.

6.2 Methodology

6.2.1 Sample preparation

The test sample of the experiment consisted of SAC305 solder paste (ALMIT SRC, LFM-series) and two Cu substrates (99% purity) with the dimensions of 15 mm × 15 mm × 3 mm (bottom substrate) and 2 mm × 8 mm in diameter (top substrate). The faying surface of the substrates was ground, polished and cleaned using standard metallographic techniques prior to soldering. The SAC305 paste was then deposited in between the substrates through a mask with an opening diameter of 6 mm and thickness of 0.4 mm (equivalent to 0.1 g of solder paste). The layout of the test sample is illustrated in Figure 6.1(a).

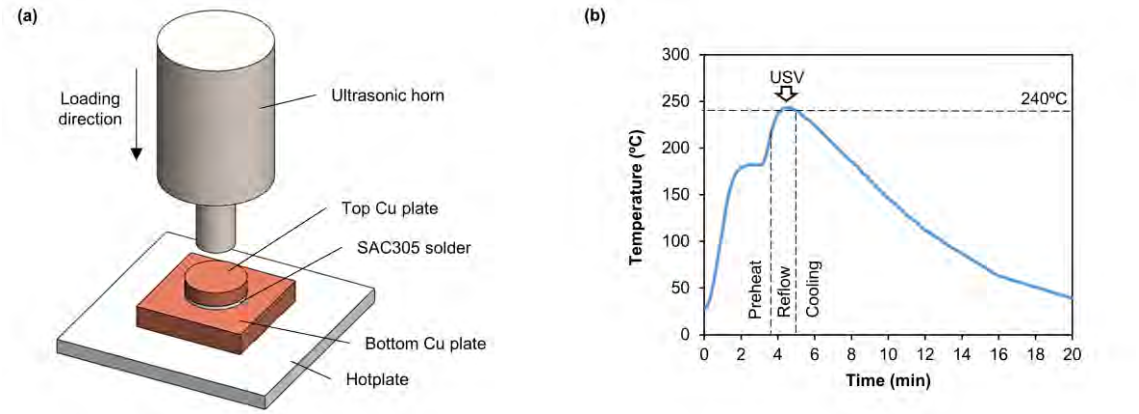

Figure 6.1: (a) Schematic illustration of test sample and (b) reflow soldering profile

6.2.2 Soldering procedure

The test sample was reflowed on a hotplate (CHP-170DN, AS-ONE) under ambient atmosphere, following the reflow soldering profile as shown in Figure 6.1(b). Once the soldering temperature reached above 240 °C, an ultrasonic horn (HC-DLT-5580, Hangzhou Create Ultrasonic Technology Co., Ltd) was loaded on the top Cu substrate to apply 55 ± 1 kHz vertical USV with different ultrasonic power of 10, 20 and 30 W (equivalent to 2, 4, and 6 μm in amplitude) for 1.5 and 4.5 s, respectively. These two USV time were selected due to the optimal results obtained in our previous study. The hotplate was turned off immediately after the reflow stage and the sample was then cooled to room temperature at a rate of 0.3 ℃/s. Non-ultrasonic treated sample was fabricated to serve as the control sample.

6.2.3 Cross-sectional microstructure analysis

The soldered samples were cross-sectioned at the center and then ground and polished using standard metallographic techniques. Next, the samples were etched in the solution of 10 vol. % of HCl + 90 vol. % of CH_3OH for 15 s to reveal their microstructure. Scanning electron microscope (SEM, Phenom ProX) equipped with energy-dispersive X-

ray spectroscopy (EDS) was employed to observe the cross-sectional microstructure and to identify the composition of the phases in the samples.

An image analysis software (Image J, NIH software) was used to measure the width of β-Sn phase and the thickness of interfacial IMC layer in each sample. The average width of the β-Sn phase in each sample was extracted from at least five different SEM micrographs. The interfacial IMC layer thickness was calculated by dividing the total area of the IMC layer to its total length, as measured from a SEM micrograph. The average thickness value was then derived from the measurements at minimum five different spots in each sample.

The hardness of the solder matrix of each sample was measured by a Vicker microhardness tester (HMV 2T E, SHIMADZU) with a pyramidal diamond indenter. The indentation was performed on the cross sections of each sample, using a test load of 98.07 mN and a dwell time of 10 s. The average hardness value was obtained from a minimum of 20 indentations that performed randomly on each sample.

6.2.4 Shear analysis

Compressive shear test was conducted at room temperature, using a universal testing machine (Instron 3369). The bottom Cu substrate was clamped to the shear test fixture while the top Cu substrate was shear punched with a shear strain rate of 0.5 mm/min. The average shear strength was taken from three different samples for each soldering parameter. The microstructure and elemental composition of the shear fractured surface were then observed by the SEM equipped with EDS and analyzed by X-ray diffractometer (XRD, PANalytical Empyrean) fitted with CuKα radiation in the 2θ range of 20-80 °.

6.3 Results and discussion

6.3.1 Solder matrix microstructure of Cu/SAC305/Cu joints

Figure 6.2 shows the cross-sectional microstructure of the non-ultrasonic treated Cu/SAC305/Cu joint (the control sample). The solder matrix of the control sample was constituted by primary β-Sn and eutectic phases, which were exhibited as whitish and grayish areas, respectively, in Figure 6.2(a). As observed from Figure 6.2(a) and 6.2(c), the primary β-Sn phase was in a dendritic structure and adhered with nearly circular branches. These β-Sn dendrites were aligned in the oblique direction to the Cu substrates. Meanwhile, the eutectic phase present at the interspace between the primary β-Sn phases was in a structure of β-Sn matrix embedded with the particle or rod-like Ag-rich and Cu-rich intermetallic phases, as illustrated in Figure 6.2(c) and 6.2(d). The Ag-rich and Cu-rich intermetallic phases were possibly Ag_3Sn and Cu_6Sn_5 phases, based on our previous study (Ai Ting Tan, Tan, & Yusof, 2017).

Morphological change of the β-Sn phase was observed in the solder joints after treated with USV. Figure 6.3 shows the cross-sectional microstructure of the Cu/SAC305/Cu joints treated with 10 to 30 W of USV for 1.5 and 4.5 s. At shorter USV time (1.5 s), the β-Sn dendrites became shorter and finer in size after treated with USV below 30 W (Figure 6.3(a) and 6.3(c)). Some of the β-Sn phases were seemingly more grain-like rather than dendritic. When the ultrasonic power was increased to 30 W for the same USV time, the β-Sn dendrites elongated in the direction oblique to the Cu substrates (Figure 6.3(e)). However, at longer USV time (4.5 s), coarsening of β-Sn dendrites in terms of the dendrite width was observed in the sample treated with 10 W of USV (Figure 6.3(b)), compared to the dendrites formed in those of the control sample and the samples treated with shorter USV time (1.5 s). When the ultrasonic power was increased to 20 W and above, the β-Sn phase changed to grain-like structure, as shown in Figure 6.3(d) and

6.3(f). Moreover, the size of the grain-like β-Sn phase was finer at 20 W of USV, but coarsened at 30 W of USV.

In order to quantify the degree of refinement and coarsening of the β-Sn phase under the influence of USV, the width of the β-Sn phase was measured and the results were plotted in Figure 6.4. The results showed that the width of the β-Sn phase reduced and became more homogeneous when treated with shorter USV time (1.5 s) as compared to the control sample. However, the degree of reduction and homogeneity of the β-Sn width decreased with increasing ultrasonic power from 10 to 30 W. On the contrary, under the influence of longer USV time (4.5 s), the width of the β-Sn phase increased generally with ultrasonic power and became less homogenous compared to the control sample. An exception was observed in the sample treated with 20 W of USV, in which the width of the β-Sn phase was remarkably shorter and more homogenous than those of the control sample.

Apart from the morphological change of β-Sn phase, a notable variation on the distribution of eutectic phase was observed in the ultrasonic-treated samples. The eutectic phase in the ultrasonic-treated samples (Figure 6.3) was generally more evenly distributed at the interspacing of β-Sn phases compared to those in the control sample (Figure 6.2(a)). Furthermore, the total grayish area in the solder matrix region seemingly increased with increasing ultrasonic power, regardless of the USV time. Additionally, Cu_6Sn_5 IMC precipitates, in the form of whisker, were found in the eutectic region of the samples treated with 10 and 30 W of USV for 4.5 s (Figure 6.3(b) and 6.3(f)).

The results obtained above suggest that the ultrasonic power of USV is responsible for the morphological change of β-Sn phase at different USV time and the increasing formation of eutectic phase in the solder matrix of the Cu/SAC305/Cu solder joints. Under the normal reflow soldering process, Cu_6Sn_5 IMC (that may contribute to the eutectic phase) nucleates first in the molten solder during the reflow stage due to the

rapid dissolution of Cu atoms from the Cu substrate at increasing soldering temperature. When the molten solder starts to solidify and then undergoes a large undercooling, β-Sn phase nucleates and preferably grows into dendritic structure, as observed in Figure 6.2(a). When the temperature drops to the eutectic temperature (approximately 217 °C for SAC305 solder), the remaining molten solder solidifies to form the eutectic phase.

The application of USV during the reflow stage has induced acoustic streaming and acoustic cavitation in the molten solder. Acoustic streaming homogenizes the mass and heat transfer within the molten solder, contributing to the uniform distribution of eutectic phase in the solder matrix of the ultrasonic-treated samples, as observed in Figure 6.3. Whereas, acoustic cavitation is associated with the formation of tiny bubbles in the molten solder, either from the pre-existing bubbles (due to the evaporation of soldering flux) or the cavities that formed at the solid/liquid interface with the aid of USV. These cavitation bubbles will expand and compress in size according to the pressure induced by the USV. The surrounding molten solder of these cavitation bubbles will be either undercooled when the bubble expanded or superheated when the bubble is compressed. Undercooling of the molten solder promotes the formation of β-Sn phase, while superheating promotes the formation of eutectic phase. The size of these cavitation bubbles increases as a function of USV time and when they reach their resonance size, they might collapse (termed as transient cavitation) and release a tremendous amount of heat and shock waves in the molten solder (T. Leong et al., 2011). Otherwise, the cavitation bubbles might continue to oscillate without collapsing (termed as stable cavitation). The heat released from the transient cavitation contributes to additional superheating effect, while the shock waves contribute to the additional streaming effect. The oscillating stable cavitation would contribute to micro-streaming effect as well.

According to Santos et al. (Santos, Lodeiro, & Capelo-Martínez, 2009), the intensity of acoustic streaming and acoustic cavitation is proportional to the power of the

USV. Therefore, the oscillation of cavitation bubbles becomes greater as a function of ultrasonic power and the bubbles have higher tendency to collapse and release a greater amount of heat and shock waves in the molten solder. The excessive heat generated promotes the further dissolution of Cu from the Cu substrate and possibly causes the nucleated β-Sn phase to be re-melted. This might be the reason for the increasing formation of eutectic phase in the samples treated with increasing ultrasonic power, as observed in Figure 6.3. Meanwhile, the additional shock waves and the intensified acoustic streaming will effectively accelerate the mass and heat transfer within the molten solder. Since the phase formation occurs through nucleation and subsequent growth via diffusion, this enables the nucleated β-Sn and eutectic phases to grow faster during the reflow stage, leading to the growth of β-Sn and eutectic phases, as shown in Figure 6.4 and 6.3, respectively. With the aid of segregation and aggregation effects induced at longer USV time (4.5 s), the nucleated β-Sn phases aggregate and grow larger in size, while the nucleated Cu_6Sn_5 IMC morph into Cu_6Sn_5 whiskers in the eutectic region, as shown in Figure 6.3(b) and 6.3(f). However, the shape of these phases depends on the growth rate at each face of the phase. Based on the observation in Figure 6.2(a), the β-Sn phase preferred to grow into dendrite that aligned with the direction oblique to the Cu substrates. Since the refined β-Sn phase remained dendrite after treated with shorter USV time (1.5 s) but changed to grain-like structure after treated with longer USV time (4.5 s) at higher ultrasonic power, we speculate that the nucleated β-Sn phase has obtained sufficient energy and speed to approach each face of the larger β-Sn phase when the power of the USV is higher and last for a longer duration. Therefore, the β-Sn phase was refined and became grain-like structure after treated with 20 W of USV for 4.5 s and coarsened in size when the ultrasonic power increased to 30 W.

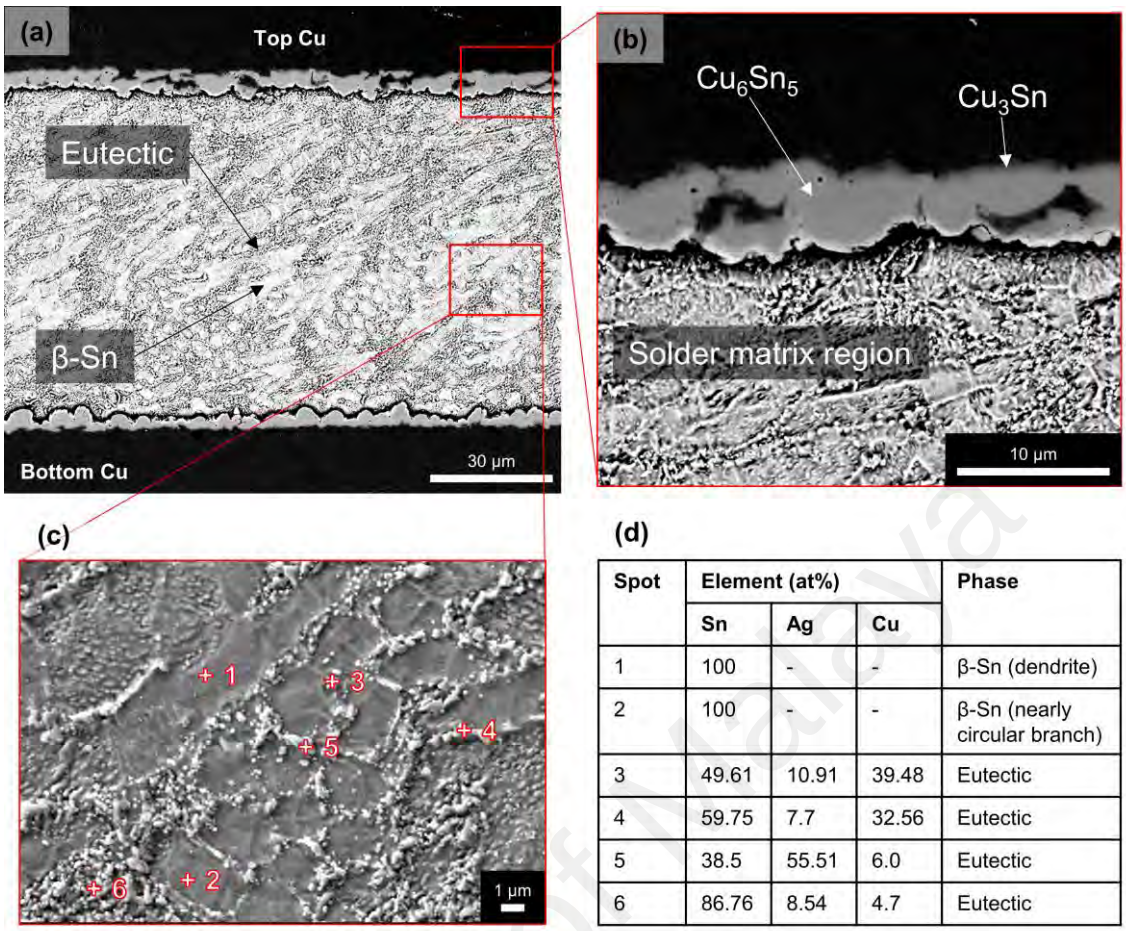

(d)

Spot	Element (at%)			Phase
	Sn	Ag	Cu	
1	100	-	-	β-Sn (dendrite)
2	100	-	-	β-Sn (nearly circular branch)
3	49.61	10.91	39.48	Eutectic
4	59.75	7.7	32.56	Eutectic
5	38.5	55.51	6.0	Eutectic
6	86.76	8.54	4.7	Eutectic

Figure 6.2: Cross-sectional SEM micrographs of non-ultrasonic treated Cu/SAC305/Cu joint; (a) Overall microstructure, (b) microstructure at the Cu/SAC305 interface, (c) microstructure at the solder matrix region and (d) EDS analysis corresponds to (c)

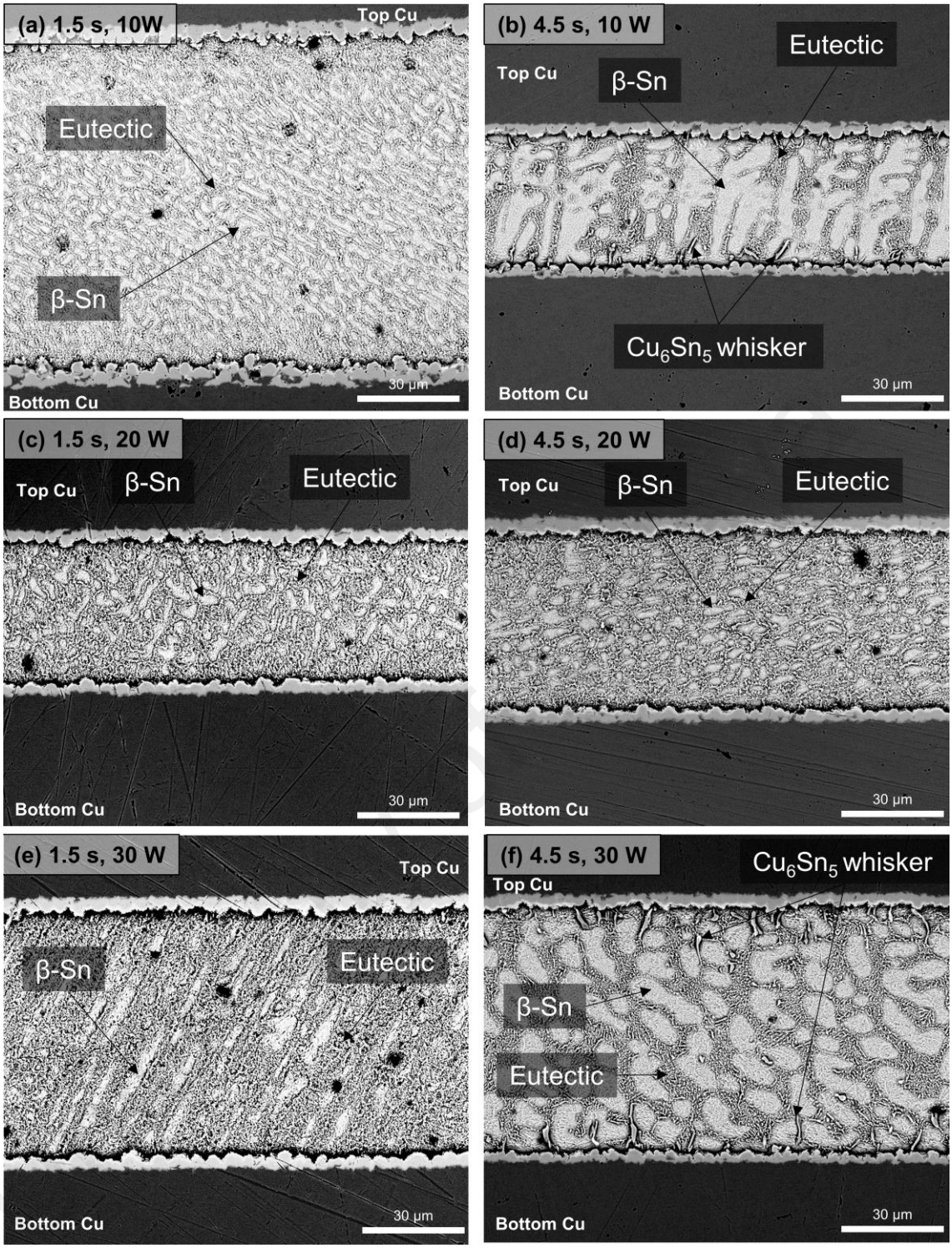

Figure 6.3: Cross-sectional SEM micrographs of Cu/SAC305/Cu joints treated with USV for 1.5 s at (a) 10 W, (c) 20 W, (e) 30 W and 4.5 s at (b) 10 W, (d) 20 W, and (f) 30 W

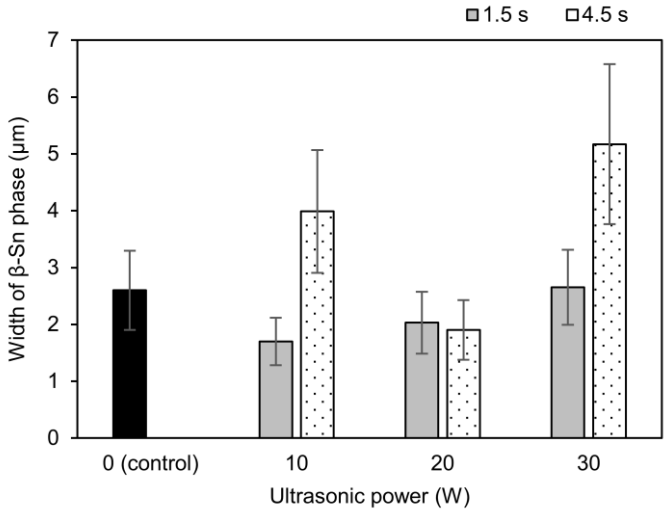

Figure 6.4: Width of the β-Sn phase with respect to ultrasonic power

6.3.2 Solder matrix hardness of Cu/SAC305/Cu joints

Figure 6.5 shows the Vickers hardness of the solder matrix of Cu/SAC305/Cu joints treated with and without USV. The average solder matrix hardness of the control sample was 11.465 HV, with a standard deviation of 0.57 HV. The samples treated with shorter USV time (1.5 s) possessed higher hardness value than the control sample, whereas lower hardness value was obtained by the samples treated with longer USV time (4.5 s). However, at shorter USV time (1.5 s), the solder matrix hardness of the samples decreased gradually with increasing ultrasonic power. On the contrary, at longer USV time (4.5 s), the solder matrix hardness of the samples generally increased with increasing ultrasonic power, with the highest solder matrix hardness of 11.297 ± 0.42 HV was obtained by the sample treated with 20 W of USV.

The results obtained are in good agreement with the studies of Lee and Huang (H.-T. Lee & Huang, 2016) and Chinnam et al. (Chinnam et al., 2011), in which smaller β-Sn phase and finer eutectic structure resulted in greater solder matrix hardness. The refinement on the β-Sn dendrites after treated with shorter USV time (1.5 s) contributes to the general improvement of the solder matrix hardness compared to the control sample, as shown in Figure 6.5. As the width of the β-Sn dendrites increased gradually with the

ultrasonic power (Figure 6.4), the solder matrix hardness decreased accordingly as the consequence. On the other hand, in the samples treated with longer USV time (4.5 s), the coarsening of β-Sn phase and the formation of Cu_6Sn_5 whiskers in the eutectic region may have reduced the resistance of solder matrix against the indentation force, and resulted in lower solder matrix hardness compared to the control sample. The higher solder matrix hardness obtained by the samples treated with higher ultrasonic power for 4.5 s may be attributed to the morphological change of β-Sn phase from the dendritic (Figure 6.3(b)) to grain-like structure (Figure 6.3(d) and 6.3(f)). The enhanced uniformity of the structure of β-Sn phase and the dispersion of eutectic phase might have improved the resistance against dislocation. The smaller grain-like β-Sn phase in the sample treated with 20 W of USV (Figure 6.3(d) and 6.4) might have further improved the solder matrix hardness.

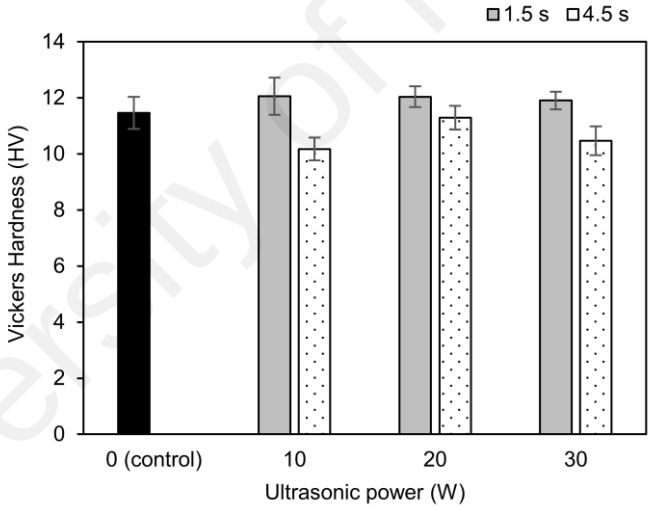

Figure 6.5: Vickers hardness of Cu/SAC305/Cu solder matrix with respect to ultrasonic power

6.3.3 Interfacial microstructure at Cu/SAC305 interfaces

As seen from Figure 6.2 and 6.3, continuous Cu_6Sn_5 and Cu_3Sn IMC layers were the two interfacial IMC layers that formed at the Cu/SAC305 interfaces of every sample. These IMCs were formed due to the reaction between the Sn atoms (from the molten SAC305 solder) and Cu atoms (from the solid substrate) at the Cu/SAC305 interfaces. The

mechanism of the interfacial reaction can be explained by the concept of "local nominal composition" which can be found in the previously published literatures (Laurila et al., 2010; Rönkä et al., 1997). The formation of interfacial IMC layer indicates that the proposed ultrasonic assisted reflow soldering allows good wettability of SAC305 solder on the Cu substrates, which promotes the diffusion of Sn and Cu atoms at the solid/liquid interfaces to form strong Cu-Sn metallurgical bonds (Giuranno, Delsante, Borzone, & Novakovic, 2016; Suganuma, 2001). The Cu_6Sn_5 IMC layer (near to the solder matrix) was thick and had a scallop-like morphology, whereas the Cu_3Sn IMC layer (near to the Cu substrate) was very thin and had a planar-like morphology, as shown in Figure 6.2(b). Similar morphology was reported in the works of Marques et al. (Marques et al., 2014) and Gain et al. (Gain et al., 2015). No significant morphological change was observed at the Cu_3Sn IMC layer of each sample. As for the morphology of Cu_6Sn_5 IMC layer, the size of Cu_6Sn_5 IMC scallops (in terms of width and height) was not uniform across the top and bottom Cu/SAC305 interfaces in the control sample (Figure 6.2(a)). The Cu_6Sn_5 IMC scallops became seemingly smaller and more homogenous in size after treating with USV (Figure 6.3). However, there was no noticeable morphological variation among the ultrasonic-treated samples, except for the sample treated with 10 W of USV for 1.5 s, in which the Cu_6Sn_5 IMC scallops seemed to decrease in width but increase in height.

In order to identify the influence of ultrasonic power on the formation of interfacial IMCs, the thickness of interfacial (Cu_6Sn_5 + Cu_3Sn) IMC layer at the top and bottom Cu/SAC305 interfaces was measured and the results were plotted in Figure 6.6. In the control sample, there was a discrepancy between the top and bottom interfacial IMC layer thickness, in which the top interfacial IMC layer (4.40 ± 0.29 μm) was thicker than the bottom layer (3.30 ± 0.38 μm). Generally, after being treated with USV, the discrepancy between the top and bottom interfacial IMC layer thickness decreased, with the top interfacial IMC layer found to be always thicker than the bottom layer. However,

different trend was noticed in the sample treated with 10 W of USV for 1.5 s, in which the bottom interfacial IMC layer (5.34 ± 0.64 μm) was thicker than the top interfacial IMC layer (4.54 ± 0.33 μm).

The change of Cu_6Sn_5 IMC scallop size and the reduction of discrepancy between the top and bottom interfacial IMC layer thickness after the ultrasonic treatment indicate that the formation and growth of interfacial IMCs across both the Cu/SAC305 interfaces become more uniform after treating with USV. This may be contributed by the homogenization effect induced by acoustic streaming on the temperature distribution and the dissolution of Cu atoms across the interfaces during the reflow stage. The exceptions that were noticed in the sample treated with 10 W of USV for 1.5 s are probably attributed to the instability of the small nucleated β-Sn phase near to the Cu/SAC305 interfaces, typically at the bottom interface where thermal heat was continuously supplied by the hot plate during the post-ultrasonic reflow period. As observed in Figure 6.4, the width of β-Sn phase in the sample treated with 10 W of USV for 1.5 s was the smallest compared to the other counterparts. Therefore, the nucleated β-Sn phase in that sample is presumably smaller in size and probably re-melted to form interfacial Cu_6Sn_5 IMC when subjected to the continuous thermal heat during the post-ultrasonic reflow period. The assumption is in line with the results obtained from Figure 6.4 and Figure 6.6, in which the interfacial IMC layer was thicker when the width of β-Sn phase was smaller. However, the interfacial IMC layer thickness in the sample treated with 30 W of USV for 1.5 s was thicker than expected and this observation is probably due to the excessive heat generated by the intensified acoustic cavitation when using 30 W of USV.

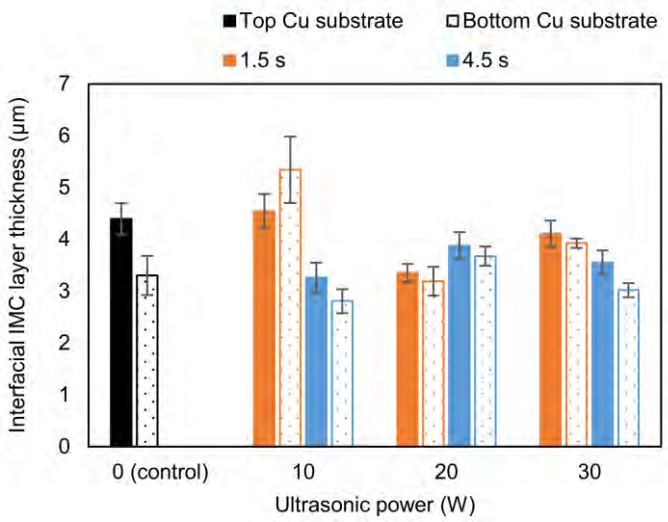

Figure 6.6: Interfacial IMC layer thickness at Cu/SAC305 interfaces with respect to ultrasonic power

6.3.4 Shear strength of Cu/SAC305/Cu joints

Figure 6.7(a) shows the results of shear strength of the Cu/SAC305/Cu joints treated with and without USV. The shear strength of the control sample was 37.70 ± 3.88 MPa. Generally, the shear strength of the solder joints was enhanced by the ultrasonic treatment, with a minimum improvement of 24.14 % obtained compared to the control sample. In comparison, the shear strength of the samples treated with shorter USV time (1.5 s) was lower than the samples treated with longer USV time (4.5 s), regardless of the ultrasonic power. Nonetheless, when the samples were ultrasonic-treated with increasing ultrasonic power, the shear strength of the samples treated with shorter USV time (1.5 s) fluctuated, whereas the shear strength of the samples treated with longer USV time (4.5 s) increased gradually. Based on the shear stress-strain curves as shown in Figure 6.7(b), all the samples exhibited ductile failure mode. It is observed that the shear strain of the samples increased with USV time.

Fracture analysis after the shear test was carried out to further investigate the influence of ultrasonic power on the Cu/SAC305/Cu joint shear strength. The morphology and composition of the shear-fractured surface on the top Cu substrate of

every sample was analyzed using SEM, EDS and XRD. Macrovoids were found in every sample but the size of the macrovoids in the ultrasonic-treated samples (represented by Figure 6.8(d) and 6.8(g)) was remarkably smaller than the control sample (Figure 6.8(a)). Based on the SEM observations, the shear fracture was initiated at region 1 and propagated to region 2. At region 1, ductile failure with parabolic dimples was observed in the solder matrix of every sample (refer to Figure 6.8(b), 6.8(e) and 6.8(h)), where the composition on the surface was mainly composed of Sn element. Ductile failure was also observed at the region 2 of every sample, but the location changed from within the solder matrix in the control sample (Figure 6.8(c)) to the solder matrix near to the interfacial Cu_6Sn_5 IMC layer in the ultrasonic-treated samples (represented by Figure 6.8(f) and 6.8(i)).

Figure 6.9 shows the XRD analysis of the shear-fractured surface on the top Cu substrate of every sample. Compared to the control sample, the intensity of β-Sn, Cu and Cu_6Sn_5 peaks was generally higher in the ultrasonic-treated samples, as shown in Figure 6.9(a). When the samples were treated at increasing ultrasonic power, the variation in the intensity of β-Sn, Cu and Cu_6Sn_5 peaks in the samples was very similar to the trend depicted in Figure 6.7. The intensity of these peaks fluctuated in the samples treated with shorter USV time (1.5 s) but increased gradually in the samples treated with longer USV time (4.5 s). By comparing the ratio of β-Sn to Cu_6Sn_5 peaks (Figure 6.9(b)), the shear-fractured surface of the samples treated with shorter USV time (1.5 s) had a higher ratio of Cu_6Sn_5 phase, whereas the samples treated with longer USV time (4.5 s) possessed a higher ratio of β-Sn phase.

Based on the results presented above, it can be deduced that the overall improvement of shear strength in the ultrasonic-treated samples is contributed by the size reduction of the macrovoids. Macrovoids are formed in the solder joints due to the entrapment of soldering flux that evaporated during the reflow soldering process. With

the aid of acoustic streaming and cavitation, these entrapped flux vapors can either escape from the molten solder or collapse and then fragment into smaller cavities before the molten solder solidifies. In other words, the porosity of the ultrasonic-treated samples is lower than the control sample, resulting in higher shear strength. However, the variation of shear strength among the ultrasonic-treated samples may be associated with the morphological change of β-Sn phase at different ultrasonic parameters. As the samples treated with shorter USV time (1.5 s) were lower in shear strength compared to the samples treated with higher USV time (4.5 s), we speculate that the refinement of β-Sn dendrites might cause the dislocation to occur at the boundary between the β-Sn phase and the eutectic phase or interfacial Cu_6Sn_5 IMC layer. Additionally, the shear strength will deteriorate further since the refined β-Sn dendrites were not aligned in the direction perpendicular to the shear direction. On the contrary, with the coarsening of β-Sn phase and morph into grain-like structure as observed in the samples treated with longer USV time (4.5 s), the dislocation might take place within the β-Sn phase, thus improving the shear strength through strain hardening mechanism. The assumption is in good agreement with the obtained shear stress-strain curves and XRD results shown in Figure 6.7(b) and 6.9, respectively.

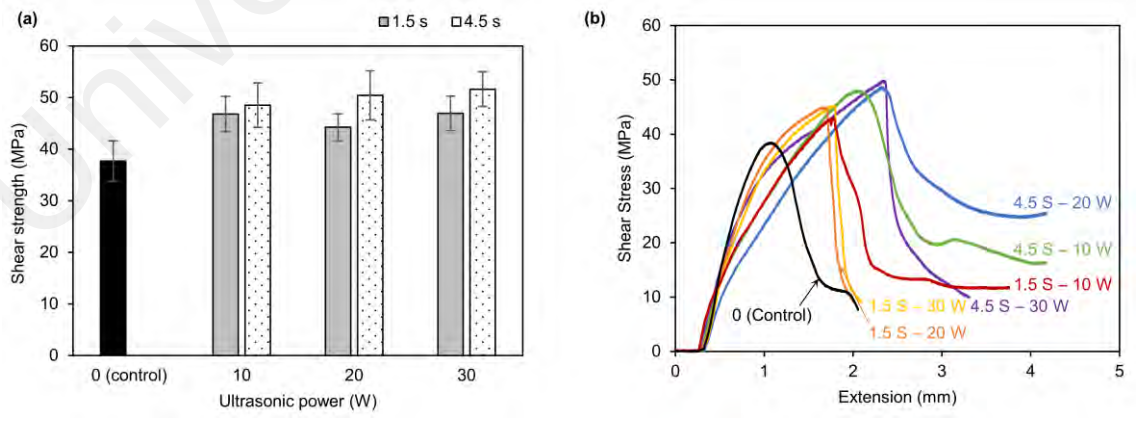

Figure 6.7: Shear test results of Cu/SAC305/Cu joints with respect to ultrasonic power; (a) Average shear strength and (b) shear stress-strain behavior

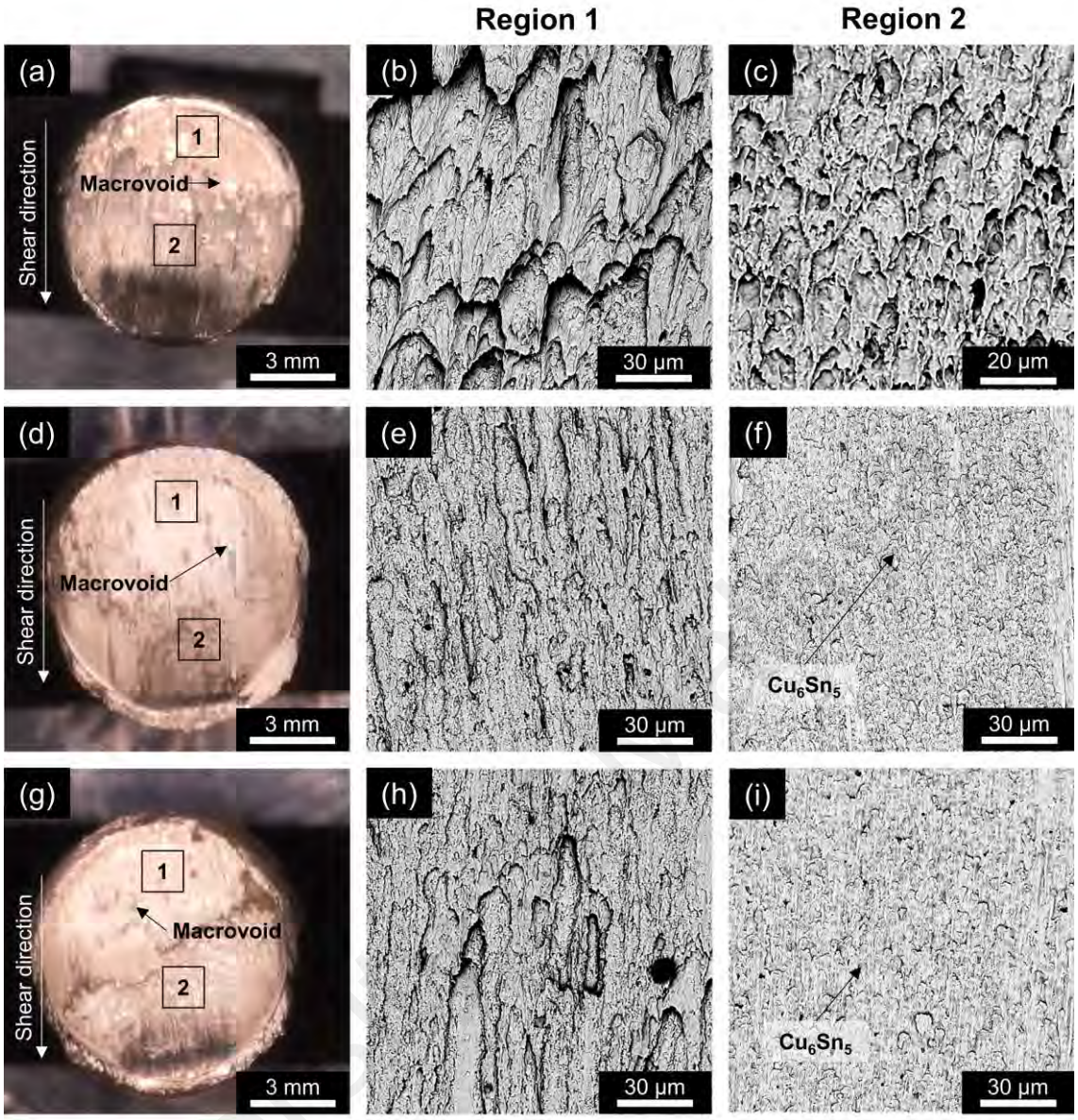

Figure 6.8: Shear-fractured surface of Cu/SAC305/Cu joints; (a-c) without USV, (d-f) 1.5 s, 30 W and (g-i) 4.5 s, 30 W

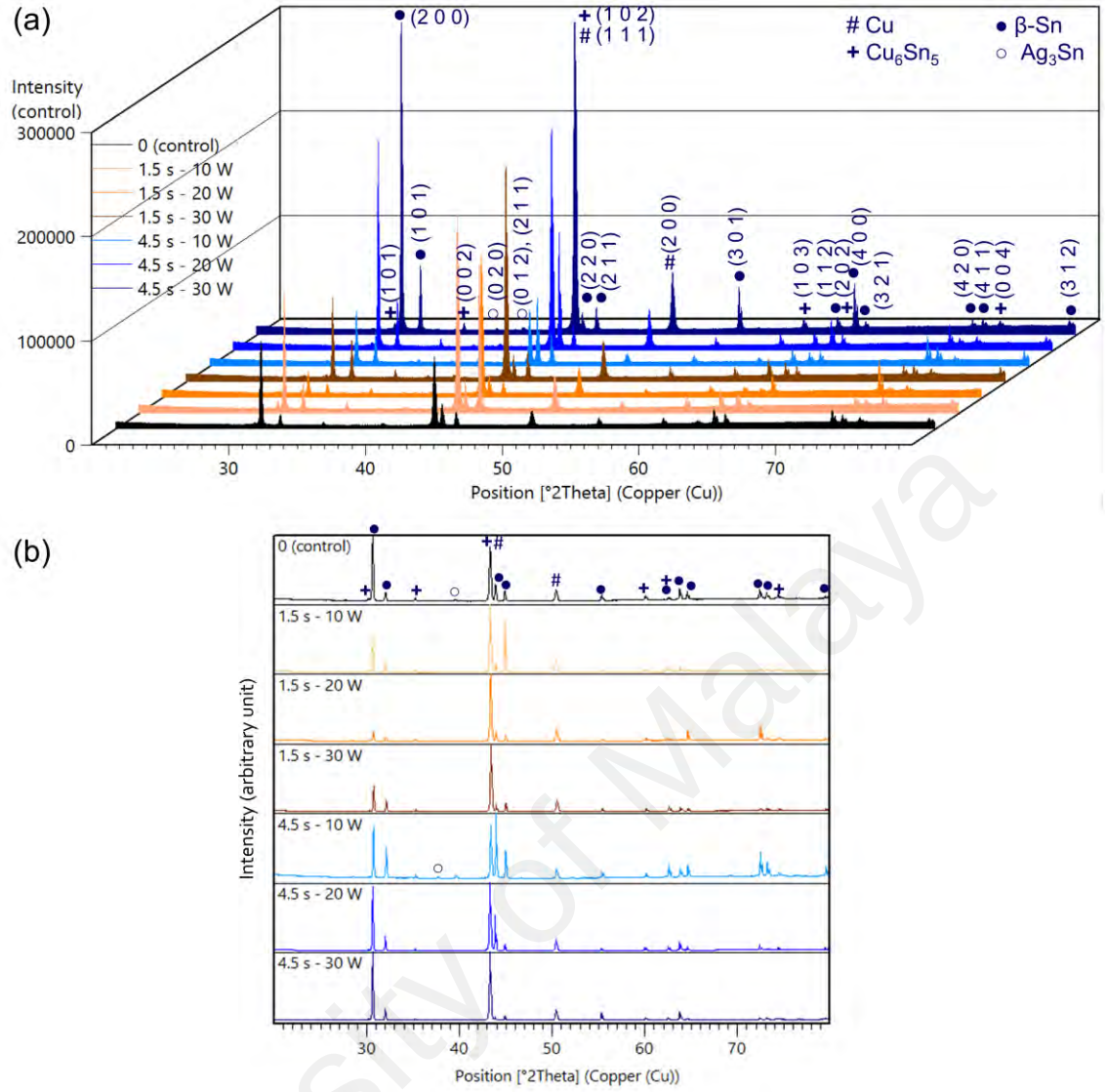

Figure 6.9: XRD analysis of the shear-fractured surface of Cu/SAC305/Cu joints based on (a) actual intensity and (b) intensity in arbitrary unit

6.4 Conclusion

The influence of ultrasonic power ranging from 10 to 30 W on the microstructure and mechanical properties of Cu/SAC305/Cu solder joints can be summarized as follows:

a) For the samples treated with shorter USV time (1.5 s), the β-Sn dendrites in the solder matrix were finer compared to the control sample but the width of the β-Sn dendrites increased with increasing ultrasonic power. For the samples treated with longer USV time (4.5 s), the β-Sn phase changed from dendritic to grain-like structure when the

ultrasonic power was increased from 10 to 20 W and above. The width of the β-Sn phase in these samples was generally larger than the control sample.

b) The formation of eutectic phase in the solder matrix of the ultrasonic-treated samples increased with increasing ultrasonic power, regardless of the USV time.

c) Compared to the solder matrix hardness of the control sample, the Vickers hardness value was higher in the samples treated with shorter USV time (1.5 s) but lower in the samples treated with longer USV time (4.5 s), irrespective of the ultrasonic power. At increasing ultrasonic power, the hardness value of the samples treated with 1.5 s decreased, whereas the value of the samples treated with 4.5 s fluctuated at different ultrasonic power.

d) Compared to the interfacial IMC layer in the control sample, the interfacial Cu_6Sn_5 scallops were finer in morphology and the discrepancy between the top and bottom interfacial IMC layers was smaller in the ultrasonic-treated samples, except in the sample treated with 10 W of USV for 1.5 s. This may be associated with the instability of the nucleated β-Sn phase when subjected to continuous heating during the post-ultrasonic reflow period.

e) For the samples treated with USV at increasing ultrasonic power, the interfacial IMC layer thickness varied according to the morphology of β-Sn phase of the corresponding samples, in which smaller β-Sn phase resulted in thicker interfacial IMC layer. However, the interfacial IMC layer in the sample treated with 30 W of USV for 1.5 s was thicker than expected and this may be due to excessive heat generated in the molten solder when using 30 W of USV.

f) All the ultrasonic-treated samples were at least 24.14% higher in shear strength than the control sample. The shear strength of the samples treated with longer USV time (4.5 s) was higher compared to those treated with shorter USV time (1.5 s). Overall,

the shear strength of the ultrasonic-treated samples increased with increasing ultrasonic power.

CHAPTER 7: CONCLUSION AND RECOMMENDATIONS

7.1 Conclusion

The foremost aim of the thesis was to improve the SAC lead free solder joint reliability by using the proposed ultrasonic assisted reflow soldering technique. The foresaid objective was successfully achieved by applying USV on the soldering assembly during the reflow stage of reflow soldering process. The conclusions for the adopted objectives of the present thesis are as follows:

1) Cu/SAC305/Cu solder joint was successfully fabricated by the proposed reflow soldering technique by using two types of USV, namely low-power-high-frequency and high-power-low-frequency USV.
2) After treating with both type of USV, the solder matrix microstructure of the lead free solder joint was altered and the interfacial IMC layers were thinner. Size reduction of the macrovoids was observed in the ultrasonic-treated solder joints and resulted in enhanced shear strength.
3) The results obtained from the studies in the chapter 4 and 5 suggest that low-power-high-frequency USV is more suitable for the application of reflow soldering.
4) When using high-power-low-frequency USV, morphological change of β-Sn phase with respect to USV time was observed in the solder matrix region. However, the yield strength of the solder joint decreased with increasing USV time due to the increase of solder matrix hardness.
5) When using low-power-high-frequency USV, the solder matrix microstructure of the ultrasonic-treated joint was refined at 1.5 s of USV time but coarsened at 3 s and above. The solder matrix hardness was increased with refined solder matrix microstructure but reduced with coarsened microstructure. However, the solder joint with coarsened solder matrix microstructure obtained relatively higher shear strength.

6) Increase of USV power would promote the formation of eutectic phase, regardless of the USV time. Additionally, the shear strength of the solder joint with coarsened solder matrix microstructure was found to increase with increasing USV power.

The reported findings of this dissertation demonstrate that ultrasonic assisted reflow soldering is a viable approach in producing lead free solder joint with better reliability. In addition, the application of USV during the reflow stage is more effective compared to its application during the cooling stage as the properties of the solder joint could be tailored with lower USV power and shorter USV time.

7.2 Recommendation for future work

The following recommendations are to be considered for future research works.

1) The long term reliability of the solder joint could be evaluated by subjected into thermal aging, thermal cycling and electromigration test conditions that simulating the actual working conditions of a soldering assembly.
2) Modelling and simulation works could be carried out to identify the minimum vibrational energy required to refine or coarsen the solder matrix microstructure of a SAC solder joint.
3) Fundamental study could be conducted to reveal the relationship between the USV parameters (frequency, time and power) with the mass and heat transfer as well as the diffusion activity in the vicinity of the molten SAC solder.
4) Soldering assembly with different geometry, configurations and materials could be tested in order to explore their relationship with the USV parameters.

REFERENCES

Abtew, M., & Selvaduray, G. (2000). Lead free Solders in Microelectronics. *Materials Science and Engineering: R: Reports, 27*(5–6), 95-141.

Baldan, A. (2002). Review Progress in Ostwald ripening theories and their applications to nickel-base superalloys - Part I: Ostwald ripening theories. *Journal of Materials Science, 37*(11), 2171-2202.

Bieler, T. R., Zhou, B. T., Blair, L., Zamiri, A., Darbandi, P., Pourboghrat, F., . . . Liu, K. C. (2012). The Role of Elastic and Plastic Anisotropy of Sn in Recrystallization and Damage Evolution During Thermal Cycling in SAC305 Solder Joints. *Journal of Electronic Materials, 41*(2), 283-301.

Bušek, D., Dušek, K., Růžička, D., Plaček, M., Mach, P., Urbánek, J., & Starý, J. (2016). Flux effect on void quantity and size in soldered joints. *Microelectronics Reliability, 60*, 135-140.

Chan, Y. C., & Yang, D. (2010). Failure mechanisms of solder interconnects under current stressing in advanced electronic packages. *Progress in Materials Science, 55*(5), 428-475.

Chellvarajoo, S., & Abdullah, M. Z. (2016). Microstructure and mechanical properties of Pb-free Sn–3.0Ag–0.5Cu solder pastes added with NiO nanoparticles after reflow soldering process. *Materials & Design, 90*, 499-507.

Chen, G., Wu, F., Liu, C., Silberschmidt, V. V., & Chan, Y. C. (2016). Microstructures and properties of new Sn–Ag–Cu lead free solder reinforced with Ni-coated graphene nanosheets. *Journal of Alloys and Compounds, 656*, 500-509.

Chinnam, R. K., Fauteux, C., Neuenschwander, J., & Janczak-Rusch, J. (2011). Evolution of the microstructure of Sn–Ag–Cu solder joints exposed to ultrasonic waves during solidification. *Acta Materialia, 59*(4), 1474-1481.

Chung, T. Y., Jhang, J. H., Chen, J. S., Lo, Y. C., Ho, G. H., Wu, M. L., & Sun, C. C. (2012). A study of large area die bonding materials and their corresponding mechanical and thermal properties. *Microelectronics Reliability, 52*(5), 872-877.

Deng, S. S., Hwang, S. J., & Lee, H. H. (2016). Temperature prediction for system in package assembly during the reflow soldering process. *International Journal of Heat and Mass Transfer, 98*, 1-9.

Deng, X., Chawla, N., Chawla, K. K., & Koopman, M. (2004). Deformation behavior of (Cu, Ag)–Sn intermetallics by nanoindentation. *Acta Materialia, 52*(14), 4291-4303.

Dušek, K., & Váňa, T. (2011, 11-15 May 2011). *Study of temperature profiles of the infrared continuous furnace.* Paper presented at the Proceedings of the 2011 34th International Spring Seminar on Electronics Technology (ISSE).

El-Daly, A. A., Fawzy, A., Mansour, S. F., & Younis, M. J. (2013a). Novel SiC nanoparticles-containing Sn–1.0Ag–0.5Cu solder with good drop impact performance. *Materials Science and Engineering: A, 578*, 62-71.

El-Daly, A. A., Fawzy, A., Mansour, S. F., & Younis, M. J. (2013b). Thermal analysis and mechanical properties of Sn–1.0Ag–0.5Cu solder alloy after modification with SiC nano-sized particles. *Journal of Materials Science: Materials in Electronics, 24*(8), 2976-2988.

Ely, D. R., Edwin García, R., & Thommes, M. (2014). Ostwald–Freundlich diffusion-limited dissolution kinetics of nanoparticles. *Powder Technology, 257*(0), 120-123.

Fathian, Z., Maleki, A., & Niroumand, B. (2017). Synthesis and characterization of ceramic nanoparticles reinforced lead free solder. *Ceramics International, 43*(6), 5302-5310.

Fawzy, A., Fayek, S. A., Sobhy, M., Nassr, E., Mousa, M. M., & Saad, G. (2014). Tensile creep characteristics of Sn–3.5Ag–0.5Cu (SAC355) solder reinforced with nano-metric ZnO particles. *Materials Science and Engineering: A, 603*(0), 1-10.

Frear, D. R. (2006). Issues related to the implementation of Pb-free electronic solders in consumer electronics. *Journal of Materials Science: Materials in Electronics, 18*(1-3), 319-330.

Gagliano, R., & Fine, M. (2001). Growth of η phase scallops and whiskers in liquid tin-solid copper reaction couples. *JOM, 53*(6), 33-38.

Gain, A. K., Zhang, L., & Chan, Y. C. (2015). Microstructure, elastic modulus and shear strength of alumina (Al2O3) nanoparticles-doped tin–silver–copper (Sn–Ag–Cu) solders on copper (Cu) and gold/nickel (Au/Ni)-plated Cu substrates. *Journal of Materials Science: Materials in Electronics, 26*(9), 7039-7048.

Géczy, A., Kvanduk, B., Illes, B., & Harsányi, G. (2016). Comparative study on proper thermocouple attachment for vapour phase soldering profiling. *Soldering & Surface Mount Technology, 28*(1), 7-12.

Géczy, A., Szőke, P., Illyefalvi-Vitéz, Z., Ruszinkó, M., & Bunea, R. (2011, 20-23 Oct. 2011). *Soldering profile optimization for vapour phase reflow technology.* Paper presented at the 2011 IEEE 17th International Symposium for Design and Technology in Electronic Packaging (SIITME).

Giuranno, D., Delsante, S., Borzone, G., & Novakovic, R. (2016). Effects of Sb addition on the properties of Sn-Ag-Cu/(Cu, Ni) solder systems. *Journal of Alloys and Compounds, 689*, 918-930.

Gong, J., Liu, C., Conway, P. P., & Silberschmidt, V. V. (2008). Evolution of CuSn intermetallics between molten SnAgCu solder and Cu substrate. *Acta Materialia, 56*(16), 4291-4297.

Gong, J., Liu, C., Conway, P. P., & Silberschmidt, V. V. (2009). Initial formation of CuSn intermetallic compounds between molten SnAgCu solder and Cu substrate. *Scripta Materialia, 60*(5), 333-335.

Han, Y. D., Jing, H. Y., Nai, S. M. L., Xu, L. Y., Tan, C. M., & Wei, J. (2012a). Interfacial reaction and shear strength of Ni-coated carbon nanotubes reinforced Sn-Ag-Cu solder joints during thermal cycling. *Intermetallics, 31*, 72-78.

Handwerker, C., Kattner, U., & Moon, K. W. (2007). Fundamental Properties of Pb-Free Solder Alloys. In J. Bath (Ed.), *Lead free Soldering* (pp. 21-74). Boston, MA: Springer US.

Haseeb, A. S. M. A., & Leng, T. S. (2011). Effects of Co nanoparticle addition to Sn–3.8Ag–0.7Cu solder on interfacial structure after reflow and ageing. *Intermetallics, 19*(5), 707-712.

Hodúlová, E., Palcut, M., Lechovič, E., Šimeková, B., & Ulrich, K. (2011). Kinetics of intermetallic phase formation at the interface of Sn–Ag–Cu–X (X=Bi, In) solders with Cu substrate. *Journal of Alloys and Compounds, 509*(25), 7052-7059.

Hokka, J., Mattila, T. T., Xu, H., & Paulasto-Kröckel, M. (2013). Thermal Cycling Reliability of Sn-Ag-Cu Solder Interconnections—Part 2: Failure Mechanisms. *Journal of Electronic Materials, 42*(6), 963-972.

Huang, M. L., Zhao, J. F., Zhang, Z. J., & Zhao, N. (2015). Role of diffusion anisotropy in β-Sn in microstructural evolution of Sn-3.0Ag-0.5Cu flip chip bumps undergoing electromigration. *Acta Materialia, 100*, 98-106.

Huang, N., Hu, A., & Li, M. (2013). Influence of texture of Cu on the growth of Cu–Sn intermetallic compounds. *Materials Letters, 109*(0), 8-11.

Huang, Y. L., Xiu, Z. Y., Wu, G. H., Tian, Y. H., & He, P. (2016). Sn-3.0Ag-0.5Cu nanocomposite solders reinforced by graphene nanosheets. *Journal of Materials Science-Materials in Electronics, 27*(7), 6809-6815.

Illés, B., & Géczy, A. (2012). Multi-physics modelling of a vapour phase soldering (VPS) system. *Applied Thermal Engineering, 48*, 54-62.

Illés, B., & Géczy, A. (2016). Investigating the heat transfer on the top side of inclined printed circuit boards during vapour phase soldering. *Applied Thermal Engineering, 103*, 1398-1407.

Illés, B., Géczy, A., Skwarek, A., & Busek, D. (2016). Effects of substrate thermal properties on the heat transfer coefficient of vapour phase soldering. *International Journal of Heat and Mass Transfer, 101*, 69-75.

Imai, D., Kibushi, R., Hatakeyama, T., Nakagawa, S., & Ishizuka, M. (2014, 23-25 April 2014). *The effect of thermal conductivity of board to laser condition in laser soldering the case of paste solder.* Paper presented at the 2014 International Conference on Electronics Packaging (ICEP).

Ji, H., Wang, Q., Li, M., & Wang, C. (2014). Ultrafine-Grain and Isotropic Cu/SAC305/Cu Solder Interconnects Fabricated by High-Intensity Ultrasound-Assisted Solidification. *Journal of Electronic Materials, 43*(7), 2467-2478.

Ji, H. J., Wang, Q., & Li, M. Y. (2016). Microstructural Evolution of Lead free Solder Joints in Ultrasonic assisted Soldering. *Journal of Electronic Materials, 45*(1), 88-97.

Ji, H. J., Wang, Q., Li, M. Y., & Wang, C. Q. (2014). Effects of ultrasonic irradiation and cooling rate on the solidification microstructure of Sn-3.0Ag-0.5Cu alloy. *Journal of Materials Processing Technology, 214*(1), 13-20.

Jing, H. Y., Guo, H. J., Wang, L. X., Wei, J., Xu, L. Y., & Han, Y. D. (2017). Influence of Ag-modified graphene nanosheets addition into Sn–Ag–Cu solders on the formation and growth of intermetallic compound layers. *Journal of Alloys and Compounds, 702*, 669-678.

Jung, Y., Ryu, D., Gim, M., Kim, C., Song, Y., Kim, J., . . . Lee, C. (2016, May 31 2016-June 3 2016). *Development of Next Generation Flip Chip Interconnection Technology Using Homogenized Laser-Assisted Bonding.* Paper presented at the 2016 IEEE 66th Electronic Components and Technology Conference (ECTC).

Kago, K., Suetsugu, K., Hibino, S., Ikari, T., Furusawa, A., Takano, H., . . . Matsushige, K. (2004). Novel ultrasonic soldering technique for lead free solders. *Materials Transactions, 45*(3), 703-709.

Kariya, Y., Tajima, S., & Yamada, S. (2012). Influence of Crystallographic Orientation on Fatigue Reliability of beta-Sn and beta-Sn Micro-Joint. *Materials Transactions, 53*(12), 2067-2071.

Kim, Y., Roh, H. R., Kim, S., & Kim, Y. H. (2010). Kinetics of Intermetallic Compound Formation at the Interface Between Sn-3.0Ag-0.5Cu Solder and Cu-Zn Alloy Substrates. *Journal of Electronic Materials, 39*(12), 2504-2512.

Kotadia, H. R., Mokhtari, O., Clode, M. P., Green, M. A., & Mannan, S. H. (2012). Intermetallic compound growth suppression at high temperature in SAC solders with Zn addition on Cu and Ni–P substrates. *Journal of Alloys and Compounds, 511*(1), 176-188.

Lau, C. S., & Abdullah, M. Z. (2013). Simulation investigations on fluid/structure interaction in the reflow soldering process of board-level BGA Packaging. *International Journal of Computer Theory and Engineering, 5*(4), 645.

Laurila, T., Karppinen, J., Vuorinen, V., Li, J., Paul, A., & Paulasto-Kröckel, M. (2012). Effect of Isothermal Aging and Electromigration on the Microstructural Evolution of Solder Interconnections During Thermomechanical Loading. *Journal of Electronic Materials, 41*(11), 3179-3195.

Laurila, T., Vuorinen, V., & Kivilahti, J. K. (2005). Interfacial reactions between lead free solders and common base materials. *Materials Science and Engineering: R: Reports, 49*(1–2), 1-60.

Laurila, T., Vuorinen, V., & Paulasto-Kröckel, M. (2010). Impurity and alloying effects on interfacial reaction layers in Pb-free soldering. *Materials Science and Engineering: R: Reports, 68*(1-2), 1-38.

Lee, H. T., & Huang, K. C. (2016). Effects of Cooling Rate on the Microstructure and Morphology of Sn-3.0Ag-0.5Cu Solder. *Journal of Electronic Materials, 45*(1), 182-190.

Lee, J. S., Chu, K. M., Patzelt, R., Manessis, D., Ostmann, A., & Jeon, D. Y. (2008). Effects of Co addition in eutectic Sn–3.5Ag solder on shear strength and microstructural development. *Microelectronic Engineering, 85*(7), 1577-1583.

Lee, N. C. (2001). *Reflow Soldering Processes*. Burlington, MA: Newnes.

Lee, N. C. (1999). Optimizing the reflow profile via defect mechanism analysis. *Soldering & Surface Mount Technology, 11*(1), 13-20.

Lee, N. C. (2000, 24-28 Sept. 2008). *Lead free soldering and low alpha solders for wafer level interconnects*. Paper presented at the 2000 SMTA International.

Leicht, H., & Thumm, A. (2008). *Today's Vapor Phase Soldering-An Optimized Reflow Technology for Lead Free Soldering.* Paper presented at the SMTAI Conference Proceedings.

Leong, T., Ashokkumar, M., & Sandra, K. (2011). The fundamentals of power ultrasound - A review. *Acoustics Australia, 39*(2), 54-63.

Li, J. F., Agyakwa, P. A., & Johnson, C. M. (2012). Effect of trace Al on growth rates of intermetallic compound layers between Sn-based solders and Cu substrate. *Journal of Alloys and Compounds, 545*, 70-79.

Liang, J., Dariavach, N., & Shangguan, D. (2007). Metallurgy, Processing and Reliability of Lead free Solder Joint Interconnections. In E. Suhir, Y. C. Lee, & C. P. Wong (Eds.), *Micro- and Opto-Electronic Materials and Structures: Physics, Mechanics, Design, Reliability, Packaging* (pp. A351-A409). Boston, MA: Springer US.

Liashenko, O. Y., Lay, S., & Hodaj, F. (2016). On the initial stages of phase formation at the solid Cu/liquid Sn-based solder interface. *Acta Materialia, 117*, 216-227.

Lihua, Q., Jihua, H., Jing, N., Long, Y., Yaorong, F., Xingke, Z., & Hua, Z. (2009, 10-13 Aug. 2009). *Microstructure changes and compound growth dynamic at lead free/Cu interface under different conditions.* Paper presented at the Electronic Packaging Technology & High Density Packaging, 2009. ICEPT-HDP '09. International Conference on.

Lin, Y. W., Lai, Y. S., Lin, Y. L., Tu, C. T., & Kao, C. R. (2008). Tin whisker growth induced by high electron current density. *Journal of Electronic Materials, 37*(1), 17-22.

Liu, B., Tian, Y., Liu, W., Wu, W., & Wang, C. (2016). TEM observation of interfacial compounds of SnAgCu/ENIG solder bump after laser soldering and subsequent hot air reflows. *Materials Letters, 163*, 254-257.

Liu, C. Y., Lai, C. H., Wang, M. C., & Hon, M. H. (2006). Thermal behavior and microstructure of the intermetallic compounds formed at the Sn–3Ag–0.5Cu/Cu interface after soldering and isothermal aging. *Journal of Crystal Growth, 290*(1), 103-110.

Liu, P., Yao, P., & Liu, J. (2009). Evolutions of the interface and shear strength between SnAgCu–xNi solder and Cu substrate during isothermal aging at 150°C. *Journal of Alloys and Compounds, 486*(1-2), 474-479.

Liu, W., Tian, Y., Wang, C., Wang, X., & Liu, R. (2012). Morphologies and grain orientations of Cu–Sn intermetallic compounds in Sn3.0Ag0.5Cu/Cu solder joints. *Materials Letters, 86*(0), 157-160.

Livovsky, L., Pietrikova, A., & Durisin, J. (2008, 7-11 May 2008). *Monitoring of the temperature profile of vapour phase reflow soldering.* Paper presented at the 2008 31st International Spring Seminar on Electronics Technology.

Luque de Castro, M. D., & Priego-Capote, F. (2007). Ultrasound-assisted crystallization (sonocrystallization). *Ultrasonics Sonochemistry, 14*(6), 717-724.

M.A.A, M. S., Bakri, A. M. M. A., Kamarudin, H., Bnhussain, M., M.H, Z. H., & Somidin, F. (2011). Solderability of Sn-0.7Cu/Si3N4 lead free composite solder on Cu-substrate. *Physics Procedia, 22*, 299-304.

Ma, Y., Li, X., Zhou, W., Yang, L., & Wu, P. (2017). Reinforcement of graphene nanosheets on the microstructure and properties of Sn58Bi lead free solder. *Materials & Design, 113*, 264-272.

Ma, Z. L., Belyakov, S. A., & Gourlay, C. M. (2016). Effects of cobalt on the nucleation and grain refinement of Sn-3Ag-0.5Cu solders. *Journal of Alloys and Compounds, 682*, 326-337.

Mahmudi, R., & Alibabaie, S. (2013). Elevated-temperature shear strength and hardness of Zn–3Cu–xAl ultra-high-temperature lead free solders. *Materials Science and Engineering: A, 559*, 421-426.

Marques, V. M. F., Johnston, C., & Grant, P. S. (2014). Microstructural evolution at Cu/Sn–Ag–Cu/Cu and Cu/Sn–Ag–Cu/Ni–Au ball grid array interfaces during thermal ageing. *Journal of Alloys and Compounds, 613*, 387-394.

Mei, Z. (2005). Microstructural Evolution and Interfacial Interactions in Lead free Solder Interconnects. In D. Shangguan (Ed.), *Lead free Solder Interconnect Reliability* (pp. 29 - 65). Materials Park, OH: ASM International.

Mohankumar, K., & Tay, A. A. O. (2004, 8-10 Dec. 2004). *Nano-particle reinforced solders for fine pitch applications.* Paper presented at the Proceedings of 6th Electronics Packaging Technology Conference (EPTC 2004) (IEEE Cat. No.04EX971).

Mohd Salleh, M. A. A., McDonald, S. D., Gourlay, C. M., Yasuda, H., & Nogita, K. (2016). Suppression of Cu6Sn5 in TiO2 reinforced solder joints after multiple reflow cycles. *Materials & Design, 108*, 418-428.

Mookam, N., & Kanlayasiri, K. (2012). Evolution of Intermetallic Compounds between Sn-0.3Ag-0.7Cu Low-silver Lead free Solder and Cu Substrate during Thermal Aging. *Journal of Materials Science & Technology, 28*(1), 53-59.

Moore, A. L., & Shi, L. (2014). Emerging challenges and materials for thermal management of electronics. *Materials Today, 17*(4), 163-174.

Nagaoka, T., Morisada, Y., Fukusumi, M., & Takemoto, T. (2009). Joint strength of aluminum ultrasonic soldered under liquidus temperature of Sn–Zn hypereutectic solder. *Journal of Materials Processing Technology, 209*(11), 5054-5059.

Nishikawa, H., & Iwata, N. (2015). Formation and growth of intermetallic compound layers at the interface during laser soldering using Sn–Ag Cu solder on a Cu Pad. *Journal of Materials Processing Technology, 215*, 6-11.

Ogochukwu, E. S. (2013). Laser Soldering. In Y. Mastai (Ed.), Materials Science - Advanced Topics (pp. Ch. 15). Rijeka: InTech.

Park, M. S., & Arróyave, R. (2012). Concurrent nucleation, formation and growth of two intermetallic compounds (Cu6Sn5 and Cu3Sn) during the early stages of lead free soldering. *Acta Materialia, 60*(3), 923-934.

Peng, W., Monlevade, E., & Marques, M. E. (2007). Effect of thermal aging on the interfacial structure of SnAgCu solder joints on Cu. *Microelectronics Reliability, 47*(12), 2161-2168.

Perez, M. (2005). Gibbs–Thomson effects in phase transformations. *Scripta Materialia, 52*(8), 709-712.

Puttlitz, K. J., & Stalter, K. A. (2004). *Handbook of Lead free Solder Technology for Microelectronic Assemblies*: Taylor & Francis.

Qu, L., Zhao, N., Zhao, H. J., Huang, M. L., & Ma, H. T. (2014). In situ study of the real-time growth behavior of Cu6Sn5 at the Sn/Cu interface during the soldering reaction. *Scripta Materialia, 72–73*(0), 43-46.

Reinl, S. (2013). Diode Lasers used in Plastic Welding and Selective Laser Soldering – Applications and Products. *Physics Procedia, 41*, 234-240.

Rizvi, M. J., Chan, Y. C., Bailey, C., Lu, H., & Islam, M. N. (2006). Effect of adding 1 wt% Bi into the Sn–2.8Ag–0.5Cu solder alloy on the intermetallic formations with Cu-substrate during soldering and isothermal aging. *Journal of Alloys and Compounds, 407*(1–2), 208-214.

Rönkä, K. J., van Loo, F. J. J., & Kivilahti, J. K. (1997). The local nominal composition-useful concept for microjoining and interconnection applications. *Scripta Materialia, 37*(10), 1575-1581.

Samanta, K. K. (2016). PA Thermal Management and Packaging: Wideband PA and Packaging, History, and Recent Advances: Part 2. *IEEE Microwave Magazine, 17*(11), 73-81.

Santos, H. M., Lodeiro, C., & Capelo-Martínez, J. L. (2009). The Power of Ultrasound. In J. L. Capelo-Martínez (Ed.), *Ultrasound in Chemistry: Analytical Applications* (pp. 1-16). Weinheim, Germany: Wiley-VCH Verlag GmbH & Co. KGaA.

Schussler, F., Kozic, D., & Franke, J. (2009). Influences on the reflow soldering process by components with specific thermal properties. *Circuit World, 35*(3), 35-42.

Shen, J., & Chan, Y. C. (2009). Research advances in nano-composite solders. *Microelectronics Reliability, 49*(3), 223-234.

Shen, J., Tang, Q., Pu, Y., Zhai, D., Cao, Z., & Chen, J. (2013). Influence of POSS nano-particles on Sn–3.0Ag–0.5Cu–xPOSS/Cu composite solder joints during isothermal aging. *Journal of Materials Science: Materials in Electronics, 24*(12), 4881-4887.

Shen, J., Zhao, M., He, P., & Pu, Y. (2013). Growth behaviors of intermetallic compounds at Sn–3Ag–0.5Cu/Cu interface during isothermal and non-isothermal aging. *Journal of Alloys and Compounds, 574*(0), 451-458.

Shen, Y. A., & Chen, C. (2017). Effect of Sn grain orientation on formation of Cu6Sn5 intermetallic compounds during electromigration. *Scripta Materialia, 128*, 6-9.

Srivalli, C., Abdullah, M. Z., & Khor, C. Y. (2015). Numerical investigations on the effects of different cooling periods in reflow-soldering process. *Heat and Mass Transfer, 51*(10), 1413-1423.

Suganuma, K. (2001). Advances in lead free electronics soldering. *Current Opinion in Solid State and Materials Science, 5*(1), 55-64.

Suh, J. O., Tu, K. N., Lutsenko, G. V., & Gusak, A. M. (2008). Size distribution and morphology of Cu6Sn5 scallops in wetting reaction between molten solder and copper. *Acta Materialia, 56*(5), 1075-1083.

Synkiewicz, B., Skwarek, A., & Witek, K. (2015). Vapour phase soldering used for quality improvement of semiconductor thermogenerators (TEGs) assembly. *Materials Science in Semiconductor Processing, 38*, 346-351.

Tan, A. T., Tan, A. W., & Yusof, F. (2015). Influence of nanoparticle addition on the formation and growth of intermetallic compounds (IMCs) in Cu/Sn-Ag-Cu/Cu solder joint during different thermal conditions. *Science and Technology of Advanced Materials, 16*(3), 18.

Tan, A. T., Tan, A. W., & Yusof, F. (2017). Effect of ultrasonic vibration time on the Cu/Sn-Ag-Cu/Cu joint soldered by low-power-high-frequency ultrasonic assisted reflow soldering. *Ultrasonics Sonochemistry, 34*, 616-625.

Tang, W. M., He, A. Q., Liu, Q., & Ivey, D. G. (2010). Solid state interfacial reactions in electrodeposited Cu/Sn couples. *Transactions of Nonferrous Metals Society of China, 20*(1), 90-96.

Tang, Y., Li, G. Y., & Pan, Y. C. (2013). Influence of TiO2 nanoparticles on IMC growth in Sn–3.0Ag–0.5Cu–xTiO2 solder joints in reflow process. *Journal of Alloys and Compounds, 554*, 195-203.

Tay, S. L., Haseeb, A. S. M. A., Johan, M. R., Munroe, P. R., & Quadir, M. Z. (2013). Influence of Ni nanoparticle on the morphology and growth of interfacial intermetallic compounds between Sn–3.8Ag–0.7Cu lead free solder and copper substrate. *Intermetallics, 33*, 8-15.

Teo, J. W. R., & Sun, Y. F. (2008). Spalling behavior of interfacial intermetallic compounds in Pb-free solder joints subjected to temperature cycling loading. *Acta Materialia, 56*(2), 242-249.

Tian, Y., Zhang, R., Hang, C., Niu, L., & Wang, C. (2014). Relationship between morphologies and orientations of Cu6Sn5 grains in Sn3.0Ag0.5Cu solder joints on different Cu pads. *Materials Characterization, 88*, 58-68.

Tsao, L. C., Huang, C. H., Chung, C. H., & Chen, R. S. (2012). Influence of TiO2 nanoparticles addition on the microstructural and mechanical properties of Sn0.7Cu nano-composite solder. *Materials Science and Engineering: A, 545*(0), 194-200.

Tsao, L. C., Wu, R. W., Cheng, T.-H., Fan, K.-H., & Chen, R. S. (2013). Effects of nano-Al2O3 particles on microstructure and mechanical properties of Sn3.5Ag0.5Cu composite solder ball grid array joints on Sn/Cu pads. *Materials & Design, 50*, 774-781.

Tu, K. N. (2007). Kinetic Analysis of Flux-Driven Ripening of Copper–Tin Scallops. In K. N. Tu (Ed.), *Solder Joint Technology* (Vol. 117, pp. 127-151). New York, NY: Springer New York.

Tu, K. N. (1994). Irreversible-processes of spontaneous whisker growth in bimetallic Cu-Sn thin-film reactions. *Physical Review B, 49*(3), 2030-2034.

Tu, K. N., & Zeng, K. (2001). Tin–lead (SnPb) solder reaction in flip chip technology. *Materials Science and Engineering: R: Reports, 34*(1), 1-58.

Tz-Cheng, C., Kejun, Z., Stierman, R., Edwards, D., & Ano, K. (2004, 1-4 June 2004). *Effect of thermal aging on board level drop reliability for Pb-free BGA packages.* Paper presented at the Electronic Components and Technology Conference, 2004. Proceedings. 54th.

Wang, M. N., Wang, J. Q., Feng, H., & Ke, W. (2012). In-situ observation of fracture behavior of Sn-3.0Ag-0.5Cu lead free solder during three-point bending tests in ESEM. *Materials Science and Engineering a-Structural Materials Properties Microstructure and Processing, 558*, 649-655.

Wang, Y. W., Lin, Y. W., Tu, C. T., & Kao, C. R. (2009). Effects of minor Fe, Co, and Ni additions on the reaction between SnAgCu solder and Cu. *Journal of Alloys and Compounds, 478*(1-2), 121-127.

Wen, Y., Zhao, X., Chen, Z., Gu, Y., Wang, Y., Chen, Z., & Wang, X. (2017). Reliability enhancement of Sn-1.0Ag-0.5Cu nano-composite solders by adding multiple sizes of TiO2 nanoparticles. *Journal of Alloys and Compounds, 696*, 799-807.

Wilde, G., & Perepezko, J. H. (2000). Experimental study of particle incorporation during dendritic solidification. *Materials Science and Engineering: A, 283*(1–2), 25-37.

Wu, A. T., Gusak, A. M., Tu, K. N., & Kao, C. R. (2005). Electromigration-induced grain rotation in anisotropic conducting beta tin. *Applied Physics Letters, 86*(24), 3.

Wua, A. T., & Hsieh, Y. C. (2008). Direct observation and kinetic analysis of grain rotation in anisotropic tin under electromigration. *Applied Physics Letters, 92*(12), 3.

Xu, D. E., Hook, M. D., & Mayer, M. (2017). Real time joint resistance monitoring during solder reflow. *Journal of Alloys and Compounds, 695*, 3002-3010.

Yakymovych, A., Mudry, S., Shtablavyi, I., & Ipser, H. (2016). Effect of nano Co reinforcements on the structure of the Sn-3.0Ag-0.5Cu solder in liquid and after reflow solid states. *Materials Chemistry and Physics, 181*, 470-475.

Yang, L. M., & Zhang, Z. F. (2013a). Effects of Y2O3 Nanoparticles on Growth Behaviors of Cu6Sn5 Grains in Soldering Reaction. *Journal of Electronic Materials, 42*(12), 3552-3558.

Yang, L. M., & Zhang, Z. F. (2013b, 11-14 Aug. 2013). *Influences of intermetallic compounds morphologies on fracture behaviors of Sn-3Ag-0.5Cu/Cu solder joint.* Paper presented at the Electronic Packaging Technology (ICEPT), 2013 14th International Conference on.

Yoon, J. W., Noh, B. I., Kim, B. K., Shur, C. C., & Jung, S. B. (2009). Wettability and interfacial reactions of Sn–Ag–Cu/Cu and Sn–Ag–Ni/Cu solder joints. *Journal of Alloys and Compounds, 486*(1–2), 142-147.

Zeng, G., Xue, S., Zhang, L., Gao, L., Dai, W., & Luo, J. (2010). A review on the interfacial intermetallic compounds between Sn–Ag–Cu based solders and substrates. *Journal of Materials Science: Materials in Electronics, 21*(5), 421-440.

Zhang, L., Xue, S. B., Zeng, G., Gao, L. L., & Ye, H. (2012). Interface reaction between SnAgCu/SnAgCuCe solders and Cu substrate subjected to thermal cycling and isothermal aging. *Journal of Alloys and Compounds, 510*(1), 38-45.

Zhang, Y. (2010). Tin and Tin Alloys for Lead free Solder. In M. Schlesinger & M. Paunovic (Eds.), *Modern Electroplating* (pp. 139-204). New Jersey: John Wiley & Sons, Inc.

Zhang, Z., Li, M., & Wang, C. (2013). Fabrication of Cu6Sn5 single-crystal layer for under-bump metallization in flip-chip packaging. *Intermetallics, 42*(0), 52-55.

Zhao, X., Wen, Y., Li, Y., Liu, Y., & Wang, Y. (2016). Effect of γ-Fe2O3 nanoparticles size on the properties of Sn-1.0Ag–0.5Cu nano-composite solders and joints. *Journal of Alloys and Compounds, 662*, 272-282.

LIST OF PUBLICATIONS

Academic Journals

Tan, A. T., Tan, A. W., & Yusof, F. (2015). Influence of nanoparticle addition on the formation and growth of intermetallic compounds (IMCs) in Cu/Sn-Ag-Cu/Cu solder joint during different thermal conditions. *Science and Technology of Advanced Materials, 16*(3), 18.

Tan, A. T., Tan, A. W., & Yusof, F. (2016). Influence of high-power-low-frequency ultrasonic vibration time on the microstructure and mechanical properties of lead free solder joints. *Journal of Materials Processing Technology, 238*, 8-14.

Tan, A. T., Tan, A. W., & Yusof, F. (2017a). Effect of ultrasonic vibration time on the Cu/Sn-Ag-Cu/Cu joint soldered by low-power-high-frequency ultrasonic assisted reflow soldering. *Ultrasonics Sonochemistry, 34*, 616-625.

Tan, A. T., Tan, A. W., & Yusof, F. (2017b). Evolution of microstructure and mechanical properties of Cu/SAC305/Cu solder joints under the influence of low ultrasonic power. *Journal of Alloys and Compounds, 705*, 188-197.

Conferences and Presentations

Tan, A. T., Farazila, Y., & Hamdi, M. (2015, 19-22 Apr. 2015). *Interfacial reaction of the ultrasonic assisted soldering copper and Sn-3.0Ag-0.5Cu solder alloys.* Paper presented at the 2015 International Brazing & Soldering Conference (IBSC 2015).